NTNU
Norwegian University of
Science and Technology

Introduction of Cobalt Into Silica Aerogels, Metal Speciation and Reducibility

Sondre Håbrekke

Chemistry
Submission date: December 2017
Supervisor: Karina Mathisen, IKJ

Norwegian University of Science and Technology
Department of Chemistry

Acknowledgements

The work of this thesis was carried out at the Department of Chemistry at the Norwegian University of Science and Technology (NTNU). First, I would like to thank the staff at the Swiss-Norwegian Beamlines (SNBL) at the European Synchrotron Radiation Facility for their assistance during my visits, and NTNU and Sparebanken Midt-Norges gavefond til Norges Teknisk-Naturvitenskaplige Universitet for the economic support and coverage of travel expenses. Thanks to Elin Harboe for assistance with BET, Kristin Høydalsvik-Wells and Magnus Rotan for assistance with XRD and Syverin Lierhagen with ICP-MS.

My biggest thanks goes to my supervisor Dr. Karina Mathisen for her continious support during the work of this thesis. Her guidance and support has been invaluable and I would not have made it this far without it. A huge thanks also my co-supervisor ph.d. candidate Karsten Granlund Kirste for always having an open door and answering all kinds questions I may have had.

Thanks to all the other members in the structural chemistry group, old and new, but especially post.doc Tina Kristiansen Voss, ph.d. candidate Stian Forselv and ph.d. candidate Guro Sørli. You have all been there to help when help was needed and made these two years a very enjoyable experience. Weekly group meetings, trips to Røros and fun and games at Kieglekroa would not have been the same without any of the group members.

My friends also deserve thanks for their support, and a special mention to Joakim, my number one study buddy. Last, but not least, a huge thanks to my parents for all the love and support you have given me. I would not be where I am today if it were not for you.

Abstract

Hydrophobic and amorphous silica aerogels with incorporated cobalt(II) in single-site was tried synthesized through the newly developed method of using sodium silicate as the silica precursor and achieving hydrophobicity by applying the ambient pressure drying method (APD). Two different variations of the sol-gel route was applied; the co-precursor method (CP) and the surface derivatization method (SD), where the cobalt precursor was added directly to the sol. Different parameter studies were performed to investigate if single-site cobalt were possible through this method. The parameters investigated included; cobalt content, amount of surface modification agents, pH of the gel at point of gelation and cobalt precursor. A modified version of the surface derivatization method was also tried, where gels were washed with ethanol and heptane to remove unreacted precursors and side products.

Incorporation of cobalt into single-site was not possible to determine with certainty, and cobalt present in the gels were determined to be a mix of different cobalt species such as oxides and cobalt silicate. However, catalytically active silica aerogel-supported cobalt was successfully synthesized, but the catalytically active cobalt specie(s) was not possible to be determined.

X-ray diffraction (XRD) was used to exclude the presence of crystalline phases, indicating unsuccessful incorporation of cobalt into single-site. ICP-MS was used to measure the uptake of cobalt in the silica aerogels, and nitrogen adsorption (BET/BJH) was used to measure the surface area and pore size. Furthermore, thermal stability was determined by heat treatment at 450 °C and 700 °C, and thermal events was monitored by thermal gravimetric analysis (TGA). Scanning electron microscopy was used to observe the topography, chemical environment was determined by x-ray absorption spectroscopy (XAS).

Sammendrag

Hydrofobisk og amorf silika aerogel med inkorporert kobolt(II) i "single-site", ble prøvd syntetisert via den nyutviklede metoden som anvender natriumsilikat som forløper, og tørket ved omgivelsestrykk etter å ha blitt overflatebehandlet og gjort hydrofob. To versjoner av sol-gel metoden ble brukt; "co-precursor" metoden og "surface derivatization" metoden, hvor koboltforløperen ble tilsatt direkte i sol. Ulike parametere ble studert for å se om "single-site" kobolt via denne metoden er mulig. Parameterne som ble studert var: koboltinnhold, konsentrasjon av overflatemodifiserende midler, pH i sol ved gelering og type koboltforløper. En modifisert versjon av "surface derivatization" metoden ble også prøvd hvor gelene ble vasket med etanol og heptan for å fjerne ureagerte forløpere og produkter fra sidereaksjoner.

Om inkorporering av kobolt i "single-site" var suksessfullt, var ikke mulig å fastslå med sikkerhet, og kobolt i gelene ble antatt å være på foreskjellige former, slik som oksider og koboltsilikat. Katalytisk aktiv aerogel med kobolt ble syntetisert, men de katalytisk aktive spesiene var ikke mulig å bestemme.

Røntgendiffraksjon ble brukt for å utelukke kystallinske faser som ellers ville ha indikert mislykket inkorporering av kobolt i "single-site". ICP-MS ble brukt for å bestemme koboltopptak i gelene og nitrogenadsorpsjon (BET/BJH) ble brukt for å bestemme overflate og porestørrelse. Termisk stabilitet ble testet ved varmebehandling på 450 °C og 700 °C, og termiske hendelser ble analysert ved termisk gravimetrisk analyse (TGA). Elektronmikroskop (SEM) ble bruk for å se på topografi, og kjemisk miljø rundt kobolt ble bestemt av røntgenabsorpsjon.

Abbreviations

APD	Ambient Pressure Drying
Co	Cobalt
Co-gel	Cobalt gel
$Co(C_2H_3O_2) \cdot 4H_2O$	Cobalt acetate tetrahydrate
$Co(NO_3)_2 \cdot 6H_2O$	Cobalt nitrate hexahydrate
CP	Co-precursor
BET	Brunauer-Emmet-Teller
BJH	Barrett-Joyner-Halenda
DSC	Differential Scanning Clorimeter
ESRF	European Synchrotron Radiation Facility
EXAFS	Extended X-ray Absorption Fine structure
Fe	Iron
FF	Fourier Filtering
FT	Fourier-Transform
FT-IR	Fourier-Transform Infrared
F-T	Fischer-Tropsch
HF	Hydrofluoric acid
HNO_3	Nitric acid
HMDZ	Hexamethyldisilazane
HMDSO	Hexamethyldisiloxane
ICP-MS	Inductively Coupled Plasma-mass spectrometry
IEP	Isoelectric Point
IWI	Incipient Wetness Impregnation
MS	Mass Spectrometer
Na_2SiO_3	Sodium silicate
NH_3	Amomonia
NH_4OH	Amomonium hydoxide
Ni	Nickel

Pd	Palladium
PEMFC	Proton-Exchange Membrane Fuel Cell
PZC	Point of Zero Charge
Rh	Rhodium
SA	Silicic Acid
SD	Surface Derivatization
SCD	Supercritical Drying
SEM	Scanning Electron Microscopy
Si	Silicon
SiO^-	Siloxy anion
SiOH	Silanol
$Si(OH_4)$	Silicic acid
$Si(OR)_4$	Silicon alcoxide
SSHC	Single-Site Heterogeneous Catalyst
TEOS	Tetraethyl Orthosilicate
TGA	Thermogravimetric Analysis
XRD	X-ray Diffraction
XAS	X-ray Absorption Spectroscopy
XANES	X-ray Absorption Near Edge Structure

December 7, 2017

Contents

1 Introduction

Over the last century, technological advances has caused a tremendous rise in human impact on the planet. The main source of energy in the world today is the burning of fossil fuels such as oil, natural gas and coal, and emission of greenhouse gases, mainly carbon dioxide (CO_2), is causing a global temperature rise. With this follows a vast variety of problems such as wilder weather, melting of polar ice caps, rising ocean levels and increasing extinction rates in plants and animals. The urgent need for a shift from fossil fuel based energy sources has caused an astonishing increase in research on cleaner, renewable and carbon free energy sources.

One such clean energy source is hydrogen gas for use in fuel cells in cars and other vehicles, and upon energy extraction only produces water as a byproduct. However, despite the rise of interest in the use of hydrogen as an energy source and it being the best fuel performance wise, several obstacles remains until it can see any wide usage. Easy, cheap and safe methods for storage and transport are lacking, and the primary constraint allowing for hydrogen fuel cells to become common is its low volumetric density. Using ammonia (NH_3) as the hydrogen carrier has therefore seen much interest lately as it is the second most produced chemical in the world, which has lead to a well established transport infrastructure. Ammonia is also easy to liquefy, safer to store and handle, is carbon free, has a relatively high hydrogen content (17 wt.%) and is readily available.[1,2]

On-site production of hydrogen from ammonia is considered a possible solution to the storage and transport problems hydrogen has. This does however, demand economically viable, lightweight and effective catalysts to convert ammonia to hydrogen trough ammonia decomposition for fuel processing. The conventional method of using large and slow converting fixed bed reactors does not meet the criteria for such usage and other types of reactors has to be developed.[2]

Catalytically active transition metals supported on porous materials such as zeolites, zeotypes, alumina, and silica are light weight and possible candidates. These types of catalysts are unfortunately prone to deactivation trough sintering effects of the dispersed metal. However, a newly developed method for producing highly porous silica aerogels as a catalyst support

material with cheap precursors such as sodium silicate instead of expensive silicon alcoxides, has shown great promise in heterogeneous catalysis. This route also applies an easier drying method at ambient pressure by hydrophobic surface modification (APD method) compared to the conventional supercritical drying method (SCD method). An active catalyst metal is easily introduced and incorporated into the silica aerogel structure and stabilized by simply adding a metal salt during the synthesis. Silica aerogels with incorporated copper in so called single-site position prepared through this method has been shown to be active in deNO$_x$ reactions. Single-site catalysts (SSC) provide high accessibility of the active phase, and incorporation into a porous support such as porous silica aerogels provide a good environment for catalytic reactions.[3]

Catalysts based on cobalt has long been known to be active in decomposition of ammonia, it is fairly cheap and is commonly used industrially.[4] However, single-site cobalt supported on silica aerogels prepared through this newly developed method, could provide a cheap and easy method for producing lightweight catalysts demanded by on-site hydrogen production. In this thesis, the goal was to attempt to synthesize hydrophobic silica aerogels with cobalt incorporated in single-site through the newly developed method for ammonia decomposition. This has never been done before and several parameter studies were performed to investigate the possibility of such incorporation.

2 Theory

2.1 Silica aerogel

Silica aerogel is an ultralight porous amorphous material with an open-structure consisting of up to 99% air and is derived from a gel where the pore liquid has been replaced with air. Aerogels have been know since 1931 when S. S. Kistler synthesized the first silica aerogel and coined the term aerogel.[5] The material features properties such as high surface area (500-1200 cm^3/g), high porosity (80-99.8 %), low density (0.003-0.05 g/cm^3), high thermal insulation (0.005 W/m K), ultra low dielectric constant (k = 1.0-2.0) and low refractive index (~1.05). Because of these properties, silica aerogels have a wide range of uses such as insulation in spacesuits, space dust collectors, dielectric materials, lightweight optics, chemical sorbents, carrier material in catalysis and many more.[6,7] Silica aerogels are also sometimes called "frozen smoke" or "solid air" due to its ultralight weight and translucency.

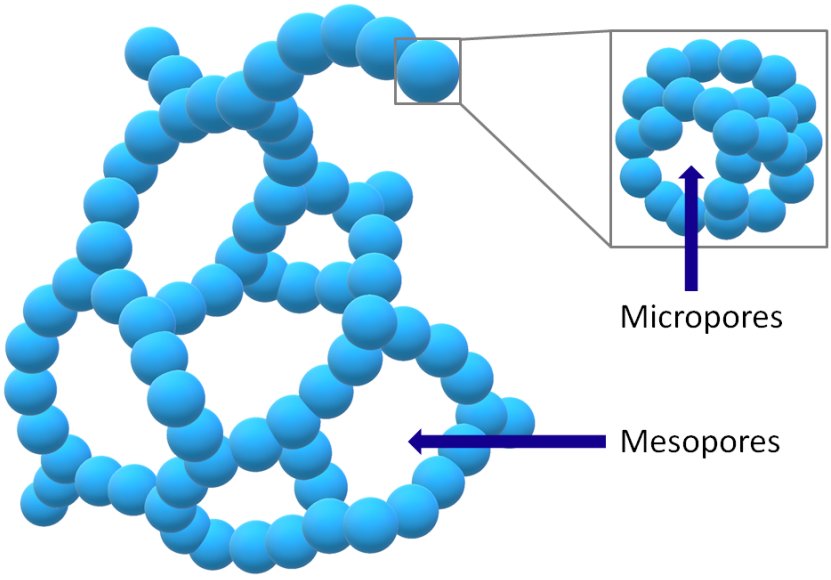

Figure 2.1: Drawing of the silica aerogel structure showing the interconnected silica particles and the pore structure.

The gel structure of silica aerogels consists of 2-6 nm sized silica particles called primary particles, which are clumped together to form bigger agglomerates called secondary particles.

These secondary particles are interlinked into long chains making up an interconnected pore system. The pore system consist of mostly mesopores (2-50 nm) but also micropores (>2 nm), where the micropores are irregularities in the packing of primary particles and the mesopores are larger voids between the interlinked secondary particles.[6,8] The network structure can be seen illustrated in figure 2.1. A SEM image of the structure can be seen in figure 2.2.

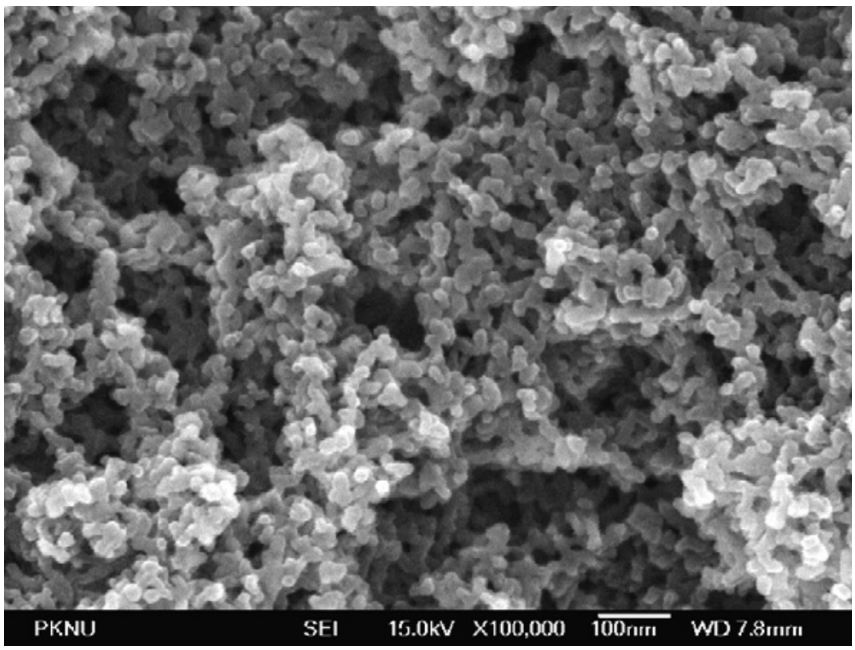

Figure 2.2: SEM image of the silica aerogel structure showing the interlinked spherical secondary particles. Reprinted with permission from Elsevier.[9]

Pore size, surface area and gel structure can be varied by how the gel is being prepared. Different silica precursors, pH, temperature and drying processes are some conditions that can influence the final product. Another material very similar to aerogels are xerogels, a denser version of the aerogel that only has micropores.[10] The higher density of xerogels is a result of the pore structure having collapsed in on itself due to the method it has been prepared. The process of preparing the aerogels and xerogels are identical up to the point of drying, which is the critical step that decides whether the gel becomes an aerogel or xerogel. If the wet gel structure is preserved after drying the resulting product will be an aerogel. If the wet gel structure has collapsed the resulting product will be a xerogel.[11] This type of gel has a reduction in volume by a factor of 5 to 10 compared to the original wet gel and the pores will be mainly micropores.[12] Different methods of drying are closer described in chapter 2.1.2 and 2.1.3.

2.1.1 Preparation

Making silica aerogels begin with the preparation of a wet gel by the sol-gel method, where a dispersion of silica colloids is catalyzed to start polymerizing, forming a rigid gel.[12,13]

Several silica precursors exist for preparing silica aerogels through the sol-gel method. Traditionally, a silicon alkoxide ($Si(OR)_4$) such as tetraethyl orthosilicate (TEOS) is used where the alkoxide is hydrolyzed in the presence of water and an acid or base catalyst. Alkoxyl groups are exchanged with hydroxyl groups, producing ($Si(OR)_x(OH)_y$) (x + y = 4) with alcohol as a by-product, rendering the silanol active for polymerization.[13] An illustration of the hydrolysis process where one of the hydroxyl groups is exchanged can be seen in figure 2.3.

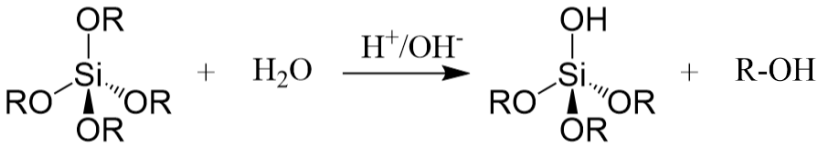

Figure 2.3: Reaction showing the hydrolysis of a silicon alkoxide catalyzed by H^+ or OH^-.

Another commonly used silica precursor is sodium silicate (Na_2SiO_3), also known as waterglass. Interest in the use of sodium silicate for making aerogels has risen significantly recently due to its low cost and low toxicity compared to alkoxides. Combined with the ambient pressure drying method (APD), this synthesis route makes it easier and much more cost effective for both research and production on an industrial scale. The method of drying gels at ambient pressure is described in chapter 2.1.3.

When using sodium silicate as a precursor, silicic acid (SA, $[SiO_x(OH)_{4-2x}]_{n-}$) is made by converting the sodium silicate by ion-exchange of Na^+ with H^+. This is done by passing an aqueous solution of sodium silicate through a column filled with an acidic resin, commonly a polystyrene sulfonate based resin, which produces a wide range of different silicic acid species. For simplicity, silicic acid will be represented as $Si(OH)_4$. The reaction forming silicic acid is shown below.

$$Na_2SiO_3 + 2H^+ \longrightarrow H_2SiO_3 + 2Na^+ \tag{2.1}$$

$$H_2SiO_3 + H_2O \longrightarrow Si(OH)_4 \tag{2.2}$$

The polymerization of the silica monomers ($(Si(OR)_x(OH)_y$, y $\geq$ 1) formed from either alkoxides or ion-exchanged waterglass, is acid or base catalyzed through a process called condensation where two monomers interlink by forming a -(Si-O-Si)- bond and water as a by-product.[12–14] This process can be seen illustrated in figure 2.4.

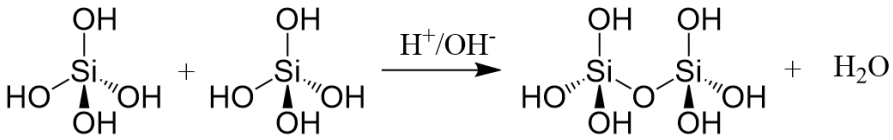

Figure 2.4: Reaction showing the condensation of silisic acid catalyzed by H^+ or OH^-.

For monomers with multiple silanol groups such as $Si(OH)_4$, condensation can happen at several -(OH) ligands simultaneously in a process called polycondensation.[12,13] The interlinking of monomers then continues producing dimers, trimers, etc. resulting in small silica particles. It is through polycondensation primary particles are produced. Condensation of terminal silanol groups on the primary particles forms the larger secondary particles which are interlinked by further condensation to form the continuous silica network.

The silica gel structure can also be tailored by controlling different parameters in the synthesis. Some of the most important parameters that can affect the gel structure significantly is the use of catalyst and pH at which the gel is formed. Particle growth is highly dependent on the kinetics of the condensation at a given pH and is divided into three approximate pH domains: pH < 2, pH 2-7 and pH >7. The isoelectric point (IEP) and point of zero charge (PZC) of silica is in the range of pH 1-3 and act as a boundary. At pH >7 the solubility of silica is maximized and serves as another boundary.[12] A relationship of pH and reaction rate of condensation and hydrolysis can be seen in figure 2.5.

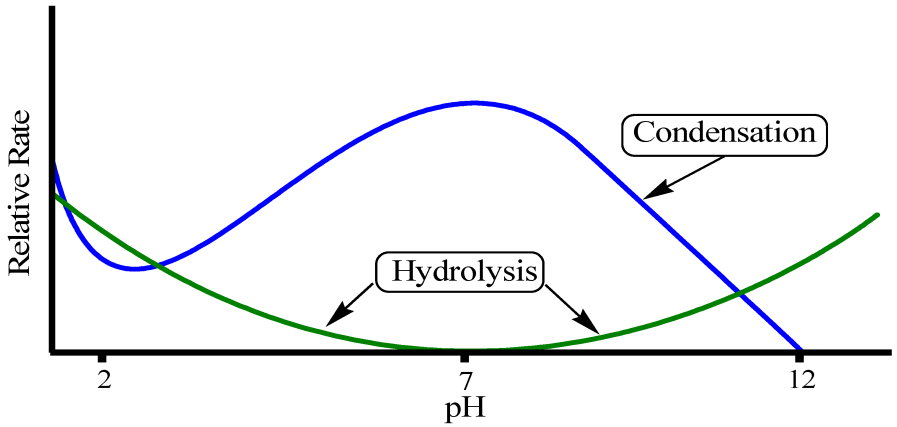

Figure 2.5: Effect of pH on the reaction rate of condensation and hydrolysis.[14]

For a gel where the condensation is acid-catalyzed, the first step (equation 2.3) is an electrophilic attack of the proton on the silanol that protonates and positively charges the oxygen on the silanol. The formed -OH_2^+ is a good leaving group as the electron density shifts from the Si atom. In the next step (equation 2.4), a siloxane bridge is formed between a protonated and unprotonated silanol, releasing a hydronium ion to start the cycle over again.

$$\equiv Si-OH + H^+ \xrightarrow{\text{fast}} \equiv Si-OH_2^+ \tag{2.3}$$

$$\equiv Si-OH_2^+ + HO-Si\equiv \xrightarrow{\text{slow}} \equiv Si-O-Si\equiv + H_3O^+ \tag{2.4}$$

At low pH, the solubility of silica is low and condensation occurs mostly between highly condensed and less condensed, neutral silica species through aggregation. Particle growth is greatly reduced when a size of 2-4 nm is reached due to the low solubility of silica at low pH and the size-dependence of solubility.[12–14] Acid-catalyzed gels therefore tend to produce weakly branched and fibrous "yarn-like" silica chains as illustrated in figure 2.6.

For a gel where the condensation is base-catalyzed, the first step (equation 2.5) is an abstraction of the proton of a silanol by the hydroxide ion. This produces a siloxide ion (SiO^-) and water. An attack on the Si atom of another silanol from the siloxide ion forms the siloxane bridge and releases the hydroxide ion to start the cycle over again (equation 2.6).

$$\equiv Si-OH + OH^- \xrightarrow{\text{fast}} \equiv Si-O^- + H_2O \tag{2.5}$$

$$\equiv Si-O^- + HO-Si\equiv \xrightarrow{\text{slow}} \equiv Si-O-Si\equiv + OH^- \tag{2.6}$$

At higher pH, the solubility of silica is high and the condensed silica species are easily ionized by the hydroxide ion. This causes higher repulsion between condensed silica species and particle growth occurs primarily by monomers linking with larger highly condensed species through Ostwald ripening. Base-catalyzed gels therefore tends to produce a larger particulate network with a higher degree of branching and higher porosity than acid-catalyzed gels as illustrated in figure 2.6.[12–14]

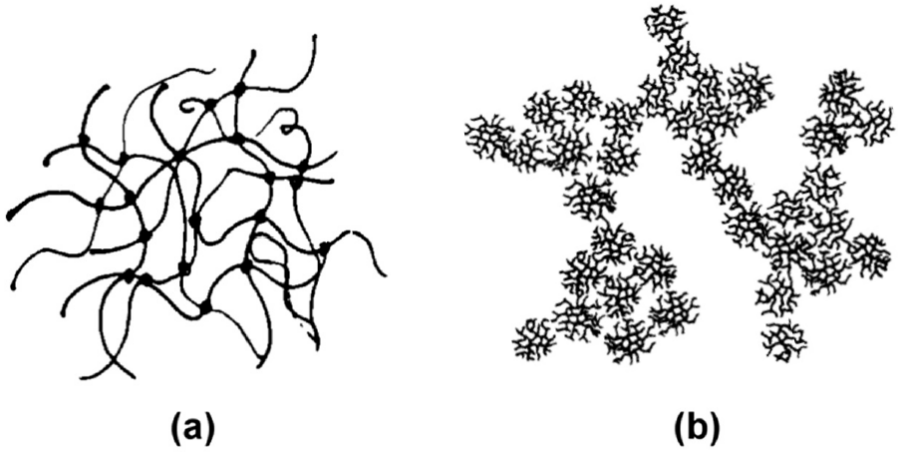

Figure 2.6: Wet silica gel structure from acid-catalyzed sol (a) and base-catalyzed sol (b). Reprinted with permission from Elsevier.[15]

In this thesis, gels will be made by using waterglass as precursor. Both acid and base-catalyzed gels will be made, inspired by previous work by T. Kristiansen.[3]

2.1.2 Supercritical drying (SCD)

Super critical drying is the conventional method for replacing the pore liquid of a wet gel with a gas to produce an aerogel by taking advantage of the properties of a supercritical fluid. This is achieved through two different routes: high-temperature drying and low-temperature drying.[11,16]

High-temperature drying uses an organic solvent, commonly an alcohol (methanol or ethanol), in which the wet gel is soaked several times to remove water inside the pores. The removal

of water is crucial as silica is soluble in supercritical H_2O and would destroy the gel structure. When the gel pores contains only alcohol, it is placed inside a pressure vessel filled with the alcohol and the pressure vessel is heated past the critical temperature (T_c) and critical pressure (P_c) of the alcohol used. Due to the lack of a liquid-gas boundary in the supercritical phase of the alcohol, capillary forces are non-existent. The vessel is depressurized isothermally, removing the alcohol from the pores as a gas, preserving the structural integrity of the gel. This route, however, is fairly dangerous as it involves flammable or explosive solvents at high temperatures and pressures.

Low-temperature drying is similar to high-temperature drying, but uses non-flammable solvents such as carbon dioxide as the supercritical fluid. The wet gel is first soaked in an organic solvent to remove water, just as for the high-temperature route. Instead of placing the wet gel in the same organic solvent that is in the pores, the gel is placed inside the pressure vessel filled with liquid carbon dioxide. The liquid carbon dioxide diffuses into the pores and replaces the organic solvent, which has a low critical temperature compared to that of for example methanol and ethanol (T_{c,CO_2} = 31 °C, $T_{c,MeOH}$ = 240 °C, $T_{c,EtOH}$ = 241 °C). The vessel is then heated beyond T_c and P_c of carbon dioxide and depressurized isothermally to achieve the aerogel. Even though the SCD method produces aerogels that preserves the gel structure very well which argues for its use, it is very expensive, dangerous and difficult to upscale for industrial use.[7]

2.1.3 Ambient Pressure Drying (APD)

Ambient pressure drying (APD) method is a process in which a wet gel is dried at ambient pressure. It is less dangerous, more cost-effective and requires less expensive equipment than the conventional method of supercritical drying (SCD). However, drying of a wet, unmodified and hydrophilic gel at lower temperatures and pressures than the supercritical point of the pore liquid will result in shrinkage and collapse of the pore structure, giving a xerogel. For example, hydrogels prepared from waterglass which contains water in its pores, will experience an inwards compressing force as the water evaporates due to the surface tension of water and capillary forces exerted on the gel structure.[17–19]

As water evaporates, porewater spreads on the gel surface because of the higher energy of

the solid/vapor interface (γ_{SV}) compared to the solid/liquid interface (γ_{SL}). Tensile stresses in the water and compressive stresses start to act on the gel structure, shrinking the gel. The meniscus of the liquid/vapor interface gradually disappear into the gel during the evaporation of the water, compressing and stiffening the gel in the process.[19] The compressing of the gel and the receding meniscus can be seen illustrated in figure 2.7.

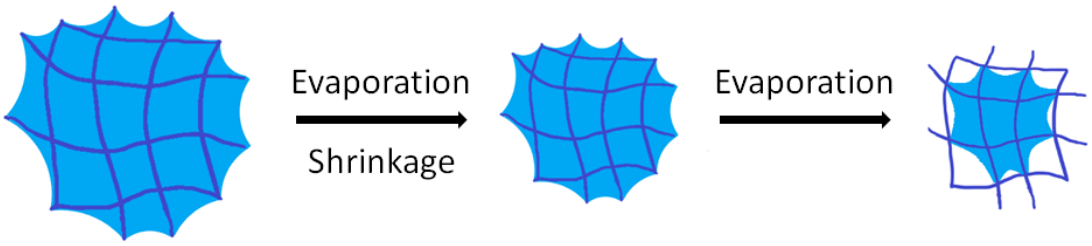

Figure 2.7: Shrinkage of the gel and the receding meniscus as porewater evaporates.

Tensile stresses in the water is related to the radius of the meniscus in the pore (r_m), and the surface tension of the solid/vapor interface (γ_{SV}) and the solid/liquid interface (γ_{SL}):

$$P_E = \frac{2(\gamma_{SV} - \gamma_{SL})}{r_m} \tag{2.7}$$

When most of the water has evaporated and the maximum curvature of the meniscus is reached ($r_{meniscus} = r_{pore}$), maximum capillary pressure is exerted on the gel structure, stopping the shrinkage. At this point, called the falling rate period, the evaporation rate of water is decreased due to the decreased vapor pressure as a result of the increased meniscus curvature.[19] The capillary pressure in the pores is related to the pore volume (V_P), surface area of the pore (S_P) and the surface tension of the solid/vapor interface (γ_{SV}) and the solid/liquid interface (γ_{SL}):

$$P_E = \frac{(\gamma_{SV} - \gamma_{SL})S_P}{V_P} \tag{2.8}$$

Shrinkage experienced by a dried unmodified gel is an irreversible process, as the silanol groups on the gel surface will start to cross-link through condensation, stiffening the gel structure even further resulting in a high density xerogel.[19] Therefore the APD method relies on a modification of the wet gel surface to make it hydrophobic by swapping the surface silanol

groups with an organosilane by the use of a silylation agent and exchanging the porewater to a solvent with a lower surface tension, typically an organic solvent such as heptane or hexane. By modifying the surface, capillary forces and tensile stresses are greatly reduced and further condensation is inhibited, preserving the gel structure when dried.[11] Common silylation agents such as hexamethyldisilazane (HMDZ) and hexamethyldisiloxane (HMDSO) are introduced to the gel during the synthesis which can be a one-step process where the the replacement of porewater and silylation takes place simultaneously, or a two-step process where the porewater is exchanged prior to the silylation.[17,20] These two methods are described in chapter 2.1.5 and 2.1.4 respectively. An illustration of the reaction with surface silanols and HMDZ and HMDSO can be seen in figure 2.9, where silanol groups are exchanged with trimethylsilane.[21]

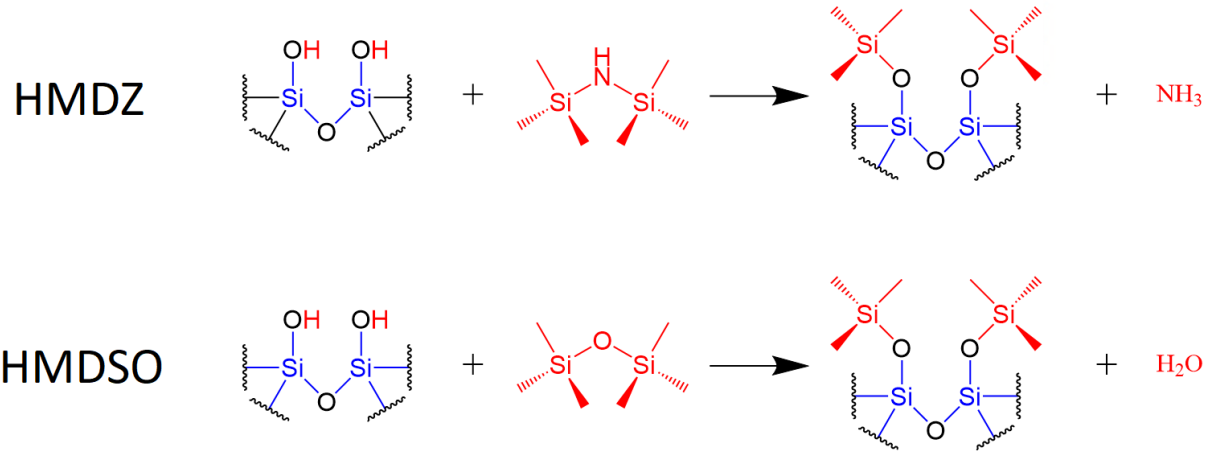

Figure 2.8: The two different reactions between surface silanols and silylation agents HMDZ and HMDSO, replacing silanol with trimethylsilane.

HMDZ and HMDSO are not water miscible and react with surface silanols in the water-organic interface. As the silanol groups are gradually replaced with trimethylsilane groups, the hydrophobic surface pushes the porewater out, replacing it with the organic solvent. The process is illustrated in figure 2.9. Although the surface tension between the surface of a modified gel and the organic solvent is significantly lower than for an unmodified gel and water, it is not completely free from compressive forces. The organic solvent will cause a small amount of shrinkage when the gel is dried, however, the process is reversible. The surface is also made inert by the trimethylsilane groups, inhibiting cross-linking of silanol groups that would cause the gel to get denser. This re-expansion of a dried modified gel is called the spring back effect.

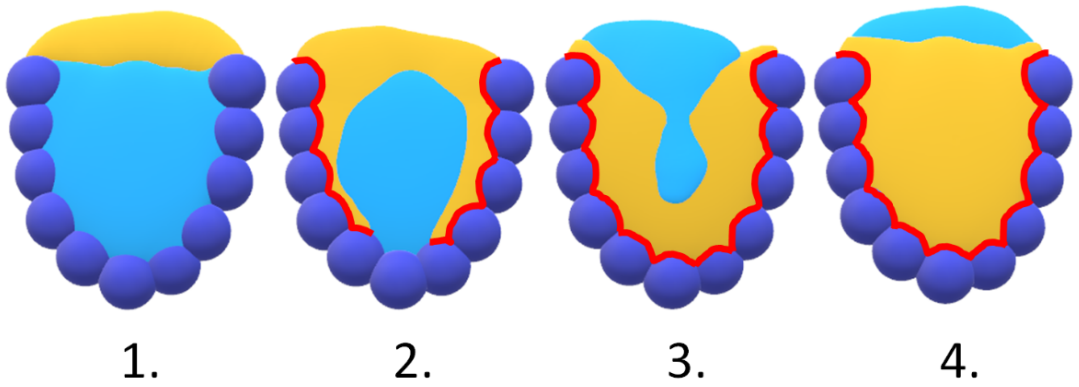

Figure 2.9: Illustration of the water (blue) being expelled from the pores and replaced by heptane (orange) as the surface becomes hydrophobic from trimethylsilane groups (red). The stages show the gel before silylation (1.), partial silylation (2.), near complete solvent exchange (3.) and complete silylation and solvent exchange (4.).

The silica aerogels prepared by the APD method usually exhibit lower porosity compared to those prepared by the SCD method due to incomplete modification of the surface silanols. Depending on the application of the aerogel, one would have to evaluate the different advantages and disadvantages of each drying methods to decide which would produce an aerogel with the minimum requirements for the application in mind. The advantage of the APD method is the significantly lower cost and easy scalability whereas the SCD method is expensive and difficult to scale, but produces aerogels with much higher porosity. All gels in this work will be dried using the APD method.

2.1.4 The Surface Derivatization (SD) method

Surface derivatization is a two-step method where the surface modification of a gel is performed by immersing the wet gel in a bath of the silylation agent and a solvent, commonly heptane or hexane.[13,22,23] The surface modification in the SD method is driven by diffusion of the silylation agents into the pores of the gel after it has set. An excess of silylation agent is added due to some of it being consumed in side reactions (equation 2.9) which causes the SD method to be quite expensive.[21]

$$(CH_3)-Si-NH-Si-(CH_3) + H_2O \rightleftharpoons (CH_3)-Si-O-Si-(CH_3) + NH_3 \quad (2.9)$$

Avoiding the usage of large amounts of silylation agent could be done by applying a washing procedure, removing porewater prior to the surface modification. The gel is soaked in an organic solvent in which water is miscible, e.g. ethanol repeatedly to completely remove the porewater. Subsequently the surface modification in the silylation agent and solvent bath can be performed without using the silylation agent in a large excess.

Although washing the gels prior to surface modification can reduce the usage of silylation agent, the amount used is still significant. In addition, the preparation time is increased due to the repeated washing of the gel.[24] The SD method does however have the advantage of easy control over the pH at which the gel is catalyzed.

2.1.5 The Co-precursor (CP) method

The co-precursor method is a one-step method for modifying the surface of the wet gel by adding the silylation agent directly to the sol prior to gelation and was first applied in combination with the APD method on waterglass based aerogels by Bhagat et. al in 2006.[25–27] It has been proven to produce aerogels at similar porosity and higher hydrophobicity than gels prepared with the SD method[17,28,29]

The addition of silylation agents directly to the sol while stirring vigorously ensures an even distribution of silylation agent inside the pores when the gel sets. Vigorous stirring is important as common silylation agents such as HMDZ and HMDSO are not miscible in water. The choice of silylation agent such as HMDZ could also act as a base catalyst as HMDZ reacts with water in the water-HMDZ interface (equation 2.9) or silanol groups on the gel surface (figure 2.8) to produce ammonia as a by-product. A one-step procedure for surface modification and solvent exchange is performed after gelation by immersing the gel in an organic solvent, commonly heptane or hexane, while the silylation continues. Controlling the pH at which the gel is catalyzed is somewhat more difficult with the CP method compared to the SD method if only HMDZ is used due to side reactions with water. Swapping some of the HMDZ with HMDSO, which is pH neutral, could give more control as not so much ammonia is produced, but the pH will still be within a range and not a specific value.[3] Completely replacing HMDZ with HMDSO has proven to not give sufficient modification of the surface and would result in a hydrophilic and high density gel.[30] The CP method has however the advantage of reducing

the amount of silylation reagents used significantly and reduces the total synthesis time as the repeated washing of the gels is not necessary.[7]

2.2 Silica aerogel as catalyst support material

The efficiency of a catalyst depend on several factors where one of the most important is the dispersion of the catalytically active phase. In heterogeneous catalysis, the catalyst is commonly a solid material such as a transition metal and the reactants are gases. Only surface atoms of the catalytically active metal with low coordination and saturation is available to participate in a reaction, and it is therefore critical for the efficiency of the catalyst to have as high dispersion of the metal as possible.[31] The dispersion ratio, D_M, is given by the number of available metal surface atoms, N_{M_s}, in relation to the total number of metal atoms, N_{M_t}:[32]

$$D_M = \frac{N_{M_s}}{N_{M_t}} \tag{2.10}$$

Increasing the ratio is often achieved by dispersing the catalyst metal on a 3D porous carrier material with high surface area. This stabilizes the catalyst metal, reducing the degree of deactivation through sintering effects and provides better size control for the catalyst metal particles as well as for reactants and products depending on pore size.[33] Silica aerogels are a good alternative as carrier material due to their meso- and microporous nature governing the reactant and product selectivity, and the extremely high surface area, giving the possibility of a high dispersion ratio. Introducing cobalt to the silica aerogel matrix can be done through several different methods, however, in this work cobalt is tried introduced into the silica aerogel matrix in single-site position. This method is described in section 2.2.1.

2.2.1 Introduction of cobalt into silica matrix

Several different methods exist for introducing cobalt to the silica aerogel matrix, each with their advantages and disadvantages. One common method is incipient wetness impregnation (IWI) where a hydophilic silica aerogel is impregnated with cobalt by adding a solution of a dissolved cobalt precursor directly to the dried gel with a volume corresponding to the total

pore volume of the support.[34] The solvent and other volatiles are dried off and the catalyst is calcined to produce metal oxide particles in the pores. The metal loading for IWI is dependent on and limited by the solubility of the metal precursor in the solvent. It also depends on the conditions for mass transfer during the impregnation and the drying process, however, the IWI process is fairly easy and straight forward.[35]

Another method of introducing cobalt to the silica aerogel matrix, and also the method used in this work, is to incorporate the Co cations during the sol-gel process by dissolving a cobalt precursor in the sol prior to gelation.[36] The cobalt cations binds to the reactive siloxy groups (-Si-O^-) and are embedded in the gel matrix which stabilizes the cobalt cations and prevents migration.[37] Since the cobalt cations react with the siloxy groups, it is expected that base catalyzed gels have a higher uptake of cobalt than acid catalyzed gels, as is reported for copper incorporated silica aerogels.[38] Adding cobalt to the sol also ensures an even distribution of the Co cations and homogeneity on a molecular level where cobalt is positioned in a so called single-site, meaning no -Co-O-Co- species.[39] An illustration of a possible result of incorporating cobalt into the silica aerogel matrix is seen in figure 2.10. The amine group stems from the formation of ammonia when the surface is silylated with HMDZ.[3]

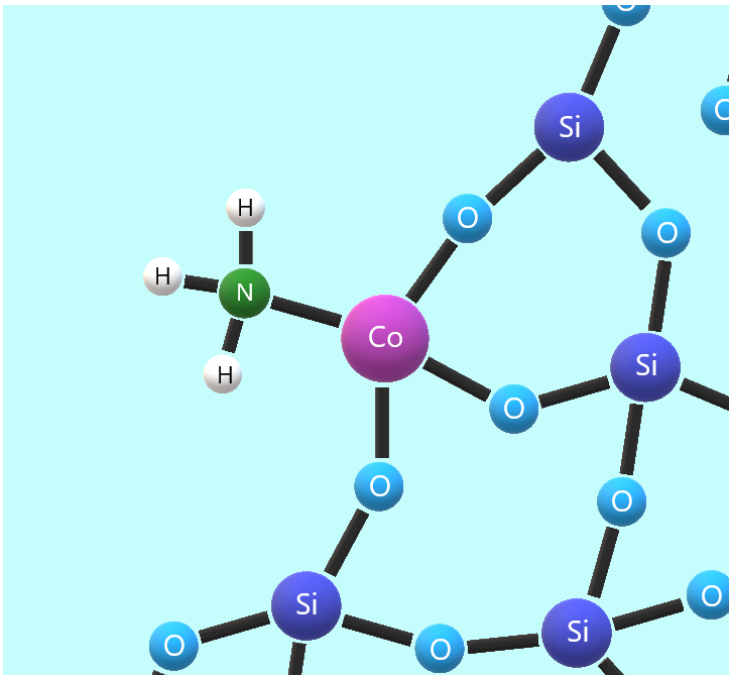

Figure 2.10: Single site cobalt with an amine group stemming from ammonia produced by silylation with HMDZ.

Ideally, all the incorporated cobalt are available on the surface of the silica aerogel, however, a problem encountered when preparing cobalt incorporated silica aerogels is the possibility of encapsulating the the metal in the silica matrix. This is due to condensation of silanol groups around the cobalt, rendering it unavailable for any catalytic processes, thus decreasing the dispersion ratio and the catalytic activity of the catalyst.[36] This undesired condensation can be reduced to an extent by creating hydrophobic surfaces with surface modification agents as explained in previous sections.

This type of catalyst with the active metal in single-sites, called single-site heterogeneous catalyst (SSHC), has seen use in several different reactions including hydration, isomerization, acetoxylation of olefins and oligomerization of dienes among many.[40] Earlier work on incorporation of transition metals such as vanadium,[41] iron,[42] copper[3,41] and cobalt[39] into silica aerogels has been attempted, however, most of these attempts have been done by preparing the wet gel from expensive precursors such as alkoxides and used supercritical drying to obtain the dry aerogel. T. Kristiansen proved it possible to incorporate transition metals into silica aerogels by another route, using cheap and commercially viable sodium silicate as the silica precursor and applying the APD method to obtain the aerogel. This route produced catalytically active single-site copper incorporated silica aerogel for the deNO$_x$ reaction, and these findings warrants similar investigation regarding other metals.[3]

One of the goals in this thesis is the incorporation of cobalt into single-site in the silica aerogel matrix for catalytic use. Cobalt has long been known to be catalytically active in several reactions, and the recent findings regarding copper lays the basis for this thesis. No work as ever been done on incorporating cobalt into silica aerogels in single-site via the recent sodium silicate and APD route, and the work in this thesis will therefore revolve around exploring how different parameters such as Co-loading, pH, concentration of silylation agents and precursor affect the silica aerogel and if single-site cobalt is possible through this route. Cobalt as a catalyst is described closer in section 2.2.2.

2.2.2 Cobalt as a catalyst

The Fischer-Tropsch (F-T) synthesis is a process where hydrogen gas and carbon monoxide gas is converted into hydrocarbons and is important for the production of lubricant oils, synthetic

diesel fuel and paraffin waxes among others.[34] The feedstock can either be hydrogen and carbon monoxide directly (equation 2.11 and 2.12), or derived from methane (equation 2.13) through steam reforming.

$$2nH_2 + nCO \longrightarrow C_nH_{2n} + nH_2O \tag{2.11}$$

$$(2n+1)H_2 + nCO \longrightarrow C_nH_{2n+2} + nH_2O \tag{2.12}$$

$$H_2O + CH_4 \longrightarrow CO + 3H_2 \tag{2.13}$$

The most common catalysts for the F-T synthesis are iron, ruthenium and cobalt, with ruthenium being the most active, especially for high molecular weight hydrocarbons.[43] However, ruthenium is a rare, noble metal and the high cost makes it preferable to use cheaper alternatives.

A growing interest for clean diesel and other fuels has drawn much focus towards the F-T process and research on cheap and effective catalysts. Catalysts based on cobalt has shown to be highly active in the conversion of CO and H_2 to long-chained high molecular weight hydrocarbons when the feedstock is methane, which can be used to produce clean diesel fuel.[34,39,44] This makes cobalt a good alternative to ruthenium based catalysts as the cost of cobalt is significantly lower.

One other area which has drawn much attention currently is on-site production of CO_x-free (x = 1, 2) hydrogen by ammonia (NH_3) decomposition:

$$2NH_3 \rightleftharpoons 3H_2 + N_2 \tag{2.14}$$

The need for clean hydrogen in applications such as proton-exchange membrane fuel cells (PEMFC) is important to reduce poisoning of the anode and the environment with CO_x. Hydrogen is commonly produced from carboniferous substances such as methanol and methane and will always contain a certain amount of CO_x, and for fuel cell applications even extremely small amounts (200 ppm) of CO_x is problematic.[45–48]

Hydrogen in its compressed liquid state has a low volumetric energy density compared to ammonia and is difficult to store on board fuel cell driven cars or other vehicles in a large enough amount. The weight fraction of hydrogen in ammonia is 17.7 wt.%, which is fairly high compared to other industrially used hydrogen carriers such as methanol (12 wt.%) and methane (25 wt.%). Even though ammonia does not have the highest wt.% of hydrogen, it eliminates any undesired CO_x that carboniferous substances produce, which makes it a good alternative. Ammonia also compresses from gas to liquid fairly easy at only ~10 bar at ambient temperature, has a lower flammability and lower explosion risk than compressed hydrogen and is readily available.[48,49] Sourcing hydrogen from ammonia instead of methanol or methane reforming is more economical and it is estimated an equilibrium conversion of ammonia at 99.1 % at 400 °C based on thermodynamic constants, where hydrocarbons such as methanol or ethanol yields lower conversion.[48,50]

As for the F-T synthesis, ruthenium has been reported in literature to have the highest activity in both ammonia synthesis and decomposition, and has been commercialized since the mid-1990s.[46,48,49] Ruthenium however, as a noble metal and its scarcity and high price limits any use on a large scale. Research on cheaper active metals has found that cobalt is active in ammonia decomposition, and recent research has shown cobalt to be even more active than ruthenium under certain conditions.[4] Sørensen et al. showed that under process conditions of 575 °C and 650 °C with a gas mixture containing 50 vol.% argon and 50 vol.% ammonia, alumina supported cobalt was the most active catalyst compared to other common catalysts such as Ru, Pd, and Fe.[51] Zhang et al. also found that carbon nanotube supported cobalt (4.1 wt.% Co) at 700 °C with a gas feed containing 100% NH_3 resulted in near complete conversion.[52]

Although cobalt catalysts are applicable in different chemical processes, the catalysis portion in this work will focus on the functionalization of single-site cobalt on silica aerogels for ammonia decomposition.

2.3 X-Ray Diffraction

X-ray diffraction is a non-destructive characterization technique that is used to identify the crystallographic structure and chemical composition in a material.[53] Long-range order in the

material is necessary, however, phase determination is not restricted to only single-crystals. XRD can also be used for measuring crystallites, then called powder x-ray diffraction (PXRD). An illustration of the principle behind XRD can be seen in figure 2.11

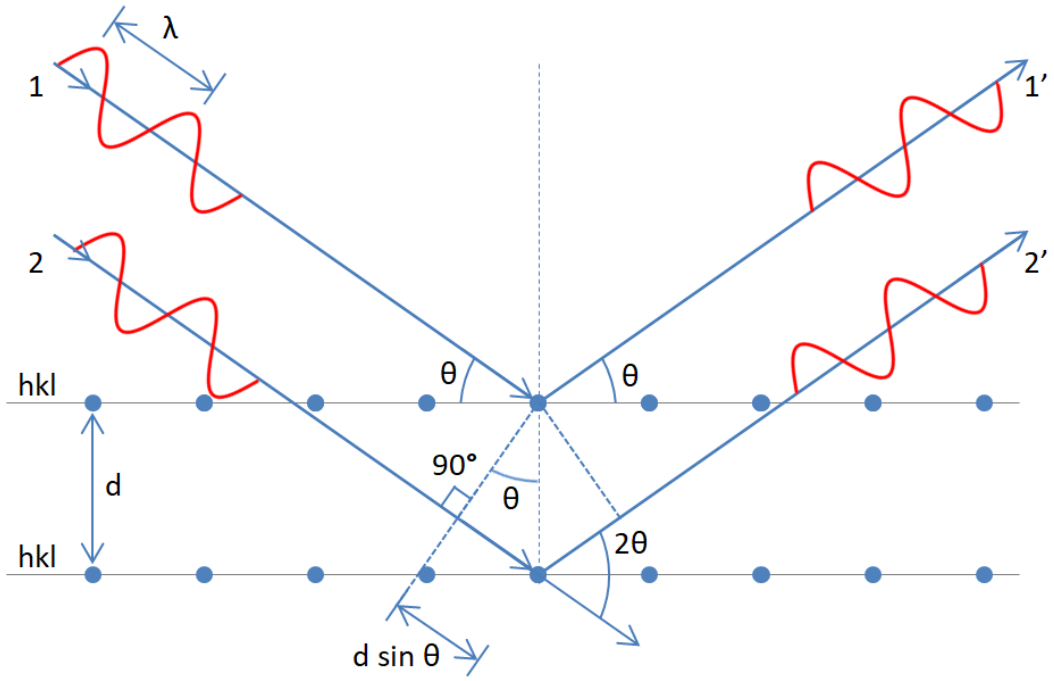

Figure 2.11: Illustration showing the principle of XRD. The incomming x-rays are diffracted when hitting the crystal planes giving either destructive or constructive interference.

Monochromatic x-rays are aimed at the sample and scattered by the atoms the lattice. The diffracted x-ray beams that are out of phase will result in destructive interference while those that are in phase will amplify through constructive interference, giving rise to a peak in the diffractogram. As seen from figure 2.11, beam 2 travels an extra distance of two times dsinθ. When this distance is equal to an integer of the wavelength λ, constructive interference is will result. This relation is given by Bragg's law

$$2dsin\theta = n\lambda; n = 1, 2, ... \tag{2.15}$$

where d is the distance between two lattice planes, θ is the angle between the x-rays and the lattice plane, n is an integer and λ is the wavelength of the x-rays. By measuring the angle θ at points of constructive interference, Bragg's law can be applied to find the lattice spacing d which is unique for every compund.

A limitation in characterization of catalyst materials with XRD is that many of the crystalline phases present may not show any well defined diffraction peaks, if any at all. A particle size requirement of >2 nm is necessary for any sharp diffraction peaks to show.[54] As a long-range order of the material is required, amorphous materials can not be characterized by XRD.

Although silica aerogels are amorphous, in this project XRD will be used to exclude the presence of any crystalline phases. Typically this can be unwanted metal species such as cobalt oxides (CoO_x) and cobalt silicate (Co_2SiO_4). Formation of these species would mean cobalt is not successfully incorporated into the silica aerogel. An example of an XRD pattern of amorphous silica can be seen in figure 2.12, which is the desired diffractogram of cobalt incorporated silica aerogel.

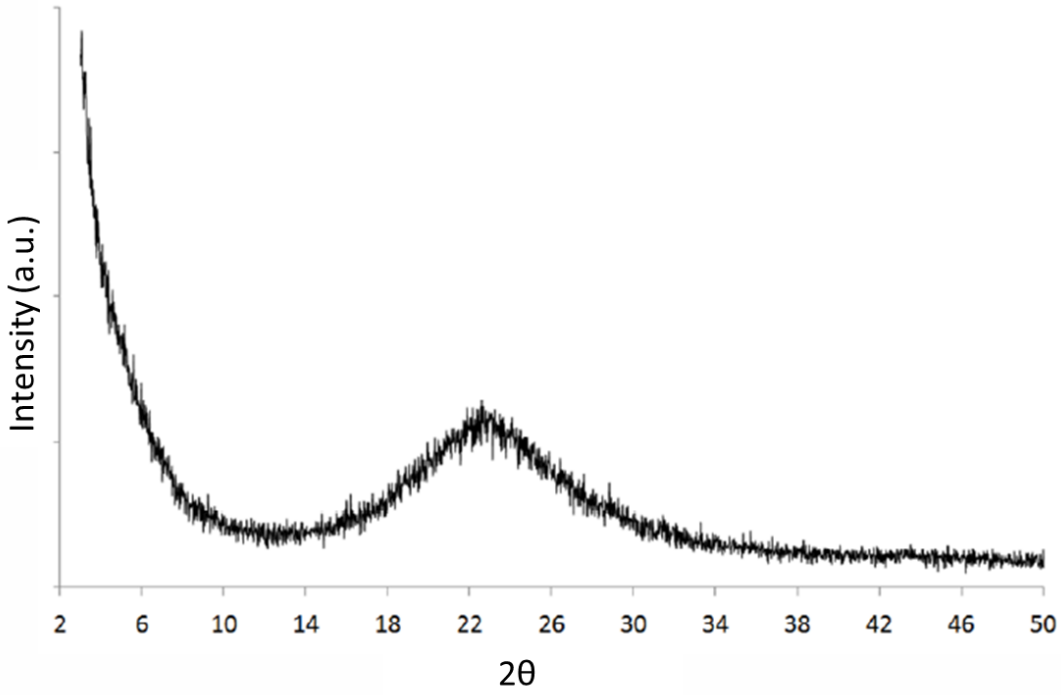

Figure 2.12: Diffraction pattern of amorphous silica.[55]

2.4 BET Theory

Brunauer, Emmet, Teller (BET) theory is commonly applied for determining the specific surface area of a porous material by the use of adsorption and desorption isotherms of an inert gas, usually nitrogen (N_2). Due to thermal motion and the uncertainties that follows, mea-

surements are done at a very low and constant temperature of 77K. At this temperature and atmospheric pressure, nitrogen is at its condensation point which makes it suitable for this application. Applying nitrogen as the probe gas, the nitrogen molecules are physisorbed on the surface forming a monolayer of a certain quantity. The area a single molecule of nitrogen covers is known, and by measuring the relative pressure p/p_0, where p is the adsorption pressure and p_0 is the saturation vapor pressure of nitrogen, in relation to the amount of adsorbed, surface area can be calculated.[53]

When analyzing the surface area of a sample, a variety of different isotherms may result, depending on the pore size and the shape of pores in the material. These isotherms have been classified by IUPAC and are divided into six different types depending on their shape. The isotherms as shown in figure 2.13.

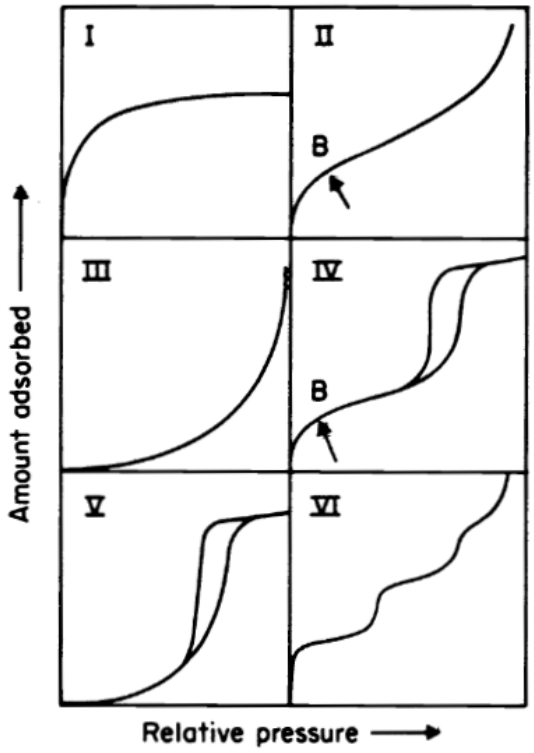

Figure 2.13: The six different isotherms, as classified by IUPAC.[56]

The most relevant isotherm for this project is type IV and is commonly seen for mesoporous materials and show a hysteresis loop. Point B on the isotherms shown in figure 2.13 is the point at which the adsorption of the monolayer is complete and multilayer adsorption begins.[56] The

hysteresis loop seen is the result of a shift in relative pressure that occur due to capillary forces that has to be overcome as nitrogen desorp. Hysteresis loops can take different shapes and are also classified by IUPAC. The different types of hysteresis loops can be seen in figure 2.14.

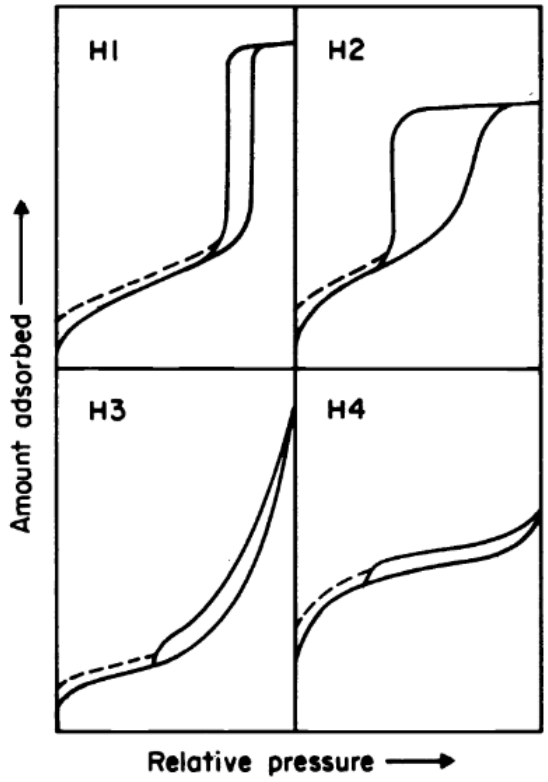

Figure 2.14: The four different hysteresis loops possible form BET measurements, as classified by IUPAC.[56]

Which factors are affecting adsorption isotherms are not fully understood, but the different shapes of the hysteresis loops are often seen in connection to the shape of the pores in a material. A narrow pore distribution and uniform mesopores are common for type H1. Type H2 is especially difficult to interpret. This type has been attributed to effects controlling the evaporation and condensation in pores with narrow necks and wide bodies, however network effects has to also be taken into account. Type H3 differs from the aforementioned types that it does not have any effects limiting the adsorption at high relative pressure and is seen in plate-like particles with slit-shaped pores. Type H4 is similar to H3 as it is a result of narrow slit-shaped pores, but when taking the shape of a Type I isotherm it is indicative of micropores.[56]

Information about the pore size distribution in a material can be found by applying the Barrett,

Joyner and Halanda (BJH) model which is an interpretation of the Kelvin equation.[57] The menisque of condensed nitrogen in the pores of a material is directly linked to the width of the pores, and taking the derivative of the BJH adsorption gives the most predominant pore width. For mesoporous silica aerogel, a type IV isotherm is expected.

In this project, BET is used to determine the specific surface area of the aerogels, and BJH is used to determine the pore distribution and average pore sizes.

2.5 Inductively Coupled Plasma- Mass Spectrometry

Inductively coupled plasma-mass spectroscopy (ICP-MS) a precise and accurate method of elemental characterization of virtually any material. The technique is able to yield elemental composition of a sample at extremely low concentrations, which can be as low as parts per quadrillion (ppq, 10^{-15}). The elements in the sample are ionized by inductively coupled plasma and passed through a mass spectrometer (MS). The MS determines the signal from each element passing through based on the mass-to-charge ratio (m/z), which makes it able to identify different isotopes as well as different elements.[58]

Even though the technique is sensitive to isotopes, the abundance of each isotope must be carefully considered as the mass-to-charge ratio of different isotopes can be similar. Other interferences as combining of plasma gas to form polyatomic species must also be taken into consideration.[59]

In this project, ICP-MS will be used for determining the cobalt content (wt%) in the silica aerogels.

2.6 Scanning Electron Microscopy

Scanning electron microscopy (SEM) is a technique used for imaging the topography and composition of a material by scanning the surface with an electron beam of high energy electrons. Images produced from SEM have very high resolution and can reveal details on the surface down to 1 nm. The electrons from the electron beam interact with the material in several

different ways producing signals that can be converted to an image where the most important type of signals are produced by secondary electrons and backscattered electrons. Signals produced from secondary electrons give information about the surface revealing details such as cracks, particle size and pores, while signals produced from backscattered electrons give information about the composition of the material due to their sensitivity to atomic number (Z).[60]

When applying SEM, it is important that the sample is conductive and grounded. Non-conductive materials will experience a build up of charge and cause the image to get disrupted appearing very bright. To avoid charging, the sample must be coated with a conductive material, typically graphite or gold. The layer has to be ultra thin to not obscure any surface features (~5 nm).[60]

In this project SEM will be used to observe the general structure and topography of the aerogels.

2.7 Thermogravimetric Analysis

Thermogravimetric analysis (TGA) is a method where weight loss is measured as a function of increased temperature and time. It is a useful method for measuring thermal decomposition, evaporation of volatiles, reduction and desorption. The technique is not only restricted to weight loss and can also be used for measuring weight gain during oxidation or adsorption. As all these are kinetic processes, the rate of which they occur will change during the analysis. The analysis is performed with a continuous gas flow during the heating of the material. The exhaust gas can be analyzed by connecting the TGA apparatus to a gas chromatography mass spectrometer (GC-MS), and thermal events can be monitored by differential scanning calorimetry (DSC).

In this project, TGA is used to observe weight loss during heating of the aerogels.

2.8 Fourier-Transform Infrared Spectroscopy

Fourier-Transform Infrared Spectroscopy (FT-IR) is a non-destructive analysis technique able to provide information about the chemical makeup of a sample, quality and consistency of a sample and the amount of different components in a mixture. The infrared spectrum is the molecular vibrational spectrum, and by irradiating a sample with specific wavelengths of infrared radiation, the sample molecules absorb the radiation, causing a change in the dipole moment. The initial vibrational energy level, or the ground state vibrational energy, is increased, transferring the molecules to an excited vibrational energy state. The difference in energy between the ground state and the excited state is the vibrational energy gap and determines the frequency of the absorption peak seen in the absorption spectrum. The wavelengths absorbed are specific for all molecules, resulting in FT-IR being a molecule fingerprint technique. The intensity of the absorption peaks are also related to the concentration of a molecule in a mixture, with higher intensity peaks indicating a higher concentration of one type of molecule. Although most molecules can be analyzed with FT-IR, homonuclear diatomic molecules, e.g. N_2 and H_2, are not detectable due to zero change in the rotational and vibrational dipole moment.[61]

In this project, FT-IR is used in combination with a tube reactor to measure the amount of decomposed ammonia (NH_3) as a function of temperature during catalytic testing of cobalt incorporated silica aerogels.

2.9 X-ray Absorption Spectroscopy

X-ray absorption spectroscopy (XAS) is a powerful technique that can provide information about element-specific local environments, oxidation states and coordination numbers of a target element in a material. It is also one of the very few techniques for structural analysis that does not require long-range ordering, making it a good analysis tool for non-crystalline and disordered materials such as silica aerogels. XAS is a bulk sampling technique, and all information obtained will be an average from all the target elements in the sample.[62] In this project XAS is used to determine if the Co cations are successfully incorporated into single-site

position in the silica aerogel matrix.

XAS takes advantage of the distinct values of binding energies of core electrons in an element. By irradiating the element with the appropriate x-ray energy, the core electrons absorb the x-rays through photo-absorption and the absorber gets ionized or the electrons are ejected as photoelectrons into the continuum. Ionizing the core electrons of an element does however require very high x-ray energies and XAS measurements are therefore performed at a synchrotron which can provide tunable x-ray energies at high intensity. This is achieved by accelerating electrons in a particle accelerator to near relativistic speeds and subjecting them to bending magnets and an undulator with alternating polarities which causes the electrons to oscillate and produce electromagnetic radiation. The radiation produced is sent from the synchrotron to a beam line, where it is adjusted by a series of slits and monochromators to fit the desired requirements for the experiment. A simplified illustration of the XAS setup can be seen in figure 2.15.

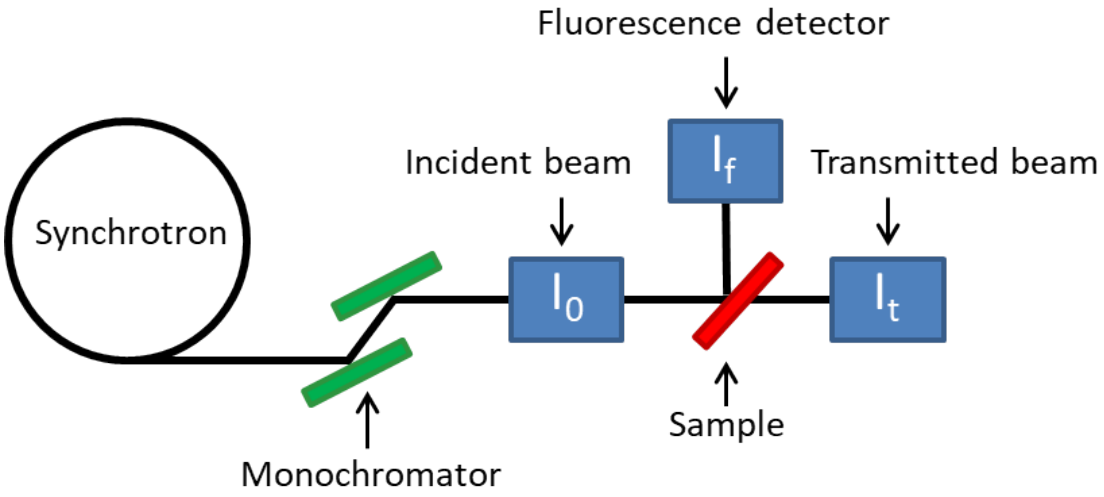

Figure 2.15

The radiation is passed through a monochromator to adjust the x-ray energy to the energy required to excite a core electron. The incident beam, I_0, passes through a detector which measures the intensity of the incident photons. Depending on the sample, data can be collected in fluorescence mode where the intensity of the fluorescence beam, I_f, is measured or in transmission mode where the intensity of the transmitted beam, I_t, is measured. For XAS measurements in transmission mode, the absorption of x-rays by the sample is given by the

absorption coefficient, μ, which can be calculated from Beer-Lambert's law:

$$\mu(E)x = ln\frac{I_t}{I_0} \tag{2.16}$$

where $\mu(E)$ is the absorption coefficient as a function of the x-ray photon energy, x is the sample thickness, I_t is the intensity of the transmitted beam and I_0 is the intensity of the incident beam.[63] In addition to the energy of the x-rays, E, the absorption coefficient is also dependent on the density of the sample, ρ, the atomic number of the target element, Z, and the atomic mass, A:

$$\mu(E) \approx \frac{\rho Z^4}{AE^3} \tag{2.17}$$

Since XAS is element specific, the x-ray energy is tuned to match the core electron bond energy of the target element. This will result in a sharp and abrupt increase in the absorption coefficient which corresponds the x-ray energy at the absorption edge, labeled E_0. Ionization of 1s core electrons are usually measured for cobalt and can be seen as an increase in the absorption at the K-edge, which for cobalt metal is at 7709 eV.[64]

When analyzing XAS data, only the part around the absorption edge is of interest and is confined to a range of ~1000 eV where the XAS spectrum is divided into two regions. The first region is the x-ray absorption near edge structure (XANES) which is the area including the pre-edge, a small absorption peak right before the absorption edge, and the absorption edge as well as all other edge features up to 50 eV above the absorption edge. The second region is the extended x-ray absorption fine structure (EXAFS) which is the area of the spectrum from 150 eV to 1000 eV above the edge. The positioning of E_0 is somewhat arbitrary and is commonly chosen to be the inflection point, i.e. the maximum in the first derivative of the absorption edge. This can, however, be problematic as electronic excitations and resonances can hide the exact position of E_0. Therefore E_0 is often chosen as half up (0.5) the normalized edge to avoid these problems.[63] In this project the position of E_0 is consistently chosen as 0.5 on the normalized edge for all samples and reference compounds, and at the inflection point for cobalt foil. An example of the XAS spectrum can be seen illustrated in figure 2.16.

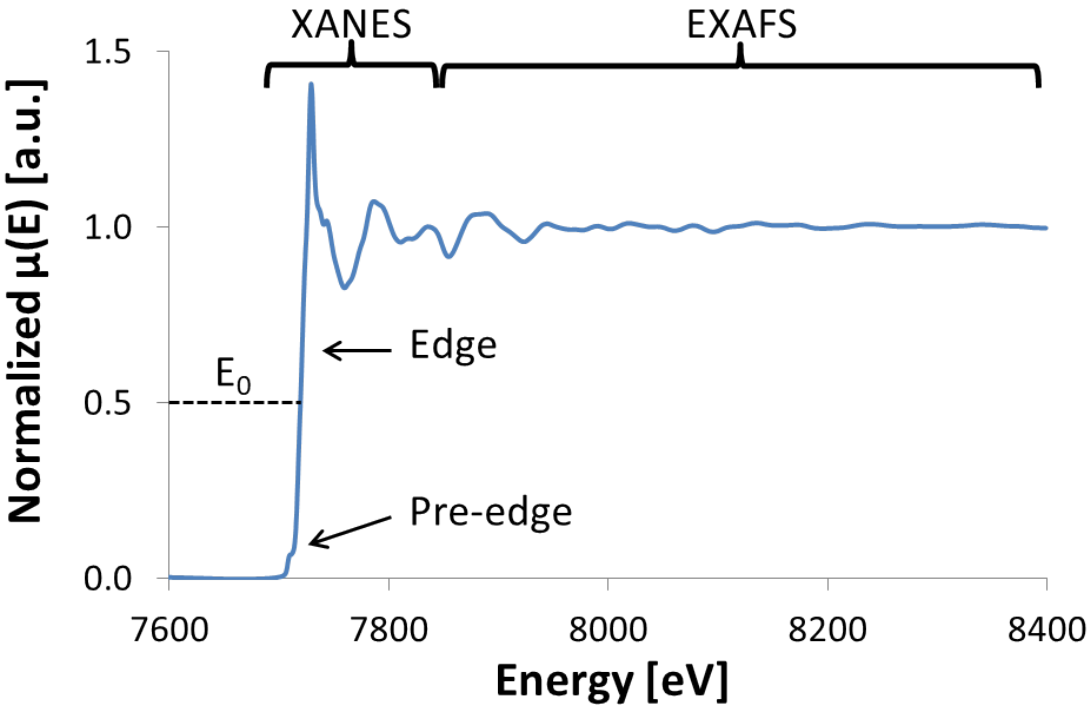

Figure 2.16: Illustration of a normalized XAS spectrum with Co_3O_4 as an example divided into the the XANES and EXAFS regions. The position of E_0 as defined as 0.5 on the normalized μ(E), the pre-edge and edge can also be seen.

2.9.1 X-ray Absorption Near Edge Structure (XANES)

A pre-edge is often seen in transition metals and can give information about site symmetry and oxidation state of the target element. This is due to an electronic transition of a core electron to a higher energy level, and for cobalt and other transition metals in the 4th period, the 3d states are only partially filled and can allow for a 1s $\rightarrow$ 3d transition, resulting in a pre-edge. The intensity of the pre-edge vary greatly depending on the Laporte selection rule and the number of unoccupied states in the d-orbital.[65] Example of pre-edges from some cobalt references can be seen in figure 2.18.

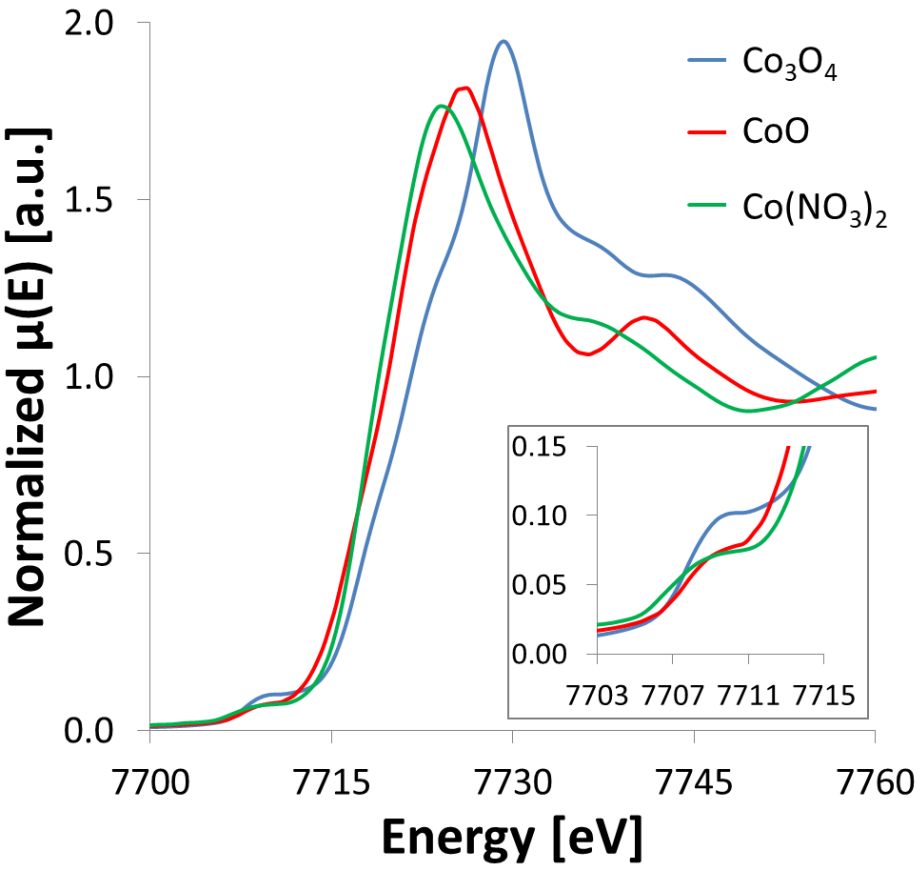

Figure 2.17: Illustration showing the absorption edge and pre-edge of Co_3O_4, CoO and $Co(NO_3)_2$ as an example.

The Laporte selection rule is a rule which governs the dipole electronic transitions in centrosymmetric molecules i.e. molecules with an inversion centre (i). Tetrahedral coordinated complexes does not exhibit this property and are therefore not affected by this rule while complexes with octahedral coordination which does have an inversion centre, are affected. The rule states that electronic transitions which does not conserve parity are allowed, while those who do are forbidden. This means that g $\rightarrow$ u and u $\rightarrow$ g transitions are allowed and g $\rightarrow$ g u $\rightarrow$ u transitions are forbidden, where g (gerade) is an even orbital function and u (ungerade) is an uneven orbital function. Electronic transitions forbidden by the Laporte rule are then s $\rightarrow$ s, p $\rightarrow$ p, d $\rightarrow$ d, f $\rightarrow$ f and s $\rightarrow$ d as they exhibit an inversion centre, while s $\rightarrow$ p, p $\rightarrow$ d and d $\rightarrow$ f are allowed as they do not exhibit an inversion centre.[3]

However, a forbidden transition such as s $\rightarrow$ d can still be allowed and is seen as a pre-edge in cobalt compounds in cases where the symmetry distorted. One such case involves complexes experiencing asymmetric vibrations where vibronic transitions can occur. Since symmetry is

not always perfect in complexes, these distortions causes forbidden transitions to occasionally happen and results in a weak pre-edge. As tetrahedral coordinated complexes are not affected by the Laporte selection rule, they tend to give a higher intensity pre-edge compared to octahedral coordinated complexes.[66]

The number of unoccupied 3d states governs the probability of a 1s-3d transition where a less filled 3d orbital has a higher probability than a highly filled 3d orbital for this transition, which also results in a higher intensity pre-edge. Different elements and different oxidation states will have varying occupancy of the 3d states, where e.g. Co^{2+} has 3 unoccupied states ($3d^7$) and will produce a lower intensity pre-edge compared to Co^{3+} which has 4 unoccupied states ($3d^6$) and will result in a higher intensity pre-edge.

For cobalt, XANES is usually studied from ~10 eV before the absorption edge to include the pre-edge. In the region after the pre-edge, the absorption edge, E_0, i.e. the ionization of a core electron is encountered. The position of E_0 in the XANES region exhibit sensitivity to formal oxidation state of the target element. At higher oxidation states, the electronic charge is reduced due to the removal of electrons. This absence of extra electronic charge causes a decreased shielding effect and an increased attraction between the nucleus and the electrons, thus, increasing the energy required for a core electron to be excited and shifts the position of E_0 to a higher value. For bulk metal oxides, the increase is linearly related to the oxidation state. However, the increase in E_0 is not only dependent on the oxidation state and is also affected by the coordination number, nature of the ligands, covalent character of the bond and electronegativity of the anion among others, which can also shift the position of E_0.[67,68] When determining the chemical nature of a sample, it is therefore important to compare the data from the sample to several different references with different oxidation states as well as some with the same oxidation state.

2.9.2 Extended X-ray Absorption Fine Structure (EXAFS)

At energies from the end of the XANES region and up to ~1000 eV above the absorption edge, the electrons are ejected as photoelectrons as a result of the photoelectric effect. The ejected photoelectrons will have a surplus kinetic energy equal to the difference of the absorbed en-

ergy and E_0 as seen in equation 2.18

$$E_k = h\nu - E_0 \tag{2.18}$$

where E_k is the kinetic energy of the photoelectron, $h\nu$ is the energy of the absorbed x-ray photon and E_0 is the absorption edge energy.[63]

The ejected photoelectrons can be represented by a spherical outgoing wave from the absorber atom which is backscattered when it collides with the neighboring atoms. The backscattered waves interacts with the outgoing waves creating destructive or constructive interference resulting in oscillations in the XAS spectrum. Where constructive interference happen, a peak is seen and where destructive interference happen, a valley is seen. Factors influencing the interference includes the distance from the absorber atom to its nearest neighbors, which element the neighbors are and the wavelength of the photoelectrons. Thermal and structural disorder can also dampen the amplitude of the EXAFS oscillations. Neighboring atoms to the absorber atom is often referred to as a shell when the bond distances are similar and the number of atoms in a shell is referred to as the multiplicity, N.[63] An illustration of the backscattering process can be seen in figure 2.18.

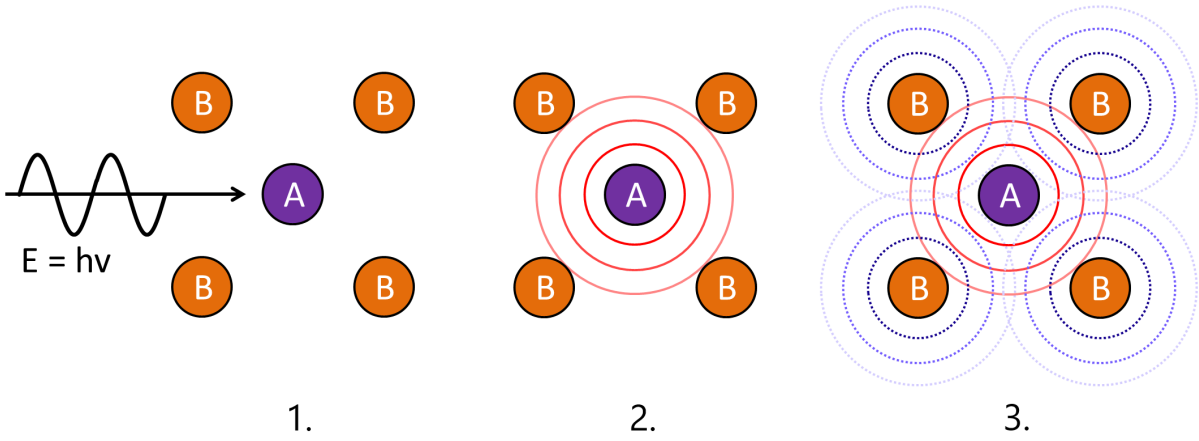

Figure 2.18: Illustration showing the incoming X-ray beam being absorbed by the target atom A and the resulting spherical photoelectron waves (red solid lines) being backscattered from the neighbouring atoms B (blue dashed lines).

EXAFS is the extraction of structural information resulting from the oscillations produced by the interaction between the photoelectron waves. Extracting the structural information from

these oscillations first involves isolating the EXAFS portion from the rest of the XAS spectrum and normalizing it, giving the function χ(E):

$$\chi(E) = \frac{\mu(E) - \mu_0(E)}{\Delta\mu_0(E)} \tag{2.19}$$

where $\chi(E)$ is the normalized EXAFS portion of the XAS spectrum, $\mu(E)$ is the absorption coefficient as a function of the x-ray energy E, $\mu_0(E)$ is the absorption for an isolated atom and $\Delta\mu_0(E)$ is the measured absorption jump at the absorption edge, E_0. Due to the photoelectrons being waves, the energy scale is commonly converted to the wave vector scale ($Å^{-1}$), represented as the wave number k:[62]

$$k = \sqrt{\frac{2m(E - E_0)}{\hbar^2}} \tag{2.20}$$

where m is the mass of an electron, $E - E_0$ is the kinetic energy of the electron as shown in equation 2.18 and $\hbar$ is the reduced Planck constant.[62] Due to oscillations rapidly weakening the amplitude of the signal at increasing values of k, $\chi(k)$ is often multiplied with a weighting factor k^n (n = 1, 2, 3), commonly k^3. This helps to adjust for high backscatter contribution from the first shell compared to shells further out from the absorber atom.

Information describing the structural nature of the sample is extracted by the use of the EXAFS equation; a theoretical expression of $\chi(k)$ which is based on the plane-wave single scattering approximation. This approximation uses the assumption that the atomic radii is much smaller than the interatomic distances, meaning the curvature of the photoelectron wave can be completely ignored which simplifies the equation. It also uses the approximation that the backscattered photoelectron wave is only backscattered once and that the path is directly from the backscatterer to the absorber.[69] The EXAFS equation can be seen below.

$$\chi(k) = S_0^2 \sum_{j=1}^{Shells} \frac{N_j}{kR_j^2} F_j(k) e^{-2k^2\sigma_j^2} e^{\frac{2R_j}{\lambda(k)}} sin[2kR_j - \phi_j(k)] \tag{2.21}$$

where

- S_0^2: Amplitude reduction factor
- N_j: Coordination number of shell j

- k: Wavenumber
- R_j: Interatomic distance between the absorbing atom and shell j
- $F_j(k)$: Back-scattering factor for an atom in shell j
- σ_j^2: Debye-Waller factor of shell j
- $\lambda(k)$: Inelastic mean free path of the photoelectron
- $\phi_j(k)$: Phase-shift of the photoelectron

Since the EXAFS equation is a theoretical approximation to the experimental data and not an exact representation, the theoretical $\chi_i^{th}(k)$ must be fitted to the experimental $\chi_i^{exp}(k)$ to ensure a good approximation. Assumptions about the chemical nature of the sample has to be made and the number of shells to fit has to be chosen. Software such as DL_EXCURV[70] can be used to refine the theoretical values via least-square approximation. The goodness of fit between the theoretical and experimental data is given by the fit factor, R:

$$R = \sum_i^N \frac{1}{\sigma_i} \left[\mid \chi_i^{exp} - \chi_i^{th} \mid \right] \times 100\% \tag{2.22}$$

A low value (below 50) of R generally indicates a good fit and a good model, however a good mathematical fit does not necessarily represent a model which is chemically valid, thus requiring the need for adjusting the model to the expected atomic structure.

2.9.3 Fourier filtering for identifying neighbouring element

As the experimental function $\chi(k)$ is a sum of all frequencies from the oscillations of the EXAFS region, EXAFS analysis is primarily done by Fourier transforming (FT) k$\chi(k)$ into r-space which is a frequency distribution spectrum. The frequencies are dependent on the distances between the absorber atom and the neighboring shells and are displayed as peaks of varying intensity where each peak represent a shell. Occasionally it can be difficult to determine the element in a neighboring shell and the element can then be identified by the use of Fourier filtering (FF), a useful tool where a shell is isolated and back-transformed from r-space to k-space. This produces a $\chi(k)$-curve for the isolated shell which can be fitted individually. Structural information obtained from the back-transformed $\chi(k)$ is then used to perform a new fitting together with all the other shells to obtain the total structural information of the sample.[69] An

illustration of the Fourier filtering process can be seen in figure 2.19.

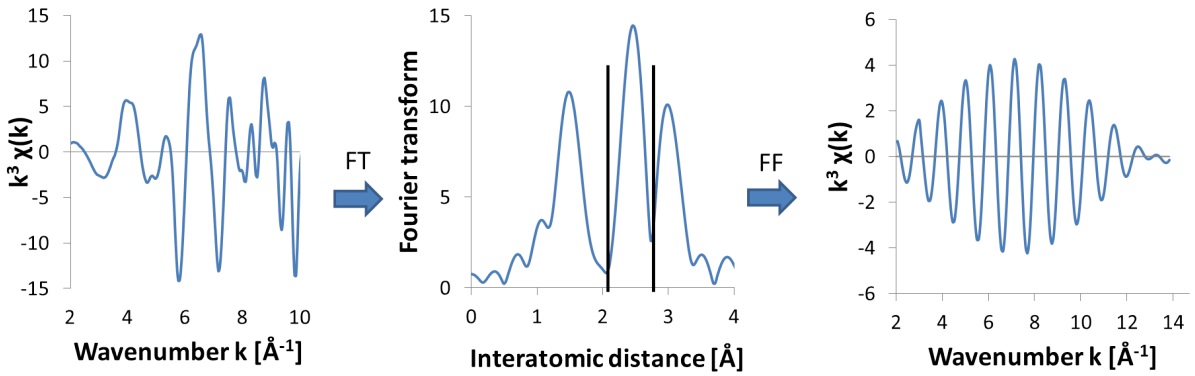

Figure 2.19: Illustration showing the Fourier filtering process of isolating a shell and back-transforming to $\chi(k)$.

In this work, several reference compounds are used to determine chemical environment of cobalt in the silica aerogel. Known interatomic distances and multiplicities for reference compounds CoO and Co_3O_4 are shown in table 2.1.

Table 2.1: Interatomic distances and coordination number of cobalt reference compunds CoO and Co_3O_4.[71]

Compound	**Shell**	**Range (Å)**	**N**
CoO	Co-O	2.0-2.5	5.2 $\pm$ 0.01
	Co-Co	3.0-3.5	11.5 $\pm$ 0.02
Co_3O_4	Co-O	1.7-2.2	5.5 $\pm$ 0.02
	Co-Co	2.3-3.0	3.5 $\pm$ 0.02

In Co_3O_4, the spinel structure is seen where cobalt cations occupy both octahedral interstices (Co^{3+}) and tetrahedral interstices (Co^{2+}), while CoO takes on the rock salt structure with Co^{2+} cations only on octahedral interstices.[72]

3 Experimental

3.1 Synthesis

Cobalt was introduced into the gel via the sol-gel method. The silica aerogels were prepared by the APD method using two different approaches; the CP-method and the SD-method. Parameter studies were performed, testing the effect of pH, Co-content, Co-precursor and concentration of silylation agent added. A modified version of the SD-method was also performed where the gels were washed to remove unreacted silylation reagent and other reaction products before drying. The chemicals used in the synthesis of silica aerogels were water-glass (Na_2SiO_3, 26.5wt.%), Amberlite IR120 H^+, hexamethyldisilazane (HMDZ), hexamethyldisiloxane (HMDSO), n-heptane, ethanol (100 %), ammonium hydroxide (NH_4OH), nitric acid (HNO_3 cobalt acetate tetrahydrate ($Co(C_2H_3O_2) \cdot 4H_2O$) and cobalt nitrate hexahydrate ($Co(NO_3)_2 \cdot 6H_2O$). All chemicals were bought from Sigma-Aldrich.

3.1.1 Preparation of sol

Preparation of the sol differed depending on the cobalt-precursor used later in the synthesis. For cobalt nitrate the procedure was as followed:

The water-glass was first diluted with distilled water to obtain a solution of 8 wt.% of silica. Ion exchange of the water-glass was then performed with Amberlite in a 1:1 volume proportion in a column. The pH changed from 13 to 2, indicating an exchange of Na^+ ions with H^+ ions and the formation of silicic acid as expected from previous work.[25] Cobalt nitrate was then added to the sol and dissolved by stirring vigorously.

Due to the low solubility and basicity of cobalt acetate, it could not be added directly to the silicic acid. The basicity of the cobalt acetate would catalyze gelation before it completely dissolved in the sol. The procedure for sol used for cobalt acetate gels had to be modified and was performed as followed:

A small amount of distilled water used for dilution of the water-glass was removed prior to

the ion exchange making a 11 wt.% solution of silica. Ion-exchange of the water-glass were performed the same way as for the cobalt nitrate sol. Cobalt acetate was then dissolved in the removed water and added to the silicic acid, diluting it corresponding to a 8 wt.% of silica before ion-exchange.

3.1.2 Water-glass based silica aerogels via the CP-method

A batch of sol with either cobalt nitrate or cobalt acetate was prepared as explained in section 3.1.1. HMDZ and HMDSO was then added while stirring vigorously. The addition of HMDZ produces ammonia (NH_3) resulting in an increase in pH to ~8. As HMDZ acts as a base catalyst, no further addition of base was needed. Gelation occurred therefore within a short time (60s-120s). A VWR pHenomenal® pH 1100L pH meter was used to record the change in pH from the addition of silylation agents to the point of gelation. The time it took until gelation occurred was also recorded. The prepared hydrogels were then immersed in n-heptane for 24 h for solvent exchange and dried. The steps involved in the CP-based synthesis are illustrated in Figure 3.1.

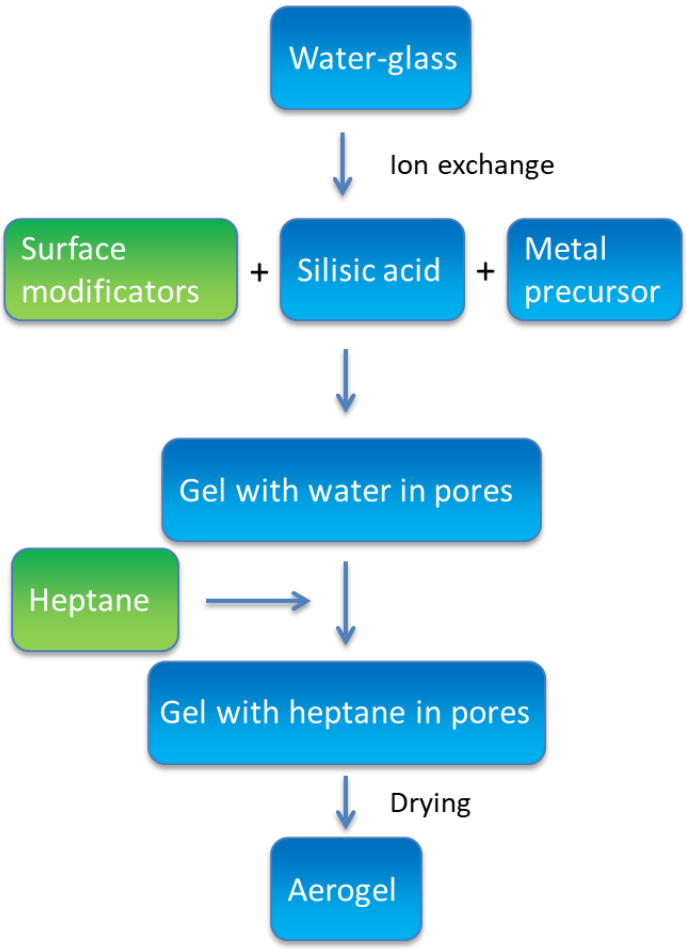

Figure 3.1: Flowchart showing the steps involved in the synthesis of the aerogels via the CP-method. Green boxes showing the point at which silylation agents and heptane is added, which is specific for the CP-method.

3.1.2.1 Cobalt content parameter study

The effect of cobalt loading in the gels was studied by preparing gels as explained in section 3.1.2, with $Co(NO_3)_2 \cdot 6H_2O$ as cobalt precursor. Eight gels were prepared with constant molar ratio of H_2O:Si = 33, HMDZ:Si = 0.70 and HMDSO:Si = 0.73 as done in previous work,[3] but with varying amount of cobalt loading from molar ratio Co:Si = 00025 to Co:Si = 0.25. An overview of the theoretical cobalt content in each sample is shown in figure 3.2. A complete overview of the parameters is shown in appendix A, table A.1.

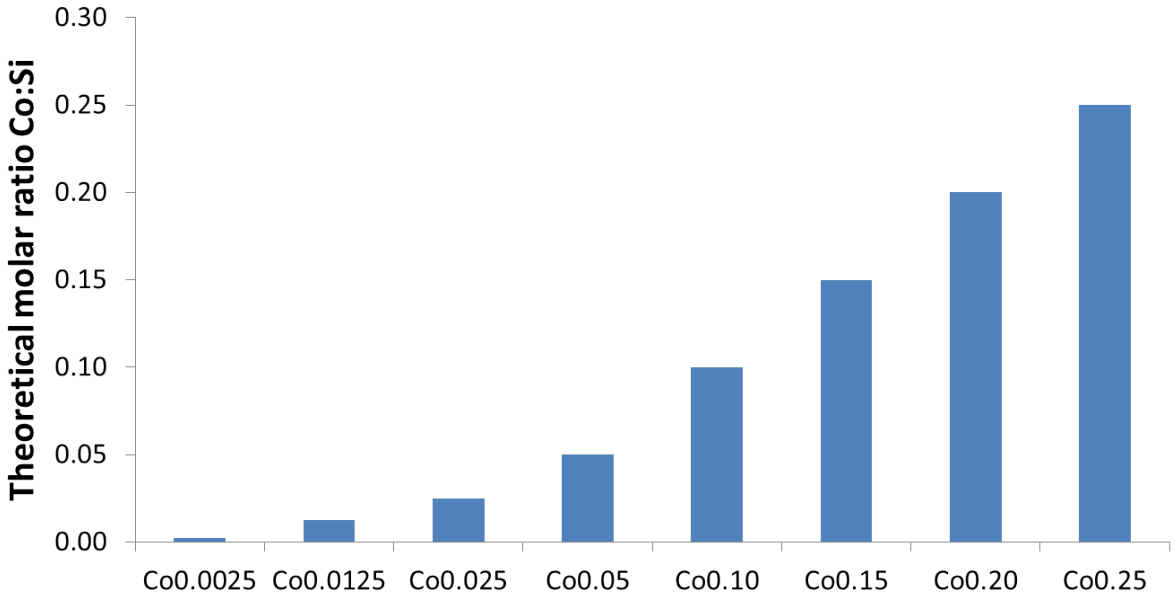

Figure 3.2: Figure showing the cobalt content for each prepared sample.

3.1.2.2 Concentration of silylation agents and cobalt precursor parameter study

The effect of concentration of silylation agents and cobalt precursor was studied by preparing gels as explained in section 3.1.2, with $Co(NO_3)_2 \cdot 6H_2O$ and $Co(C_2H_3O_2) \cdot 4H_2O$ as cobalt precursors. Two series of three gels were prepared, each with a different cobalt precursor. The precursor parameter study was combined with the concentration of silylation agent parameter study to avoid preparing unnecessary duplicate samples, and due to it being easier to control the amount of silylation agent added compared to controlling the pH. The gels within the two series were therefore prepared constant molar ratio of H_2O:Si = 33, Co:Si = 0.025 with varying concentrations of HMDSO and HMDZ ranging from a molar ratio of HMDSO:Si = 0.25 and HMDZ:Si = 0.25 to HMDSO:Si = 1.00 and HMDZ:Si = 1.00. An overview of the concentration of silylation agent in each sample is shown in figure 3.3. A complete overview of the parameters is shown in A, table A.2.

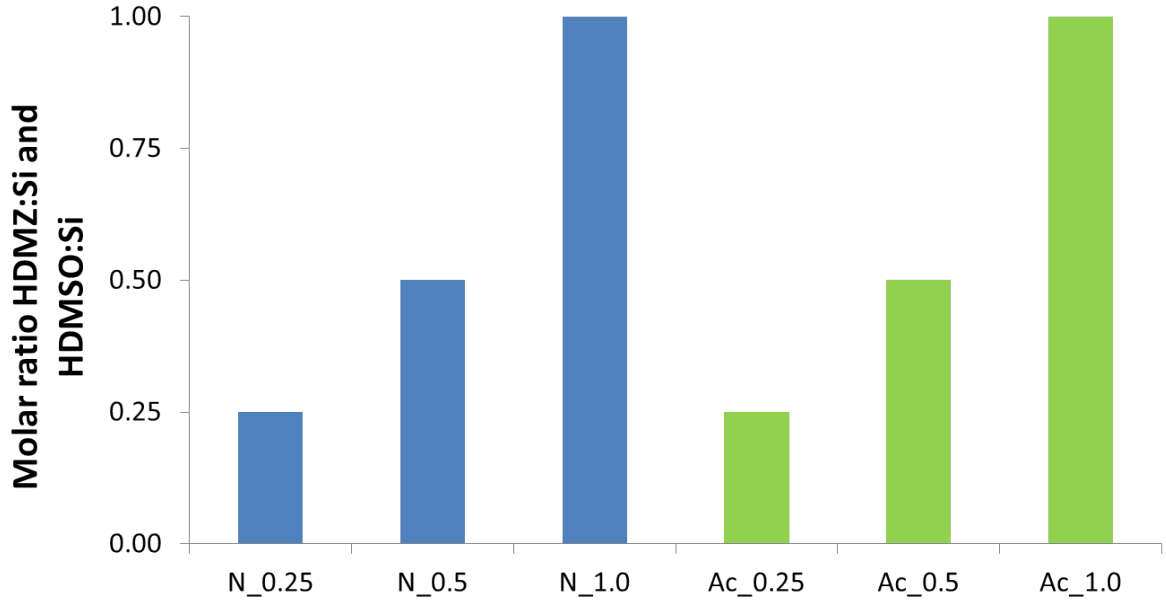

Figure 3.3: Figure showing the concentration of silylation agent for each prepared sample.

3.1.3 Water-glass based silica aerogels via the SD-method

A batch of sol with either $Co(NO_3)_2 \cdot 6H_2O$ or $Co(C_2H_3O_2) \cdot 4H_2O$ was prepared as explained in section 3.1.1. The pH of the sol was adjusted by adding a solution of NH_4OH (0.2 M) or HNO_3 (0.2 M) drop-wise while monitoring the pH with a pH meter. To avoid too much dilution of the sol while adjusting the pH, the concentration of NH_4OH or HNO_3 had to be high enough to reduce the amount of added H_2O. Time until gelation varied depending on the pH, ranging from 1 min for pH 6.9 to 4 h for pH 3.5. After gelation the hydrogels were then immersed in 35g HMDZ (molar ratio HMDZ:Si at 7) and 75 ml heptane for 24 h for surface modification and solvent exchange and dried.[3] The steps involved in the SD-based synthesis are illustrated in Figure 3.4.

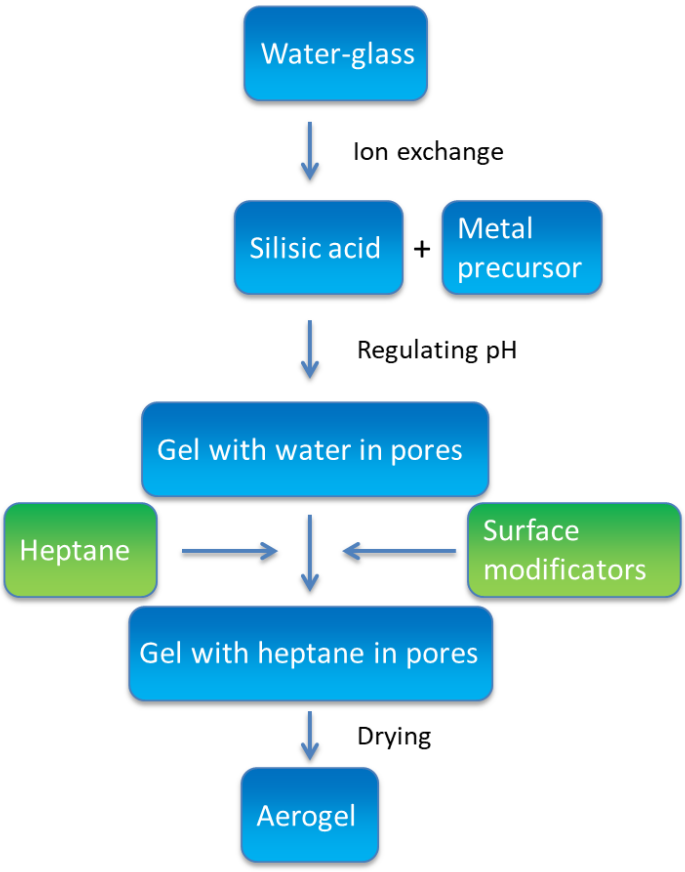

Figure 3.4: Flowchart showing the steps involved in the synthesis of the aerogels via the CP-method. Green boxes showing the point at which silylation agents and heptane is added, which is specific for the SD-method.

3.1.3.1 pH parameter study

The effect of pH was studied by preparing gels as explained in section 3.1.3 with $Co(NO_3)_2 \cdot 6H_2O$ and $Co(C_2H_3O_2) \cdot 4H_2O$ as cobalt precursors. Two series of three gels were prepared, each with constant molar ratio H_2O:Si = 33, Co:Si = 0.025 and HMDZ:Si = 7 and with different cobalt precursor. The pH was varied within the series ranging from 3.5 to 6.9. An overview of the pH in each sample is shown in figure 3.5. A complete overview of the parameters is shown in appendix A, table A.3.

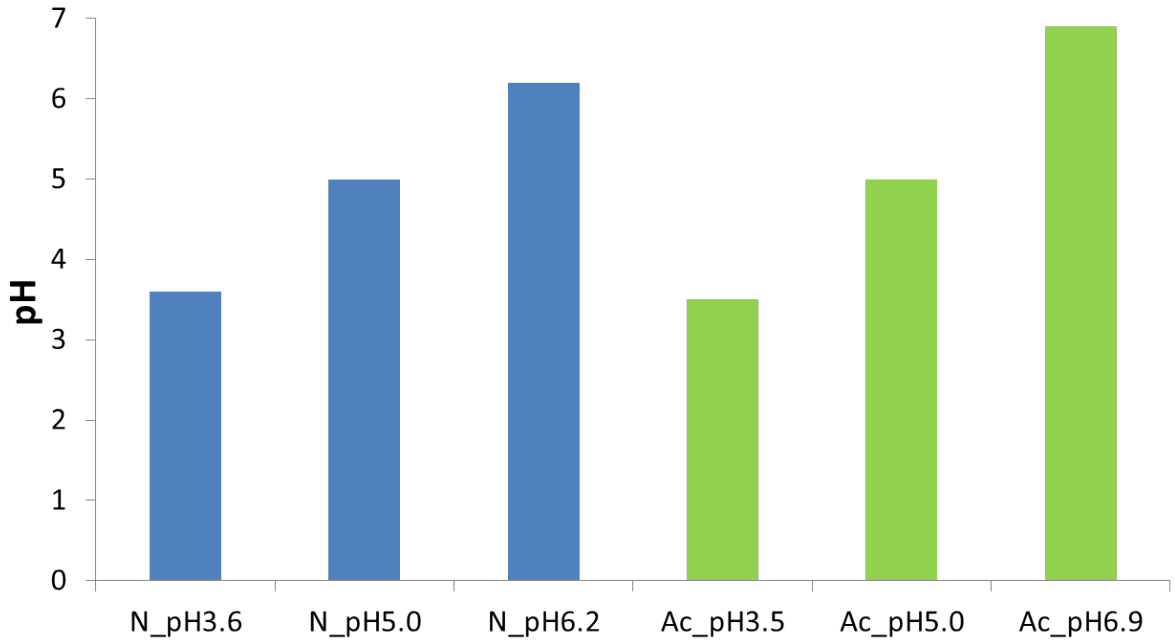

Figure 3.5: Figure showing the pH for each prepared sample.

3.1.3.2 Ethanol and heptane washed gels

To make sure all unreacted silylation reagents and other reaction products would not affect any measurements and characterizations, a washing procedure was tried for three gels prepared with the SD-method, inspired by previous work.[24,30] Three gels were prepared with the SD-method described in section 3.1.3, with $Co(NO_3)_2 \cdot 6H_2O$ as the cobalt precursor, adjusting the pH to 4.7, with constant molar ratio H_2O:Si = 33 and varying molar rato of Co:Si from 0.0025 to 0.025. Gelation occurred after 4 h. After gelation the gels were washed by immersing them in 75 ml ethanol (100 %) four times within 24 h. The gels were then washed again by immersing them in 75 ml heptane four times within 24 h. Further, the samples were immersed in a 75 ml solution of 20 vol% HMDZ and 80 vol% heptane for 24 h for surface modification. A final washing was performed by immersing the gels in 75 ml heptane four times within 24 h to remove unreacted silylation agents. Lastly the gels were dried. An overview of the cobalt content in each sample is shown in figure 3.6. A complete overview of the parameters is shown in appenidix A, table A.4.

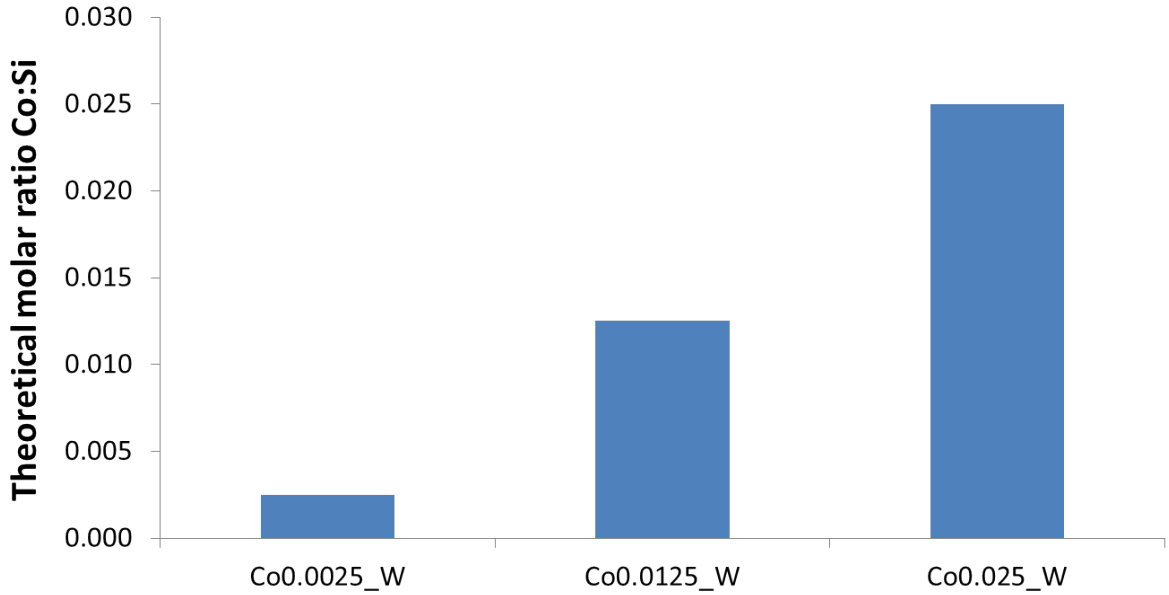

Figure 3.6: Figure showing the pH for each prepared sample.

3.1.4 Drying of gels

The drying procedure is common for all gels synthesized in this project. The wet gels were dried in air starting at room temperature (~25 °C) in a furnace with the heating program: 18 h at 65 °C, 3h at 85 °C and 2 h at 120 °C with a heating rate of 5 °C/min at all steps. After the program had finished, the gels were removed from the furnace and left to cool. The drying program can be seen in figure 3.7.

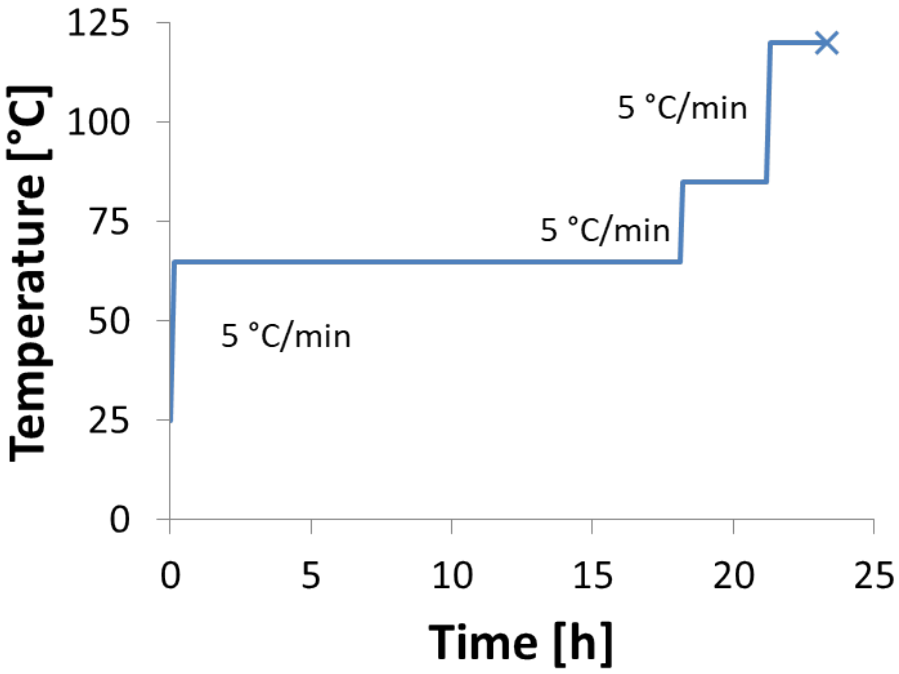

Figure 3.7: Drying program for the wet gels. X indicate the point when the samples were removed from the furnace to cool.

3.1.5 Heat treatment

All gels from the cobalt content parameter study were subject to heat treatment in air starting at room temperature (~25 °C) in a furnace, applying two different heating programs: 1) 30 min at 450 °C with a heating rate of 5 °c/min referred to as calcining and 2) 3 h at 700 °C with a heating rate of 10 °C/min referred to as annealing.[73] All samples subject to calcining have "_450" added after the sample name and all samples subject to annealing have "_700" added after the sample name. The drying programs can be seen in figure 3.8.

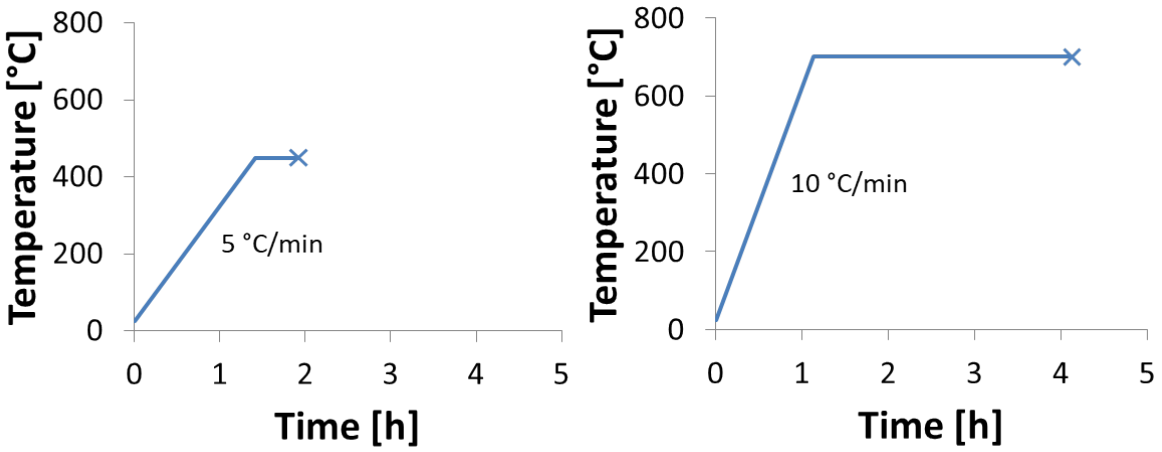

Figure 3.8: Heating program for the dry gels. X indicate the point when the samples were removed from the furnace to cool.

3.2 Powder X-ray Diffraction

X-ray powder diffraction was performed using a Burker D8 Advance DaVinci X-ray diffractometer with a CuKα radiation source with a lynxeye^{TM} superspeed 1D detector. The divergence slit opening was set to 6 mm and a step size of 0.013 °. Angles included in measurement ranged from 5° to 60°. The samples were prepared in quartz sample holders and placed in queue prior to analysis.

3.3 BET and BJH

For BET analysis, Tri Star 3000 Surface Area and Porosity Analyzer was used. Prior to measurement, samples were weighed out and degassed at 250 °C for 24 hours. The specific surface area was then calculated using the adsorption and desorption isotherms using the BET method. The pore volume and pore distribution were calculated using the BJH method.

3.4 Inductively Coupled Plasma- Mass Spectrometry

Pre-treatment of samples were carried out as followed: 10-40 mg of the samples were weighed out and transferred to Teflon vessels (25 mL) that were previously flushed with MQ-water (mili-q). The samples were then decomposed by addition of concentrated hydrofluoric acid (HF, 0.5 g) and concentrated nitric acid (HNO_3, 1.5 mL). Each decomposed sample was transferred to a large Teflon flask and diluted until a weight of 216.6 g was reached. A Teflon tube (16 mL) was then flushed with MQ-water and washed with the sample solution before it was filled with sample solution. Three blank samples were also prepared to eliminate background noise. The analyses were conducted by Syverin Lierhagen at NTNU using a High Resolution Inductively Coupled Plasma ELEMENT 2 ICP-MS.

3.5 Scanning Electron Microscopy

Scanning electron microscopy was performed on a Hitachi S-3400N. Samples were first placed on a sample holder with carbon tape and excess sample blown off. Samples were then coated with carbon using low-vacuum sputtering to make them conductive. The sample holders with the samples were loaded into the apparatus and the chamber evacuated. Images were captured at magnification 1.50k eV, 4.20k eV and 11.0k eV.

3.6 Thermogravimetric Analysis

TGA was carried out with a Perkin Elmer Thermogravimetric Analyzer (TGA7). A 7-10 mg sample was loaded in a Pt pan and heated from 50 °C to 750 °C with a heating rate of 5 °C/min with a constant airflow of 50 mL/min with 20 mL/min protective helium gas.

3.7 Catalytic testing and FT-IR Spectroscopy

Catalytic performance of ammonia decomposition was carried out in a Carbolite MTF 12/38/250 tube furnace using a 40 cm long quartz reactor tube with inner diameter of 4 mm connected to

a Gasmet^{TM} DX4000 FT-IR analyzer. First the reactor was loaded with an appropriate amount of sample (15-30 mg). The system was then flushed with He (99.9999%). Pre-treatment of sample was performed in a gas mixture of 75% H_2 and 25% Ar with a flow of 10 mL/min at temperatures ranging from room temperature to 200 °C with a heating rate of 3 °C/min. Catalytic reactions were carried out in a gas mixture of 5% NH_3 and 95% He from 200 °C to 700 °C with a heating rate of 3 °C/min. The reaction products were diluted with 100% N_2 with a flow of 340 mL/min, producing a total gas flow of 350 mL/min in to the FT-IR analyzer. A simple schematic overview of the setup is shown in figure 3.9.

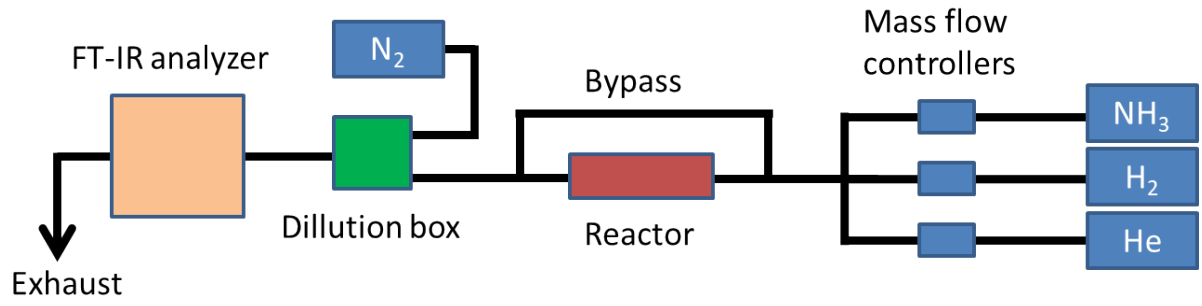

Figure 3.9: Experimental setup of the reactor and FT-IR analyzer.

Conversion of NH_3 was calculated by the following equation:

$$\%Conversion = \frac{[NH_3]_{in} - [NH_3]_{out}}{[NH_3]_{in}} \times 100\% \tag{3.1}$$

3.8 X-ray Absorption Spectroscopy

All XAS data was collected in transmission mode at the Swiss-Norwegian Beam Lines (SNBL) at the European Synchrotron Radiation Facility (ESRF) in Grenoble, France. Multibunch filling mode was also used to collect the data with a 6 GeV operating beam energy and maximum current of 200 mA. A Si(111) double crystal was used as a monochromator. The ion chamber I_0 was filled with 100% air and the ion chamber I_t was filled with a gas mixture of 60% N_2 and 40% Ar. XAS data was collected at the Co K-edge (7709) in the range 7600-8500 eV with a counting time of 200 ms and step size of 0.5 eV. Reference compounds and selected samples

were measured ex-situ by placing sample powder in aluminum sample holders and held in place with Kapton® tape.

3.8.1 In-situ measurements

In-situ measurements were performed by placing a small amount of sample (~120 mg) inside a 2 mm quartz capillary and packed with quartz wool on each side to allow for gas flow through the sample, controlled by flow controllers. Pretreatment was carried out by heating the sample from room temperature to 600 °C with a heating rate of 10 °C/min in a 10 mL/min flow of 75% H_2 and 25% Ar. The sample was held at 600 °C for 60 min before cooling to 200 °C. After cooling, the gas was switched to 5% NH_3 and 95% He with a flow of 10 mL/min for catalytic measurements of ammonia decomposition. The sample was then heated to 700 °C with a heating rate of 2.5 °C/min and was held at 700 °C for 30 min before cooling. Reaction products were constantly monitored by a mass spectrometer.

During heating, several XANES scans were collected within the range of 7.6-8.5 keV with a step size of 1 eV and counting time of 400 ms. For the pretreatment, XANES were collected starting at 100 °C and at intervals of 80 °C until reaching 600 °C. At 600 °C, XANES were collected at 8 min intervals. During decomposition of ammonia, XANES were collected starting at 200 °C and at intervals of 16 degree until reaching 700 C. At 700 °C, XANES were collected at 8 min intervals.

EXAFS scans were also collected at 700 °C in the range of 7.6-8.6 keV with a step size of 1 eV and counting time of 500 ms.

3.8.2 Data analysis

XAS data was reduced in the Athena software from the IFEFFIT package[70] where samples were energy corrected with E_0 set to 0.5 up the normalized μ(E) with a cobalt reference foil (7709 eV). XAS data from CoO, Co_3O_4, $Co(OH)_2$, $Co(NO_3)_2 \cdot 6H_2O$ were also collected for references. If several scans for one sample were collected, these were merged to improve the signal-to-noise ratio. Glitches from the monochromator and noise from the measurements were removed by

deglitching and truncating if necessary. The normalization range for XANES was set to 30-150 eV and from 150 to the end of the spectrum for EXAFS.

EXAFS data $\chi^{exp}(k)$ retrieved from Athena was imported to the DL_EXCURVE software[74] for further data extraction. The software was used to produce a theoretical model $\chi^{th}(k)$ and fitted to the experimental data $\chi^{exp}(k)$ retrieved from the Athena software. DL_EXCURVE calculates the backscattering amplitude for chosen atoms and ab inito phase-shifts as well as applying the curve wave theory. A k^3 weighting was used for all EXAFS data.

Cobalt oxide (CoO) was used as a reference for Co^{2+}. The multiplicities (N) and coordination shell distances (R) are known values (table 2.1 and were kept constant while the Fermi energy (E_F) and the Debye-Waller factor ($2\sigma^2$ were refined. The amplitude reduction factor, AFAC (S_0^2) was achieved by refining it alone, yielding a value of 1.15. The parameters $2\sigma^2$, R, N and E_F were refined for each sample with a constant AFAC-value transferred from CoO.

4 Results

4.1 Observations

During synthesis, several different observations were made depending on the parameter that was studied. Most notably was the difference in colors between the wet gels and the dried and the heat treated gels. The different appearance of the ethanol and heptane washed gels compared to all other gels was also significant. Red colored expelled pore water was observed for all gels, indicating incomplete cobalt uptake. Some of the most interesting visual observations will be regarded in this section.

4.1.1 Concentration of silylation agents and precursor parameter study

For the nitrate gels and the acetate gels, prior to addition of silylation agents, the sol had a light red color due to the dissolved cobalt nitrate or cobalt acetate. After addition of HMDZ and HMDSO, the color changed and varied from being a light blue for low concentrations of HMDZ and HMDSO to a deep, dark blue for higher concentrations as seen in figure 4.1.

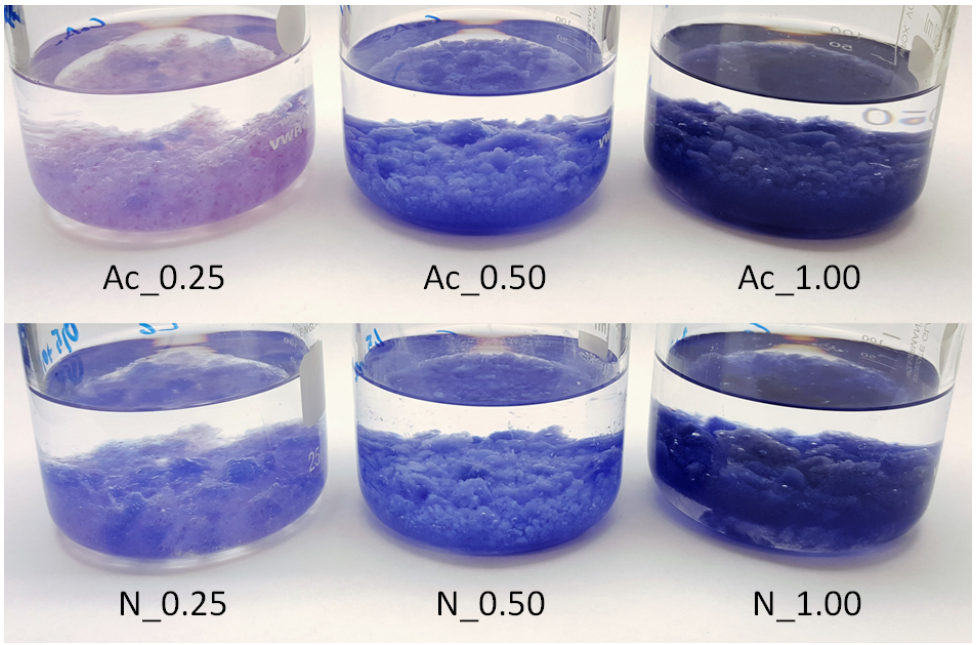

Figure 4.1: Pictures of wet gels from the concentration of silylation agent and precursor study taken after being immersed in heptane for 24 h.

The color change to blue is due to the formation of $[Co(H_2O)_4(OH)_2]$, with varying intensity depending on the concentration of HMDZ. Increased concentration of HMDZ results in an increased amount of ammonia and hydroxide ions which raises the pH, thus increasing the concentration of $[Co(H_2O)_4(OH)_2]$. The color of the sample Ac_0.25 is observed to be slightly different, indicating the presence of a $[Co(H_2O)_6]^{2+}$ complex, which exhibit a pink color. The dried gels had notable color changes depending on the cobalt precursor used and concentration of silylation agents. The dried gels are shown in figure 4.2

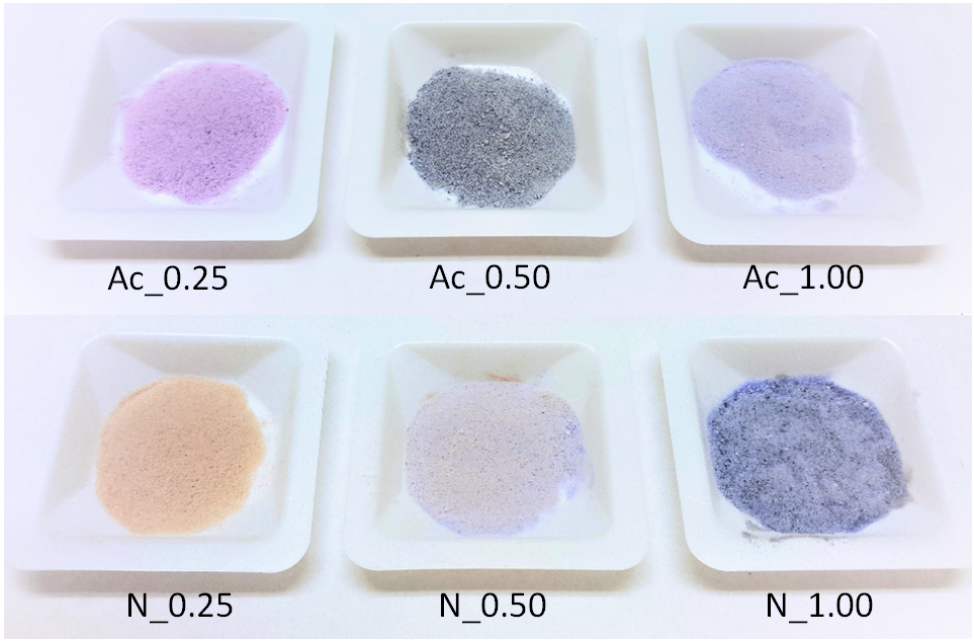

Figure 4.2: Pictures of dried gels from the concentration of silylation agent and precursor study.

The wide variety of colors in the dried gels is due to different cobalt hydroxide and cobalt amine complexes present. The yellow color seen in N_0.25 is typical for the $[Co(NH_3)_6)]^{2+}$ complex. The pink and blue colors in varying intensity is indicative of varying concentrations of $[Co(H_2O)_6]^{2+}$ and $[Co(H_2O)_4(OH)_2]$ respectively as described above.

4.1.2 Cobalt content parameter study

The wet gels in the cobalt content parameter study all had the color of the nitrate gels shown in figure 4.1, but with varying intensity depending on the cobalt loading. A weak blue was observed for the Co0.0025 sample, increasing in intensity through the samples up to Co0.25 which had a deep dark blue color, indicating the presence of $[Co(H_2O)_4(OH)_2]$. The dried as prepared gels as well as the calcined at 450 °C and annealed at 700 °C are shown in figure 4.3.

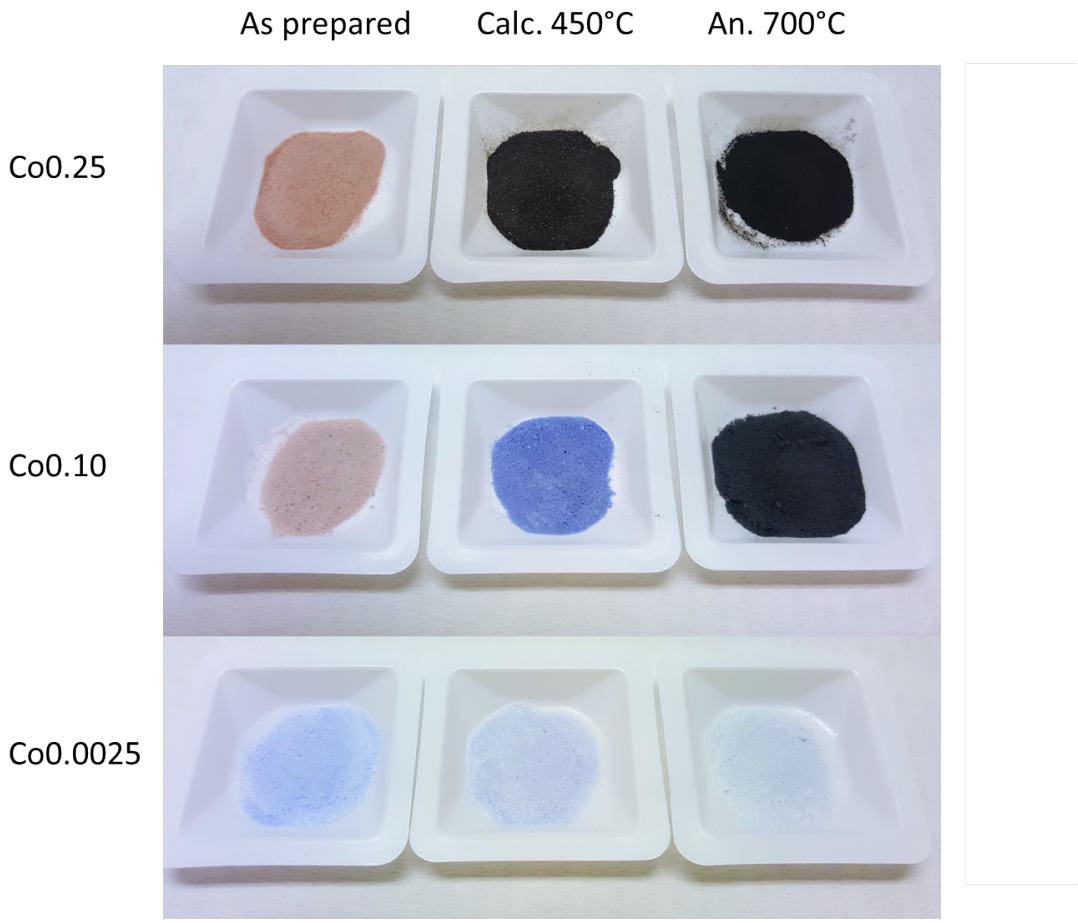

Figure 4.3: Pictures of dried gels from the cobalt content study.

For the gel with low cobalt content (Co0.0025), the as prepared gel appear light blue, but after being subjected to heat treatment, the color fades. The color of the gel with medium cobalt content (Co0.10) start out as a light brown, indicative of $[Co(NH_3)_6)^{3+}$ due to oxidation of $[Co(NH_3)_6)^{2+}$ in air. The calcined sample show a color change to blue, characteristic of $[Co(H_2O)_4(OH)_2]$ while the annealed sample is completely black due to the formation of CoO_x. The change in color observed for the as prepared sample with high cobalt loading (Co0.25), goes from a brown and directly to black in the calcined sample and the annealed sample, skipping the blue color observed in the calcined Co0.10 sample.

4.1.3 Ethanol and heptane washed gels

The most notably difference between the washed gels and the unwashed gels prepared from all the other parameter studies was the reduced shrinkage seen for the washed gels. Straight

from the drying furnace, unwashed gels had a glassy and fairly hard, sand-like texture with no translucency. They were, however, easily ground to a fine, dense powder. The dry gels also appeared to have shrunk significantly compared to the wet gels, indicating incomplete silylation of the surface. The washed gels had a rubbery, chalk-like texture with some degree of translucency and did not appeared to have shrunk as much as the unwashed gels, indicating a higher degree of silylation of the surface. Grinding the washed gels was difficult due to the rubbery texture and produced an extremely light and "fluffy" powder. The difference between a washed and unwashed gel straight from the drying furnace with samples having the same weight can be seen in figure 4.4.

Figure 4.4: Picture of dried gels straight from the drying furnace with samples containing the same weight. Unwashed gel to the left (Co0.0125) and washed gel to the right (Co0.0125_W).

4.2 Gelation time

The pH at which gelation occurred and time until gelation was recorded for all gels from the concentration of silylation agent and precursor parameter study seen in figure 3.3. The pH as a function of time is illustrated in figure 4.5

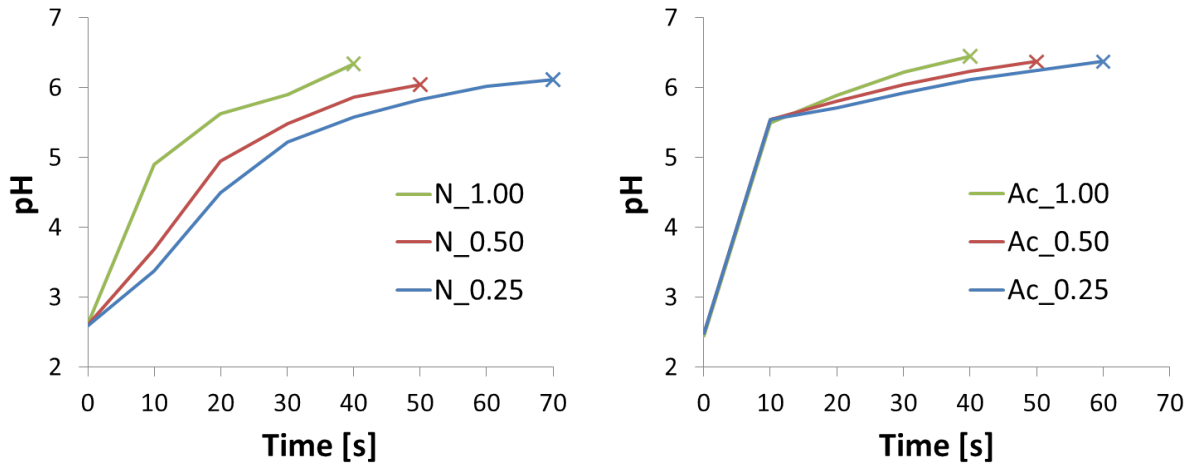

Figure 4.5: Illustration showing pH as a function of time for gels with varying concentration of silylation agent. Nitrate gels to the left and acetate gels to the right. X marks point of gelation.

The abrupt increase in pH seen in the acetate gels is attributed to the addition of basic cobalt acetate to the sol together with HMDZ and HMDSO as explained in section 3.1.1. Time until gelation is seen to decrease with increased concentration of silylation agents for both nitrate and acetate gels. Each nitrate sample and its corresponding acetate sample gels after the same amount of time with 10 s increments between the samples, with the exception of N_0.25 taking an additional 10 s until gelation. This decrease in time can be explained by an increased formation of ammonia at higher concentrations of HMDZ, catalyzing the gelation faster. The gelation takes place at pH 6-6.5 for both nitrate and acetate gels, with the latter gelling at slightly higher pH, likely due to the higher basicity resulting form addition of cobalt acetate.

4.3 Powder X-ray Diffraction

XRD was performed to exclude any unwanted crystalline phases that may be present in the amorphous aerogels. Any crystalline phases that might show could be due to impurities and reaction products stemming from the synthesis precursors. The results from the XRD will be regarded in this section.

4.3.1 Cobalt content parameter study

XRD was carried out on all samples shown in figure 3.2. The same samples calcined at 450 °C and annealed at 700 °C were also analyzed for crystalline phases. An overview showing if crystalline phases are present in the gels is shown in table 4.1.

Table 4.1: Table showing if crystalline phases are present in the samples as prepared, calcined at 450 °C and annealed at 700 °C, with orange indicating low degree of crystalline phases present and red indicating high degree of crystalline phases present.

Sample	As prepared	Calcined 450 °C	Annealed 700 °C
Co0.0025	No	No	No
Co0.0125	No	No	No
Co0.025	No	No	Yes
Co0.05	No	No	Yes
Co0.10	No	No	Yes
Co0.15	Yes	No	Yes
Co0.20	Yes	Yes	Yes
Co0.25	Yes	Yes	Yes

A selection of diffractograms from three gels with low (Co0.0025), medium (Co0.10) and high (Co0.25) Co-content highlighted (blue) in table 4.1 is presented below. XRD diffractograms for the remaining gels are presented in appendix B. XRD diffractograms of Co0.0025 as prepared, calcined at 450 °C and annealed at 700 °C are shown in figure 4.6.

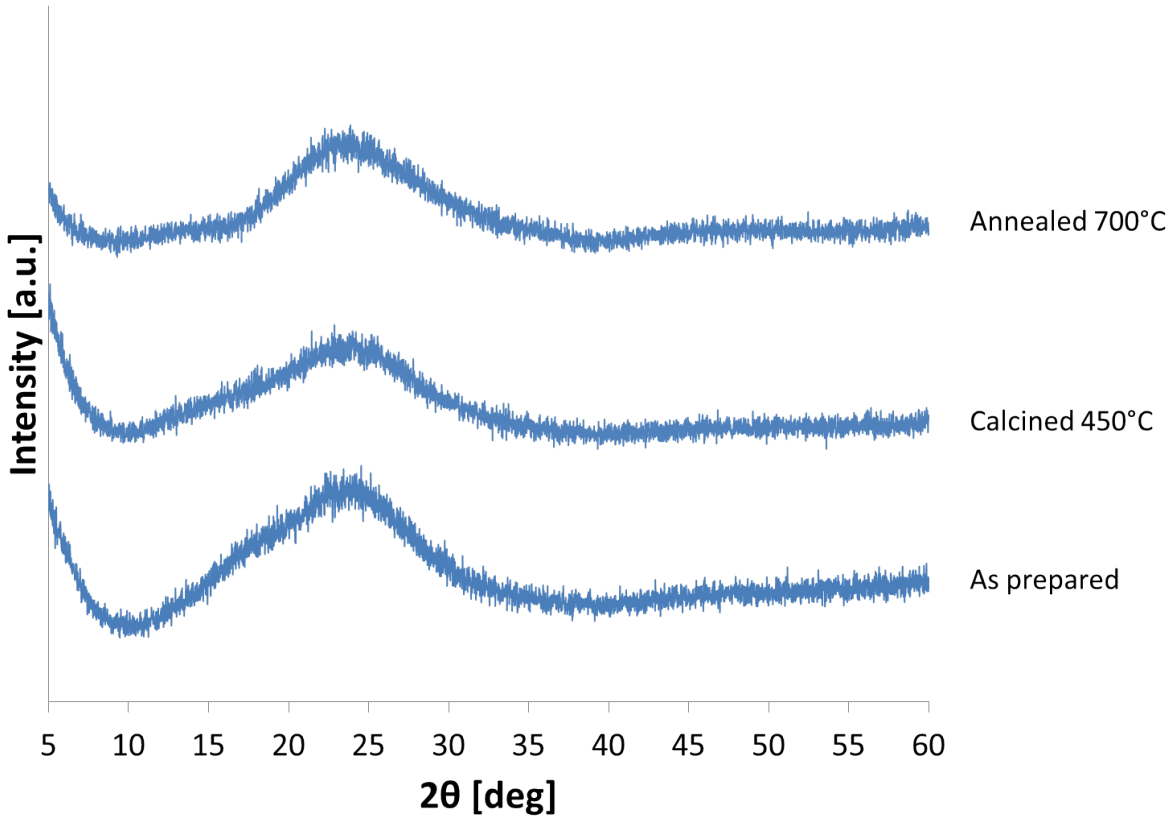

Figure 4.6: X-Ray Diffraction patterns of Co0.0025 as prepared, calcined at 450 °C and annealed at 700 °C.

The diffractograms presented in figure 4.6 show no indication of any crystalline phases present in the gels. However, the detection limit of particles >2nm must be taken into consideration as crystalline phases may still be present though not detectable. XRD diffractograms of Co0.10 are shown in figure 4.7.

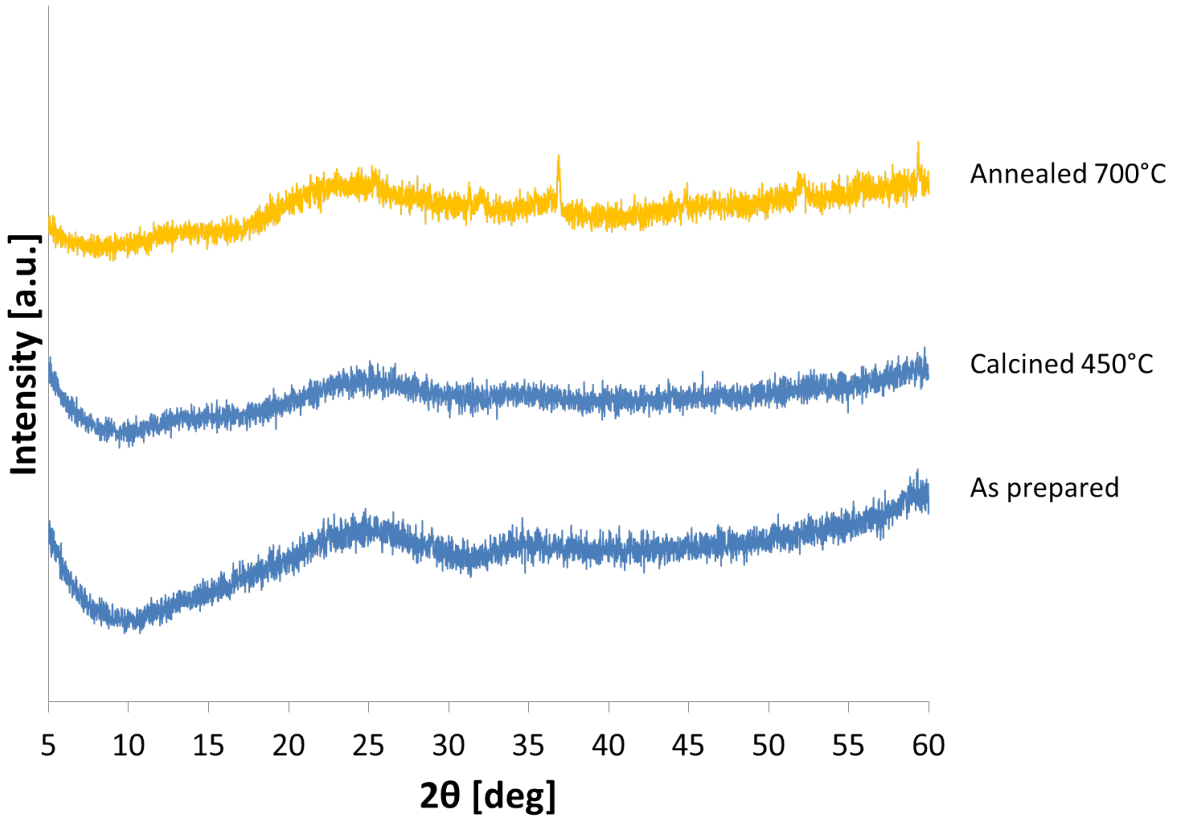

Figure 4.7: X-Ray Diffraction patterns of Co0.10 as prepared, calcined at 450 °C and annealed at 700 °C. Yellow colored line indicates low presence of crystalline phases.

XRD diffractograms for Co0.10 show some presence of crystalline phases in the sample annealed at 700 °C. The peaks correspond to a mixture of cobalt oxides (CoO_x) and cobalt silicate (Co_2SiO_4). XRD diffractograms of Co0.25 are shown in figure 4.8.

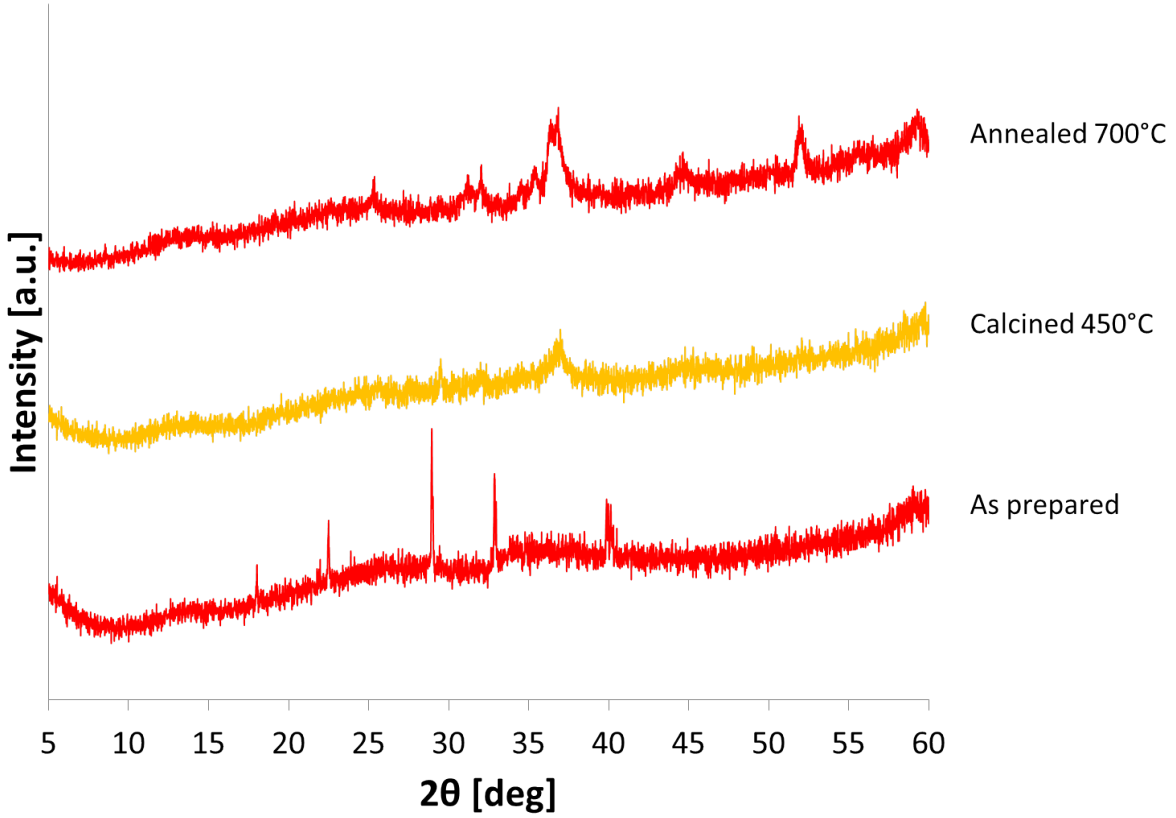

Figure 4.8: X-Ray Diffraction patterns of Co0.25 as prepared, calcined at 450 °C and annealed at 700 °C. Yellow line indicates low presence of crystalline phases and red line indicates high presence of crystalline phases.

As figure 4.8 show, a crystalline phase is present in the as prepared sample corresponding to that of ammonium nitrate. This is most likely formed as a byproduct from cobalt nitrate and the ammonia formed during the silylation with HMDZ. For the calcined sample, the ammonium nitrate phases seen in the as prepared sample disappear, but show the presence of some crystalline phases similar to that of Co0.10 annealed at 700 °C. These peaks get even more prominent in the annealed sample indicating a higher concentration of cobalt oxides (CoO_x) and cobalt silicate (Co_2SiO_4).

Comparing the diffractograms in figure 4.6, figure 4.7 and figure 4.8 the shape of the diffractograms differ quite a lot depending on the Co-content. At higher Co-content the diffractograms are flattened and increase in intensity with increasing 2θ, losing the characteristic shape of pure silica as seen in figure 2.12. This can be explained by an increase in background noise due to fluorescence from cobalt increasing at higher Co-content.

4.3.2 Collection of other parameter studies

XRD was also performed on all as prepared gels from the other parameter studies shown in figure 3.3, figure 3.5 and figure 3.6. The gels were however, very similar in regards to presence of crystalline phases and these results will regarded together in this section. The diffractograms are shown in appendix B. None of the gels from any of the parameter studies show presence of crystalline phases. These results are comparable to the as prepared gels from the Co-content parameter study with similar Co-content, which also showed no indication of crystalline phases at these cobalt concentrations.

4.4 BET and BJH

BET analysis was performed to determine the specific surface area of the synthesized gels. BJH analysis was also performed to determine the pore distribution and average pore width of the gels. The results from the BET and BJH measurements will be regarded in this section.

4.4.1 Cobalt content parameter study

BET and BJH measurements were performed on all eight gels presented in figure 3.2 as well as the same gels calcined at 450 °C and annealed at 700 °C. The adsorption and desorption isotherms and pore distribution of a selection of three gels and their calcined and annealed analogues with low (Co0.0025), medium (Co0.025) and high (Co0.25) cobalt content are shown in figure 4.9. The isotherms and pore distribution for the remaining gels together with the average pore width are shown in appendix C, figure C.13, C.14, C.15, C.16 and C.17.

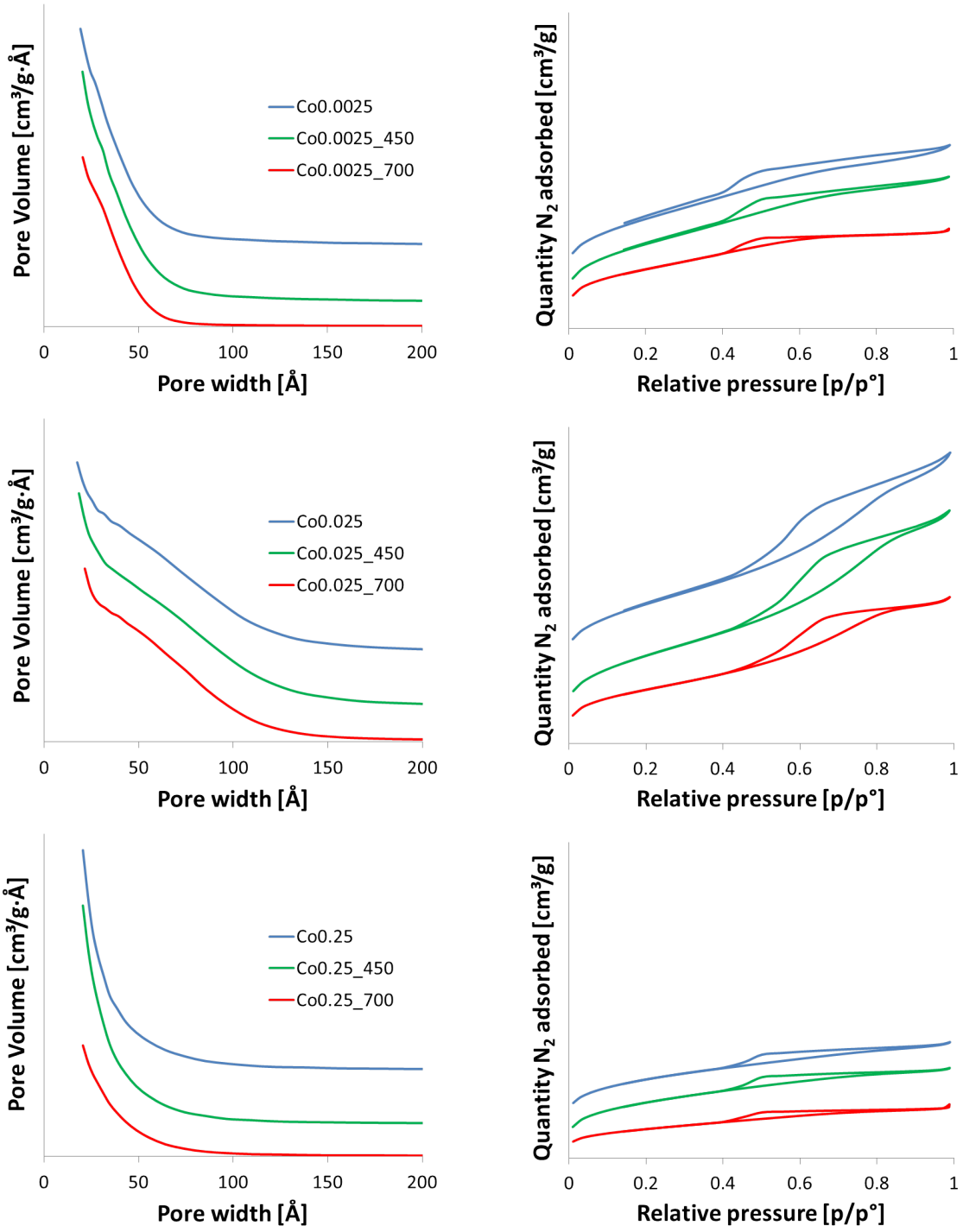

Figure 4.9: Pore distribution and adsorption and desorption isotherms for Co0.0025, Co0.025 and Co0.25 and their calcined and annealed analogues.

The pore distribution for all gels presented in figure 4.9 show that the pores consists of mainly micropores and small mesopores. However, at increasing cobalt content there is a slight shift towards larger pores, but at high cobalt content, the shift is moved back towards a more mi-

croporous nature. The change in pore distribution in regards to heat treatment show no significant change between the as prepared gels and the calcined gels, only a slight shift towards more micropores for the annealed gels. This can be explained by sintering effects and a collapse of the pore structure during the annealing.

This microporous nature of the gels is also reflected in the adsorption and desorption isotherms. The isotherms for samples Co0.0025 and Co0.25 and their calcined and annealed analogues show a type I isotherm which indicates the presence of micropores with a hysteresis loop indicating the presence of some mesopores. For Co0.025 and its calcined and annealed analogues, the isotherm takes on more of a type IV isotherm shape, indicating the presence of larger mesopores, however, the amount of mesopores is low as the average pore size is 49Å as seen in appendix C, figure C.9. An overall trend seems to be a shift towards larger pores as the cobalt content increases, reaching a maximum in the Co0.025 sample at 49Å and then decreasing at even higher cobalt content. The surface area of the as prepared gels together with their calcined and annealed analogues are shown in figure 4.9.

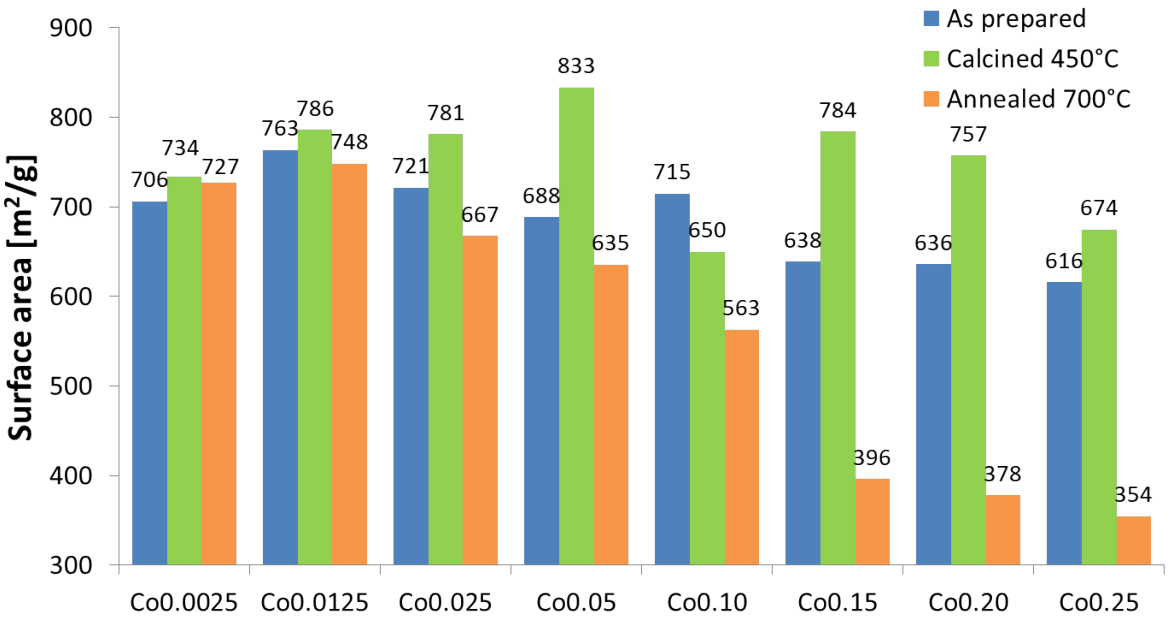

Figure 4.10: BET surface area of gels from the Co-content parameter study.

From figure 4.10 a trend can be seen where the surface area is changing in regards to the cobalt loading. For the as prepared gels, there is a slight increase in surface area before it starts to decrease as cobalt loading increases. The calcined gels also exhibit this increase in surface area,

but the decrease is starting at a higher cobalt loading than for the as prepared gels. Surface area of the annealed gels reaches a maximum at the same point as for the as prepared gels, but the decrease is much more rapid and severe as cobalt loading increases. An increase in surface area after calcining and then a decrease after annealing can be seen for all gels, except for Co0.10 sample where the surface area values do not seem to align with the overall trend. The results show that the samples have high surface areas >500 m^2/g, with the exception of the annealed Co0.15, Co0.20 and Co0.25 which all have a surface area <500 m^2/g, placing them in the low end spectrum of what is considered an aerogel.

4.4.2 Concentration of silylation agents and precursor parameter study

BET and BJH measurements were performed on all six gels gels presented in figure 3.3. The adsorption and desorption isotherms and pore distribution of the gels are shown in figure 4.11. Average pore width is shown in appendix C.

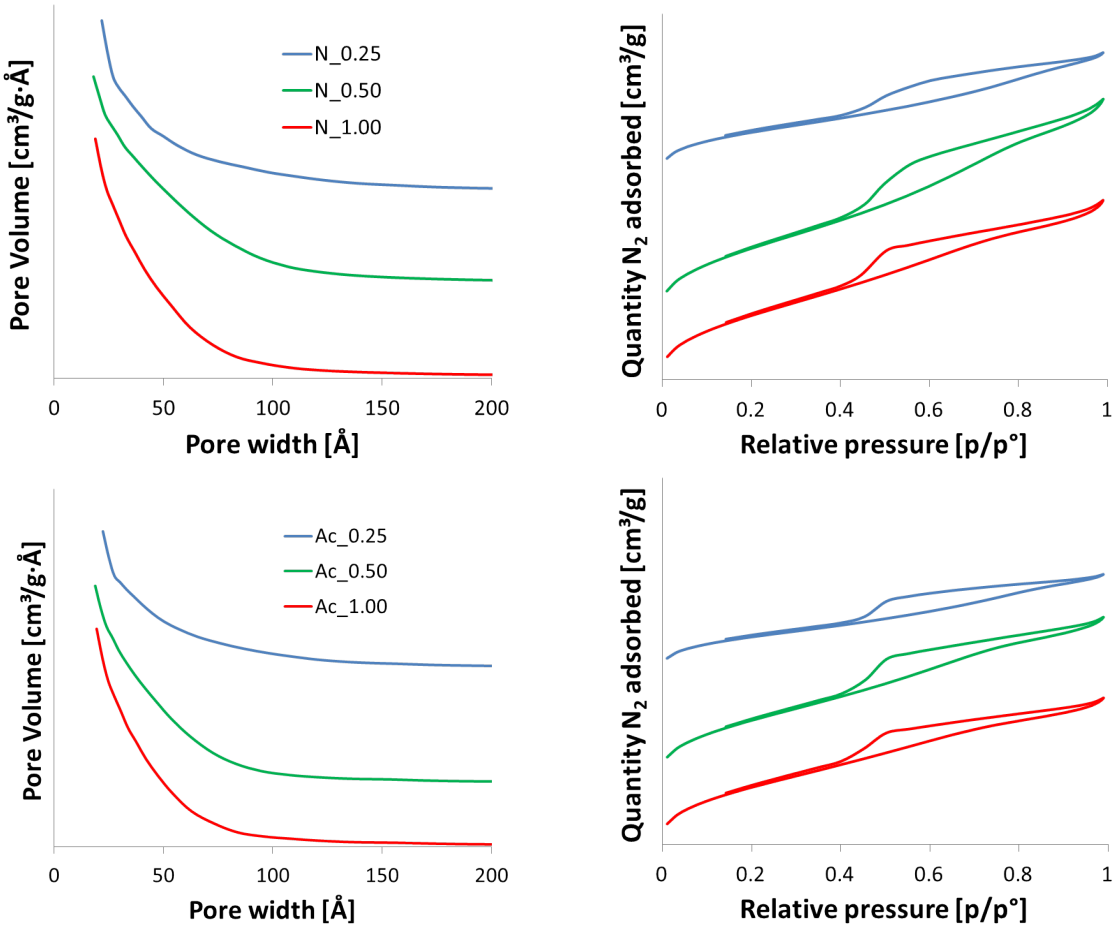

Figure 4.11: Pore distribution and adsorption and desorption isotherms for the nitrate gels (top) and the acetate gels (bottom)

The porosity for the nitrate gels and the acetate gels seems to be affected similarly with increasing concentration of silylation agent. Highest porosity is observed for the gels prepared with 0.5 molar ratio HMDZ:Si and HMDSO:Si, however, the difference in pore distribution is rather low. The isotherms takes on mostly the shape of a type I isotherm, indicative of micropores, with the hysteresis loop indicating some mesopores. This is also supported by the average pore size of the gels as seen in appendix C, figure C.10 being below 50 Å. The surface area of the the gels are shown in figure 4.12.

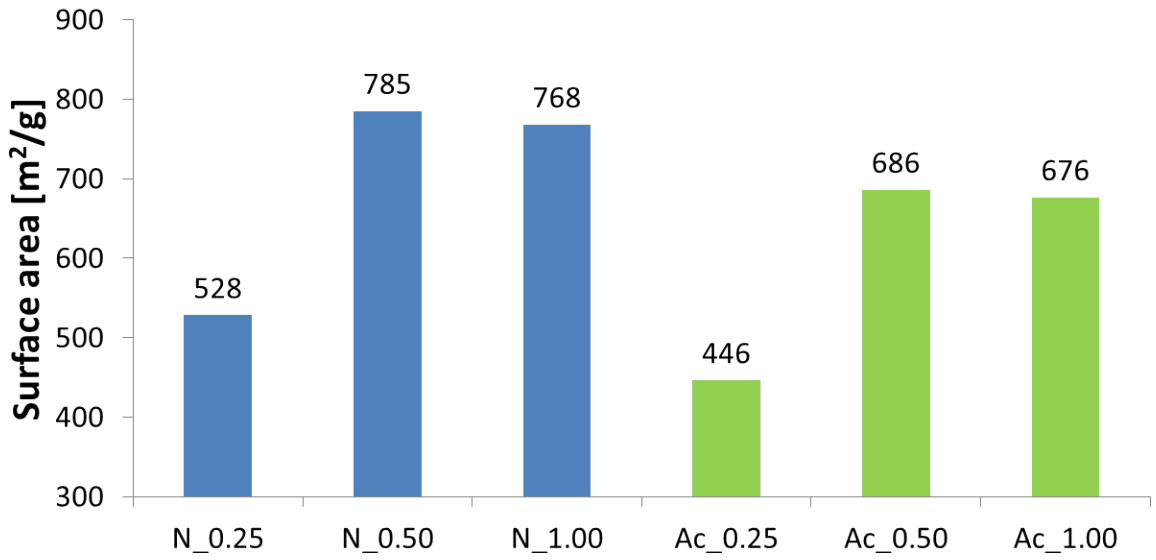

Figure 4.12: BET surface area for the gels from the concentration of silylation agents and precursor parameter study. Gels with cobalt nitrate as precursor to the left and gels with cobalt acetate as precursor to the right.

The surface area of both the nitrate gels and the acetate gels follow the same trend in surface area as for pore size distribution, with the gels prepared with 0.5 molar ratio HMDZ:Si and HMDSO:Si producing the highest, 1.00 molar ratio second highest and 0.25 the lowest. Between the two precursors, nitrate gels exhibits overall higher surface area.

The low porosity and surface area for the gels prepared from 0.25 molar ratio HMDZ:Si and HMDSO:Si can be explained by incomplete silylation of the surface, causing the gels to shrink due to capillary forces and experience cross-linking during the drying process. The higher porosity and surface area seen in the gels prepared from 0.50 molar ratio HMDZ:Si and HMDSO:Si is likely due to a more complete surface modification, hindering further condensation. At the highest molar ratio of HMDZ:Si and HMDSO:Si, a small reduction in porosity and surface area is seen and could be attributed to the increased solubility of silica due to the higher pH as a result of a higher concentration of ammonia formed from the reaction of HMDZ with surface silanols. This mechanism is also able to explain the overall lower porosity and surface area of the acetate gels compared to the nitrate gels, where the basicity of the acetate gives a higher pH, dissolving the gels more rapidly. However, the differences are very small, and the the BET and BJH measurements do have their weaknesses.

4.4.3 pH parameter study

BET and BJH measurements were performed on all gels presented in figure 3.5. The adsorption and desorption isotherms and pore distribution of the gels are shown in figure 4.13. Average pore width is shown in appendix C.

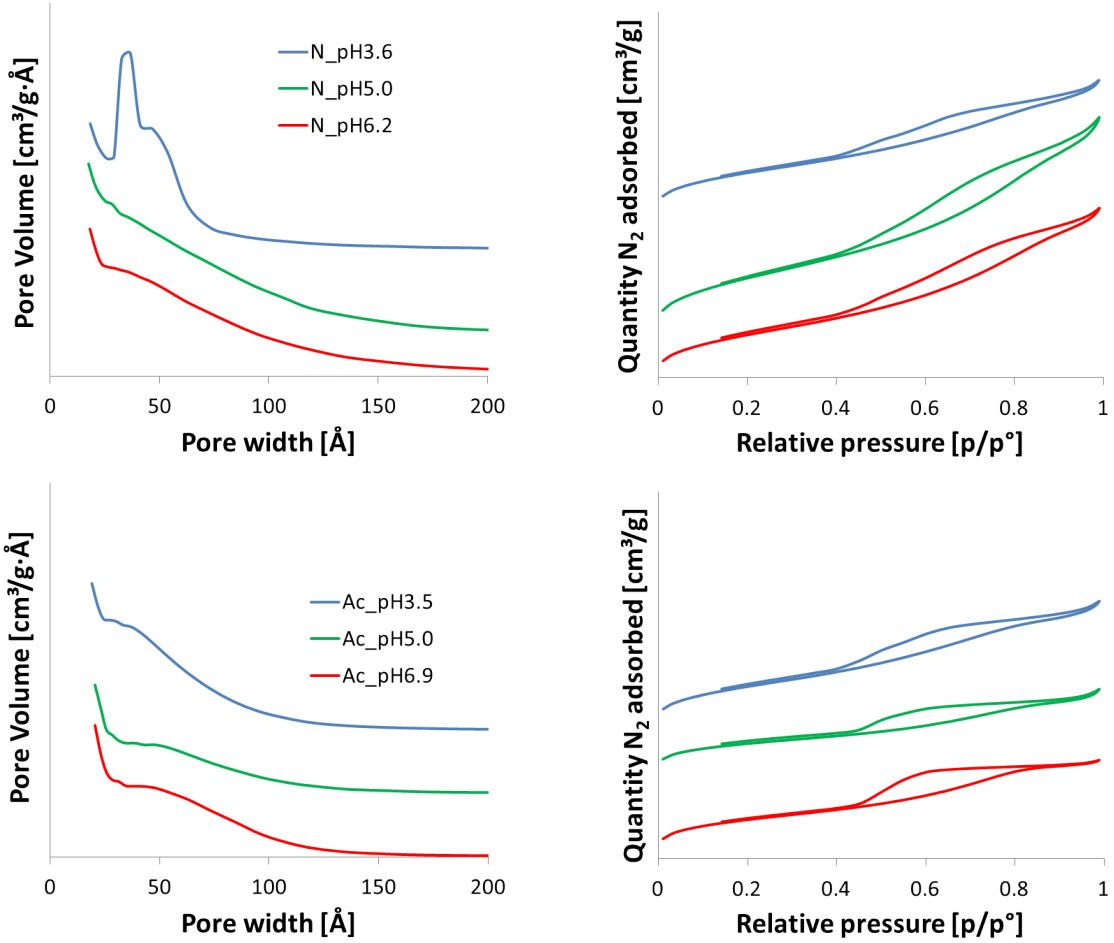

Figure 4.13: Pore distribution and adsorption and desorption isotherms for the nitrate gels (top) and the acetate gels (bottom)

The pore distribution of the nitrate gel N_pH3.6 clearly stand out, showing a jump around 25-50 Å which is not seen in the other samples, but it also does not contain any significant amount of pores wider than 75 Å which the other two gels do. The average pore width for the three gels show the lowest value for N_pH3.6 at 50 Å as seen in figure C.11, regardless of the peak observed, and the highest value for N_pH5.0 and N_pH6.2 at 55 Å. The isotherms for the three gels take on the shape of a type I isotherm, indicative of micropores with N_pH3.6

containing the most, but also mesopores as all gels exhibit a hysteresis loop. The acetate gels show the inverse of the nitrate gels, with the gel prepared at pH 3.5 having a lower amount of micropores and an average pore size of 47 Å, with the gel prepared at pH 5.0 having the largest average pore size at 52 Å. The isotherms all take on the shape of a type I isotherm, indicative of micopores with a hysteresis loop confirming the presence of mesopores. The surface area of the the gels are shown in figure 4.14.

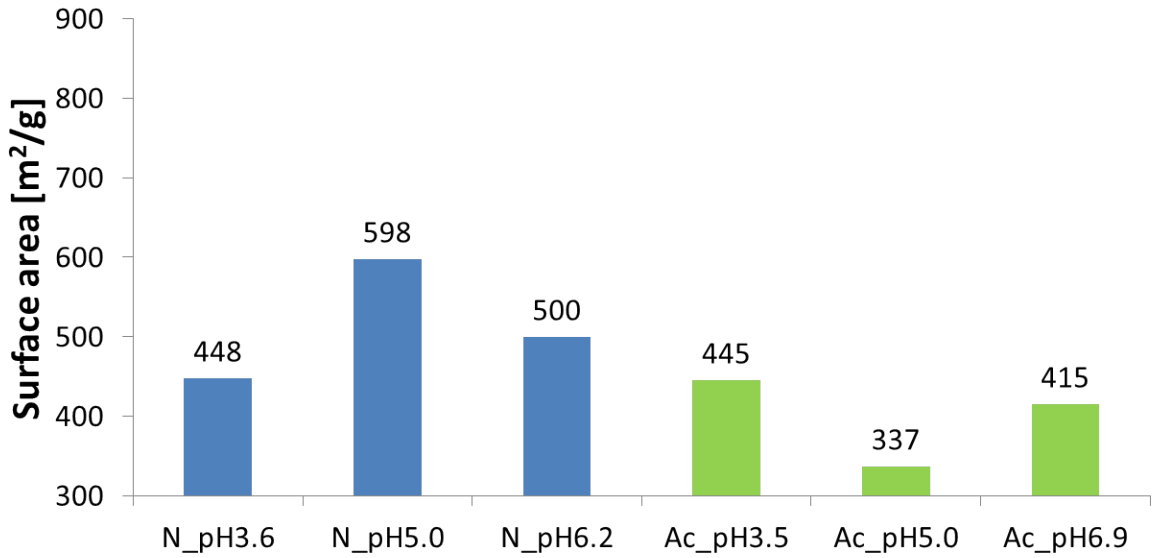

Figure 4.14: BET surface area for the gels from the pH parameter study. Gels with cobalt nitrate as precursor to the left and gels with cobalt acetate as precursor to the right.

The inverse seen in the porosity is also seen in regards to surface area, with the nitrate gels reaching a maximum at pH 5 where the acetate has a minimum. The nitrate gels also exhibits an overall higher surface area compared to the acetate gels.

4.4.4 Ethanol and heptane washed gels

BET and BJH measurements were performed on all gels presented in figure 3.6. The adsorption and desorption isotherms and pore distribution of the gels are shown in figure 4.15. Average pore width is shown in appendix C

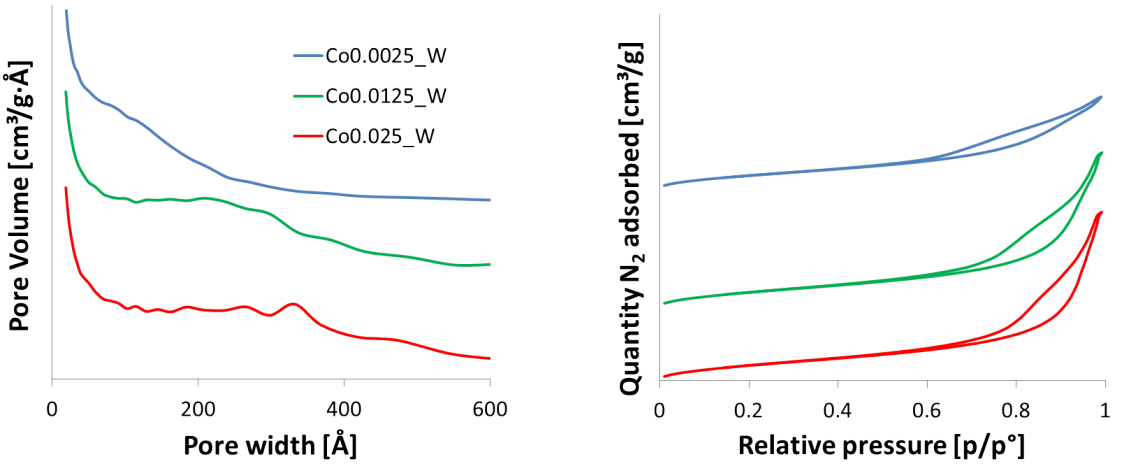

Figure 4.15: Pore distribution and adsorption and desorption isotherms for the ethanol and heptane washed gels.

For the washed gels, the pore distribution show a shift towards larger mesopores with increasing cobalt content as seen for the gels in the cobalt content parameter study with similar theoretical cobalt content. However, instead of a gradually decreasing amount of pores with high pore width, the samples Co0.025_W and Co0.0125_W show an equal distribution of pore sizes up to 230 Å for Co0.025_W and 330 Å for Co0.0125_W. Co0.0025_W show similar behaviour as its unwashed analogue. The average pore width seen appenidix C, figure C.12, is well within the mesoporous range. A type IV isotherm is observed for the Co0.025 and Co0.0125 samples, while the Co0.0025 sample show a slight shift towards a more type I isotherm. However, all three samples appear mainly mesoporous. The surface area of the gels are shown in figure 4.16.

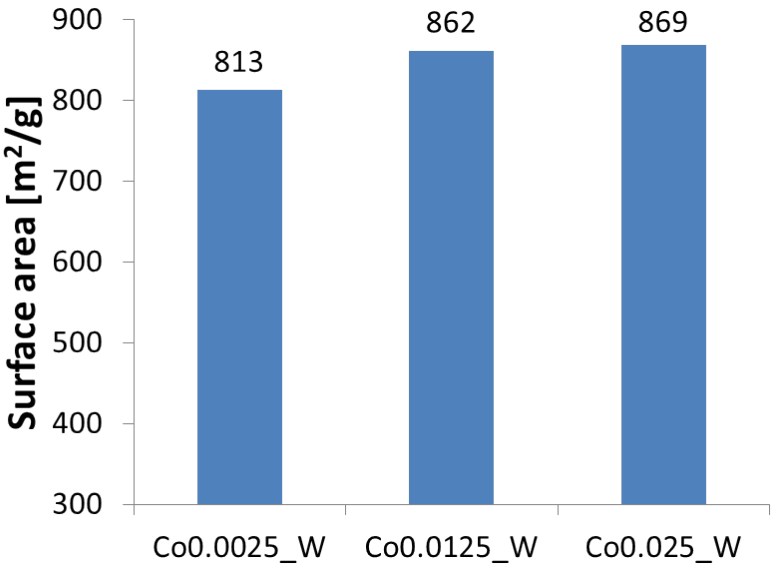

Figure 4.16: BET surface area of gels from the Co-content parameter study.

A very high surface area is observed for all the three gels, increasing with cobalt content. The extremely high porosity and high surface area seen in the gels is likely due to the repeated washing removing all pore water, reducing the capillary stresses exerted on the gels during drying. The soaking of the gels in HMDZ/heptane also increases the possibility of a reaction between HMDZ and surface silanol groups and produces a highly silylated surface unable to further cross-link by condensation.

4.5 Inductively Coupled Plasma- Mass Spectrometry

ICP-MS analysis was performed to determine the cobalt uptake of the silica aerogels under the different parameter studies. The results from the ICP-MS analysis will be regarded here.

When calculating the theoretical molar ratio, it is difficult to know the exact composition of the dry gel due to loss of Si during ion exchange, and the uncertainty in the degree of silylation. For some of the gels, the experimental molar ratio Co:Si is therefore seen to be higher than the theoretical molar ratio of Co:Si.

4.5.1 Cobalt content parameter study

ICP-MS analysis was performed on all as prepared, calcined at 450 °C and annealed at 700 °C gels from the cobalt content parameter study seen in figure 3.2. The cobalt uptake in wt.% for the as prepared gels is shown in figure 4.17. The ICP-MS data for the calcined and annealed gels is shown in appendix D, table D.6 and table D.7.

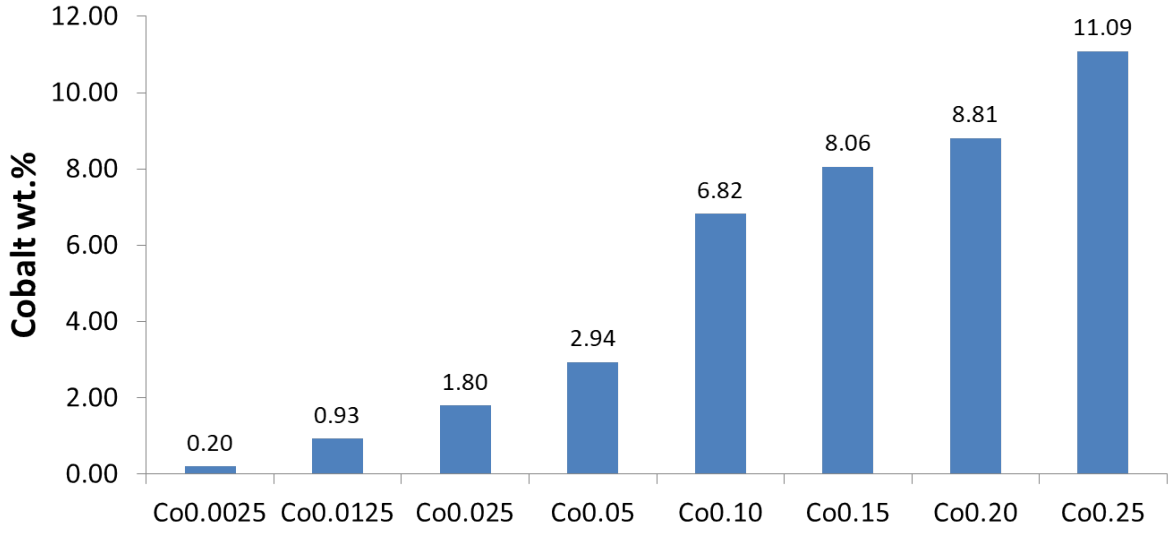

Figure 4.17: Calculated wt.% from ICP-MS for the cobalt content parameter study.

As seen from figure 4.17, the uptake of cobalt is split into two regions from molar ratio Co:Si = 0.0025 to Co:Si = 0.05 and from Co:Si = 0.10 to Co:Si = 0.25. Within the two regions, the uptake is seen to be relatively linear and overall, no upper limit of cobalt uptake is encountered. Although ICP-MS is a powerful quantitative analysis method, the uptake data does not give any information on how cobalt is present in the silica matrix or if it is in single-site position. The trend is however, with increased addition of cobalt to the sol, an increased cobalt loading is seen in the dry gel.

4.5.2 Concentration of silylation agents and precursor parameter study

For the gels from the concentration of silylation agents and precursor parameter study, all gels seen in figure 3.3 were subject to ICP-MS analysis. The cobalt uptake in wt.% is shown in figure 4.18.

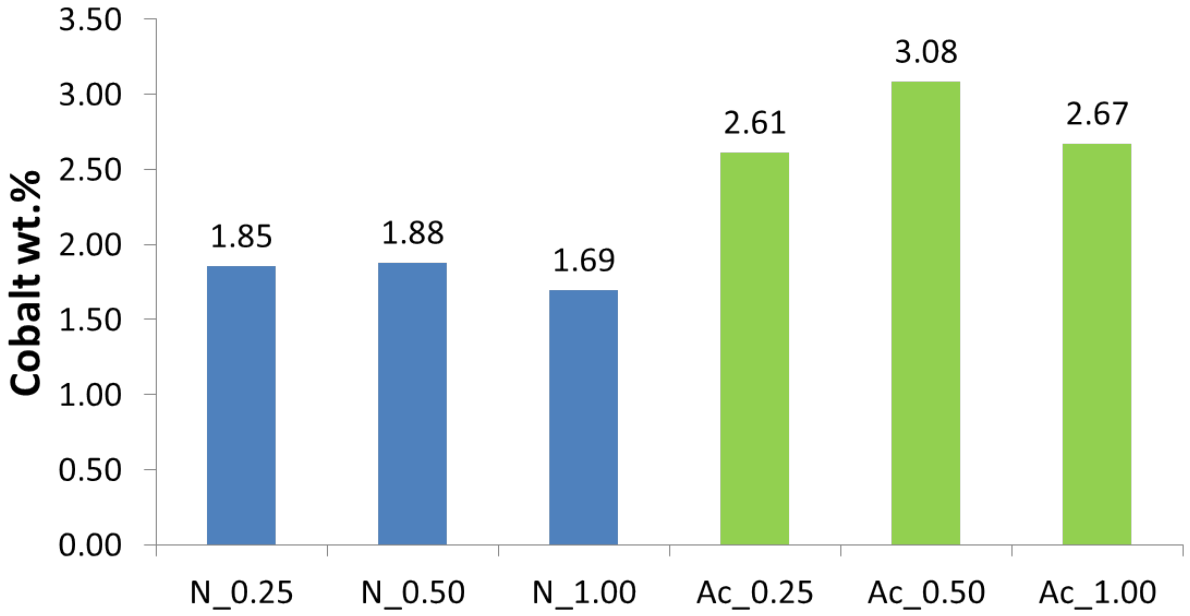

Figure 4.18: Calculated wt.% from ICP-MS for the concentration of silylation agents and precursor parameter study.

For the nitrate gels, it is seen a slight increase in cobalt uptake with increasing concentration of silylation agents, however, the increase is very small, almost negligible. The uptake is also lower for the highest concentration of silylation agents. The acetate gels experiences an overall higher uptake compared to the nitrate gels and reaches a much more distinct maximum cobalt content at 0.50 molar ratio of HMDZ:Si and HMDSO:Si before it decreases.

4.5.3 pH parameter study

For the gels from the pH parameter study, all gels seen in figure 3.5 were subject to ICP-MS analysis. The uptake in wt.% are shown in figure 4.19.

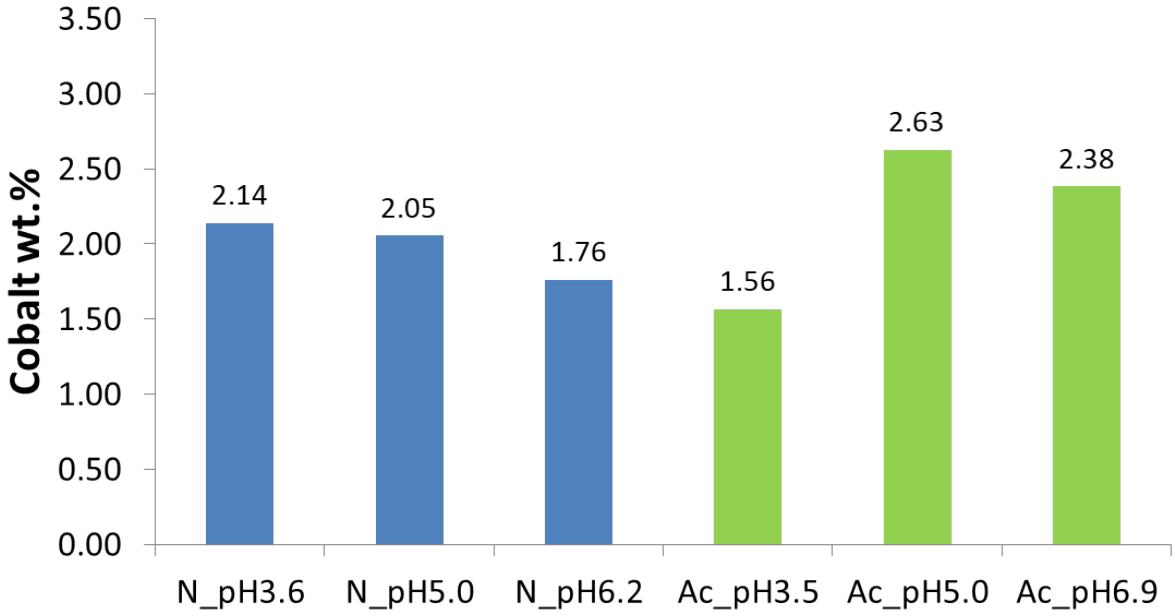

Figure 4.19: Calculated wt.% from ICP-MS for the pH parameter study.

For the nitrate gels, the uptake of cobalt is seen to decrease with increasing pH. This is rather unexpected, as the uptake is assumed to be higher at higher pH due to an increased concentration of siloxy groups for the cobalt to bond to as reported for copper.[38]

For the acetate gels, the uptake of cobalt is increasing from pH 3.5 to pH 5.0 which is experiencing the maximum uptake and then decreasing again at pH 6.9.

4.5.4 Ethanol and heptane washed gels

For all the gels washed with ethanol and heptane seen in figure 3.6, the ICP-MS uptake results in wt.% are shown in figure 4.20.

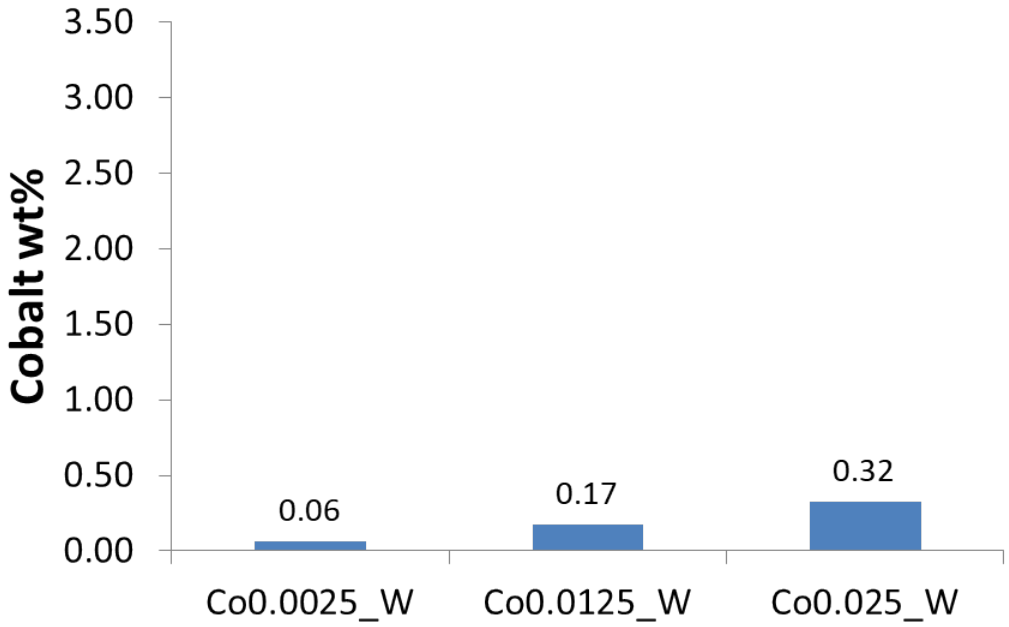

Figure 4.20: Calculated wt.% from ICP-MS for the ethanol and heptane washed gels.

The cobalt uptake in the washed gels is seen to be very low. This is likely due to the washing procedure removing most the cobalt present in the pores during solvent exchange. This indicates that the majority of the cobalt present in the gels is not embedded in the silica matrix during synthesis, but rather dissolved or dispersed in the porewater.

4.6 Scanning Electron Microscopy

Samples from each of the parameter studies were chosen for SEM, but unfortunately most of the samples were extremely difficult to get any good quality images from due to high charging despite being coated with carbon and due to low experience with the SEM apparatus. The only sample that had a somewhat decent quality was Co0.025 from the cobalt parameter study. These images are shown below.

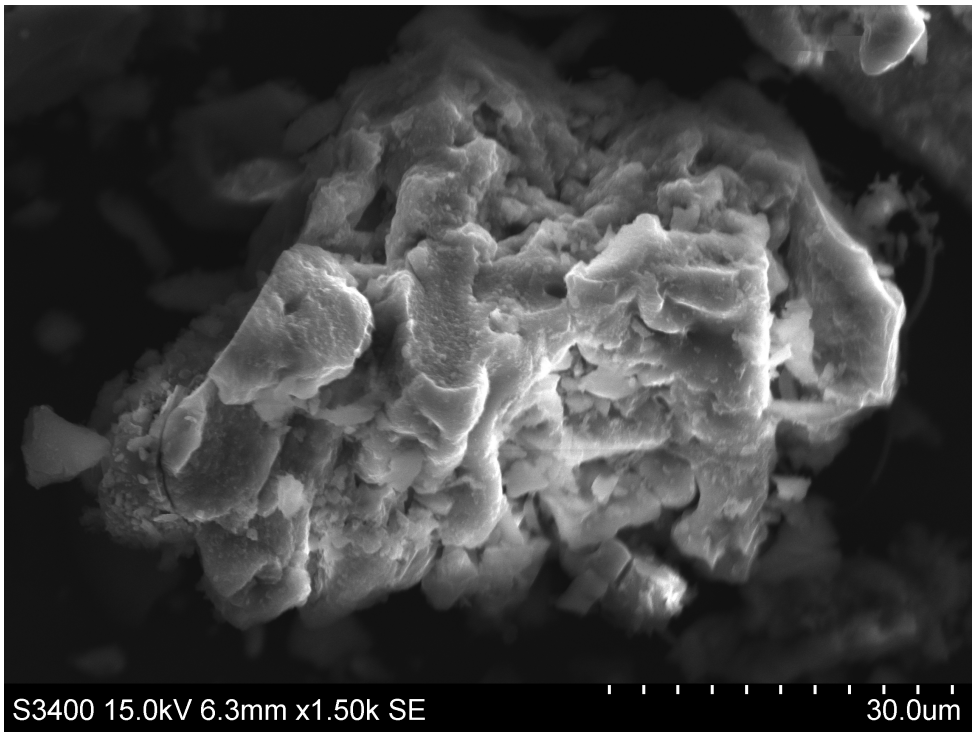

Figure 4.21: SEM image of sample Co0.025 at 15 kV with 1.50k magnification.

The particles observed had a wide range of both morphology and size, but with no particles >100 µm. As seen from image 4.21, the particle has a very rough and coarse surface due to the particle being mainly an agglomerate of smaller particles. This was the case for all larger particles observed. The smaller particles making up the larger agglomerates can be seen closer in image 4.22.

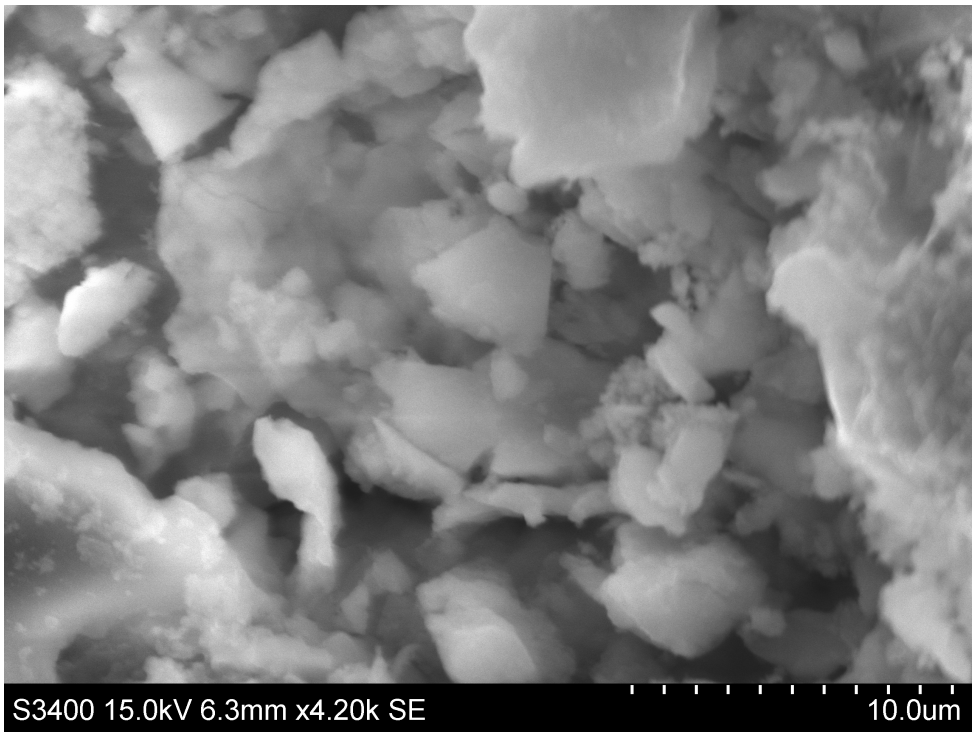

Figure 4.22: SEM image of sample Co0.025 at 15 kV with 4.20k magnification.

The smaller particles seen in image 4.22 appear to be a mix of different shapes with smooth surfaces, rough surfaces and straight edged cubic-like surfaces. This was observed for all agglomerates at this magnification. An even higher magnification was tried to see if secondary particles could be observed. This can be be seen in figure 4.23.

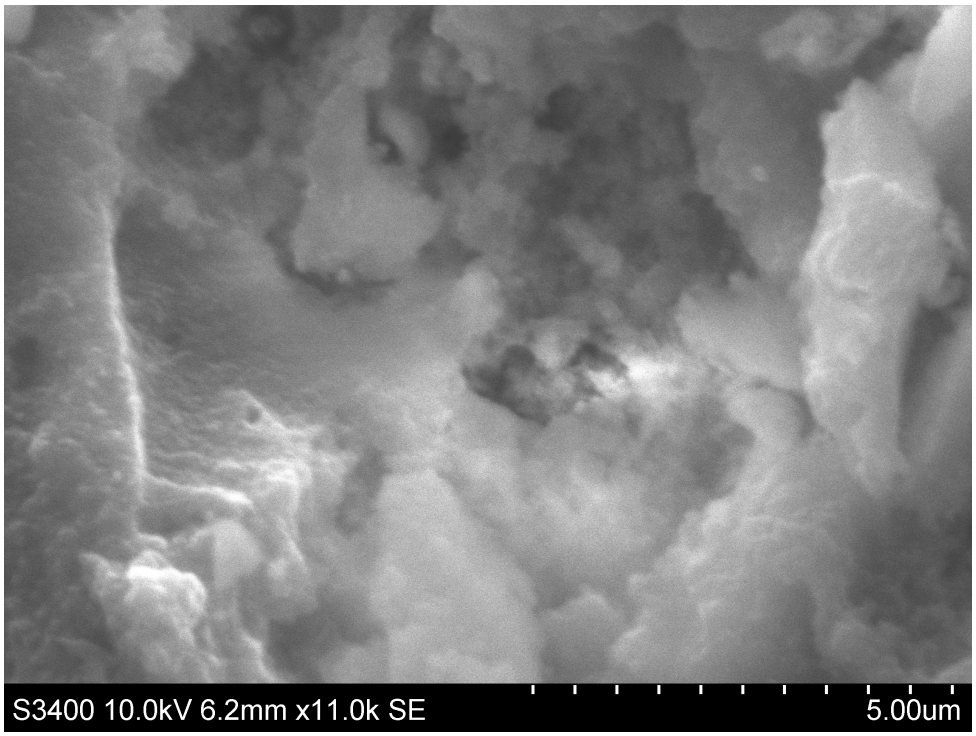

Figure 4.23: SEM image of sample Co0.025 at 10 kV with 11.0k magnification.

Due to poor image quality resulting from high charging of the surface, any secondary particles were not seen. The surface at this level of magnification seems to be a continuation of the coarse surface at higher magnifications. Primary particles were not expected to be seen at this magnification as their size are too small (2-6 nm).[8]

4.7 Thermogravimetric Analysis

Thermogravimetric analysis was performed on a selection of gels from the cobalt content parameter study and from the concentration of silylation agent parameter study to monitor thermal events by weight loss. As these gels are prepared by the APD method, weight loss due to evaporation of water and oxidation of surface silyl groups are expected. The results from TGA on these gels are regarded in this section.

4.7.1 Cobalt content parameter study

For the cobalt content parameter study, Co0.0025, Co0.025, Co0.10, Co0.15 and Co0.25 were subject to TGA. Figure 4.24 show the weight loss of these gels as a function of temperature.

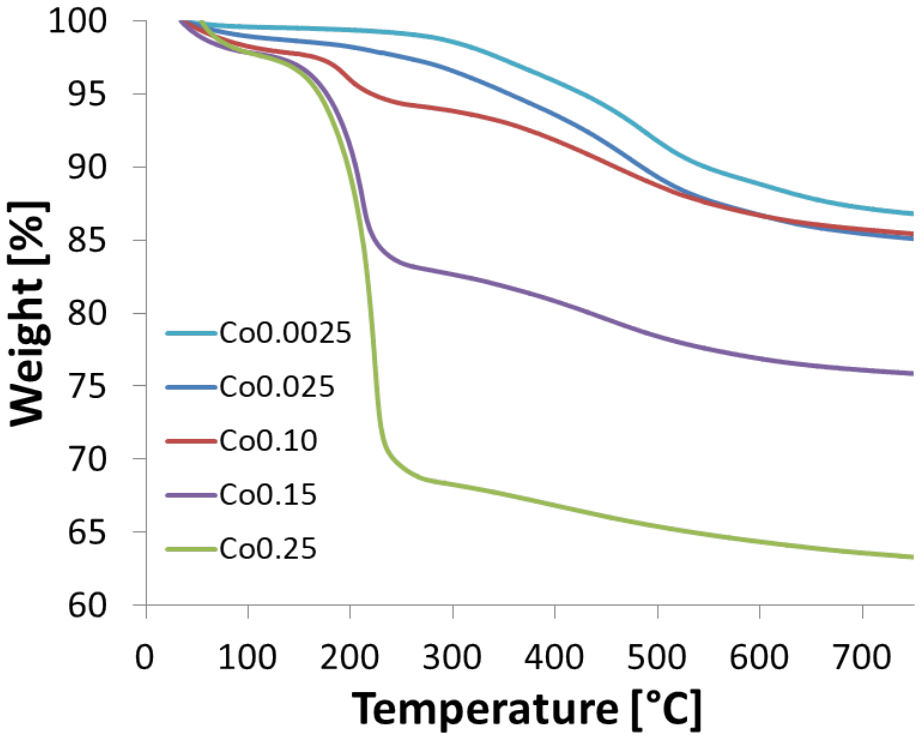

Figure 4.24: Illustration showing weight loss during heating i air to 750 °C. for gels in the cobalt content parameter study

The 0.5-3 % weight loss seen at 100 °C is attributed to evaporation of water remaining in the pores. A second weight loss is also seen at 170-250 °C, varying greatly in regard to the cobalt content of the gels. Co0.0025 experiences almost no weight loss in this region compared to Co0.25 which loses ~30 % of its weight. This is most likely due to removal of ammonia and water adsorbed on cobalt species as the magnitude of weight loss correlates to the cobalt content. This is the same pattern seen for copper incorporated aerogels prepared by the APD method.[75] A third weight loss seen at 250-750 °C, flattening out at ~550 °C, is also likely attributed to water and ammonia evaporating off as well as decomposition of nitrate and oxidation of surface silyl groups.[75] The gels with low Co-content seems to experience more weight loss in this region compared to the high Co-content gels, which could be explained by a lower concentration of silanols affiliated with cobalt due to a higher degree of silylation. The decomposition

of nitrate and removal of ammonia is supported by both literature[75] and the disappearance of ammonium nitrate in the calcined gels as seen in figure 4.8. Oxidation and replacement of the silyl groups with silanol groups is also reported in literature.[25,75] Although the weight losses observed in figure 4.24 are assumed to follow similar patterns and explanations as reported in literature, it would be preferable to perform TGA in combination with DSC and MS to confirm these results.

4.7.2 Concentration of silylation agents and precursor parameter study

For the concentration of silylation agents and precursor parameter study, all samples seen in figure 3.3 prepared with nitrate as cobalt precursor were subject to TGA. Figure 4.25 show the weight loss of these gels as a function of temperature.

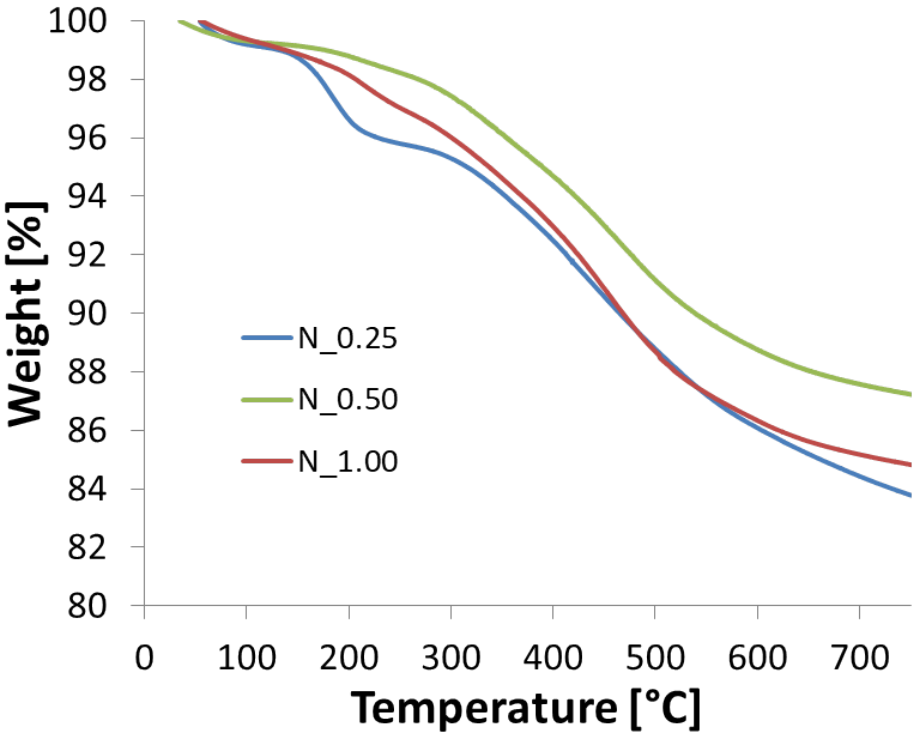

Figure 4.25: Illustration showing weight loss during heating i air to 750 °C. for cobalt nitrate gels in the silylation and precursor parameter study

The weight loss profiles seen in figure 4.25 resembles those seen in figure 4.24, resulting from the removal of water and ammonia as well as decomposition of nitrate and surface silyl groups. The sample N_0.25 prepared with the least amount of silylation agent experiences the high-

est weight loss, likely due to incomplete silylation of the surface and therefore an increased amount of remaining porewater and ammonia affiliated with surface silanol groups. The expected trend is decreased weight loss with increasing concentration of silylation agents due to a more complete surface modification causing less water and ammonia to remain in the pores, however the two other samples N_0.50 and N_1.00 does not follow the expected trend. The sample N_1.00 is seen to experience a larger weight loss than N_0.50, despite being prepared with a higher concentration of silylation agents.

4.8 Ex-situ X-ray Absorption Spectroscopy

Ex-situ XAS analysis was performed to determine the chemical environment and oxidation state of cobalt in synthesized gels. The samples Co0.10 as prepared and annealed at 700 °C from the cobalt precursor study were subject to ex-situ XAS analysis and the results will be regarded in this section.

4.8.1 XANES on Cobalt Silica Gels

The normalized XANES together with the first derivatives of Co0.10 as prepared and annealed at 700 °C as well as some cobalt reference compounds are shown in figure 4.26. The E_0 values were corrected with respect to Co-foil at 7709 eV as described in section 3.8.

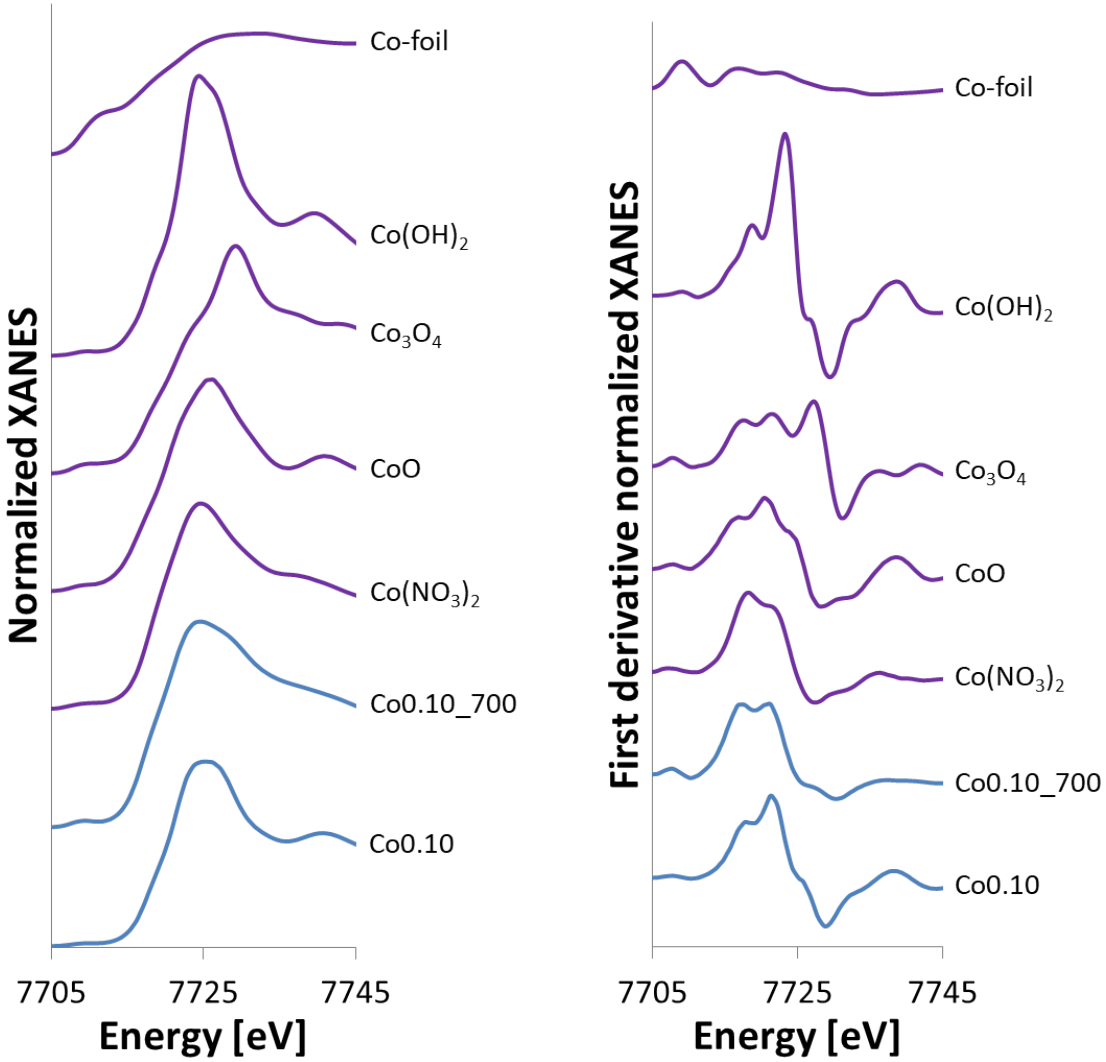

Figure 4.26: Normalized XANES (left) and the first derivative XANES (right) for the sample Co0.10 as prepared and annealed at 700 °C together with references.

The sample Co0.10 as prepared is not directly comparable to any of the reference compounds, however $Co(NO_3)_2$ show some resemblance in the first derivative with Co0.10 exhibiting a slightly more prominent peak at 7721 eV. This peak is also very prominent in $Co(OH)_2$ which could indicate the presence of some cobalt hydroxide species in the sample. The annealed sample show even more resemblance to $Co(NO_3)_2$ with the reduction in intensity of the peak at 7721 eV in the first derivative, indicating the removal of hydroxide species.

The E_0 values obtained from each of the two samples Co0.10 as prepared and annealed at 700 °C were used to determine the oxidation state of cobalt present in the samples. The E_0 values of the samples are plotted along a trend line drawn with respect to the references Co-foil (Co^0),

CoO (Co^{2+}) and Co_3O_4 (Co^{2+} and Co^{3+}) due to their linear relationship as explained in section 2.9.1. The relationship between E_0 and oxidation state of the samples are shown in figure 4.27.

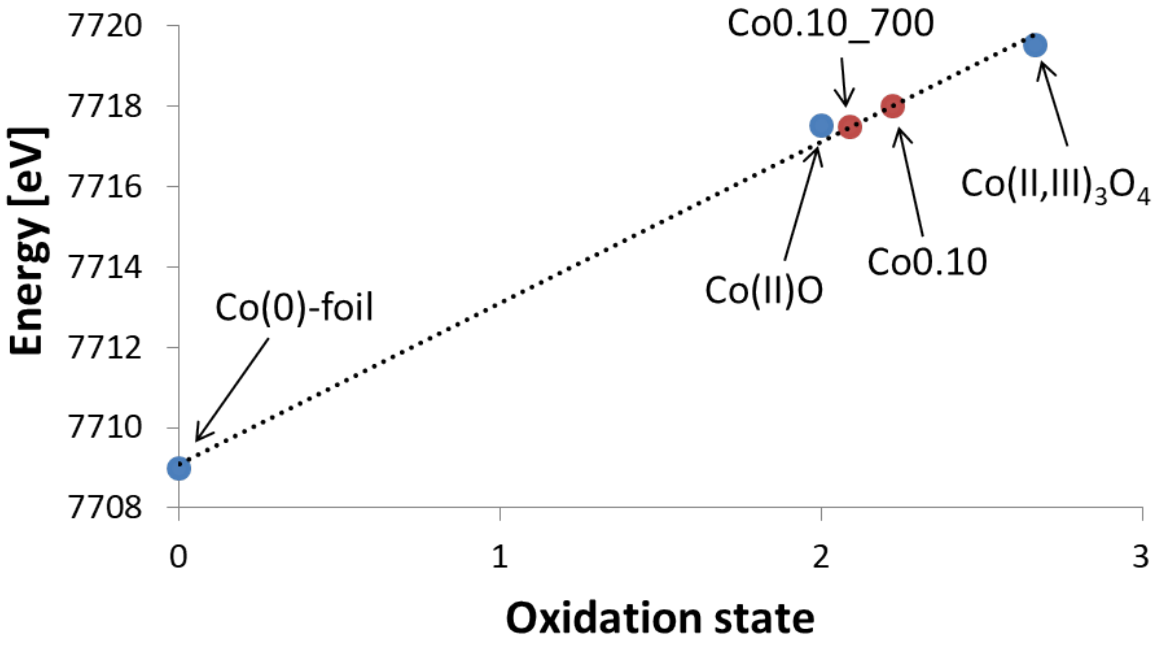

Figure 4.27: Plot of E_0 values and known oxidation states for references Co-foil, CoO and Co_3O_4 with an added trend line. Co0.10 as prepared and annealed at 700 °C is placed on the trend line based on their E_0 values.

From figure 4.27 it can be seen that both samples appear around oxidation state 2+, with Co0.10 as prepared moved slightly towards 3+. An oxidation state of 2+ is not unexpected as the cobalt precursor used in the two samples is cobalt nitrate, which also has an oxidation state of 2+. However, the position of the samples in the plot does not necessarily reflect their absolute true oxidation state as the XAS data is an average of all cobalt species present in the sample.

4.8.2 EXAFS on Cobalt Silica Gels

Through refinements in DL_EXCURV, a theoretical model concerning the first two shells was fitted to the experimental data of Co0.10 as prepared. The theoretical model fitted to the experimental χ(k) and Fourier transformed for the as prepared sample are shown in figure 4.28. The refined EXAFS values are shown in table 4.2.

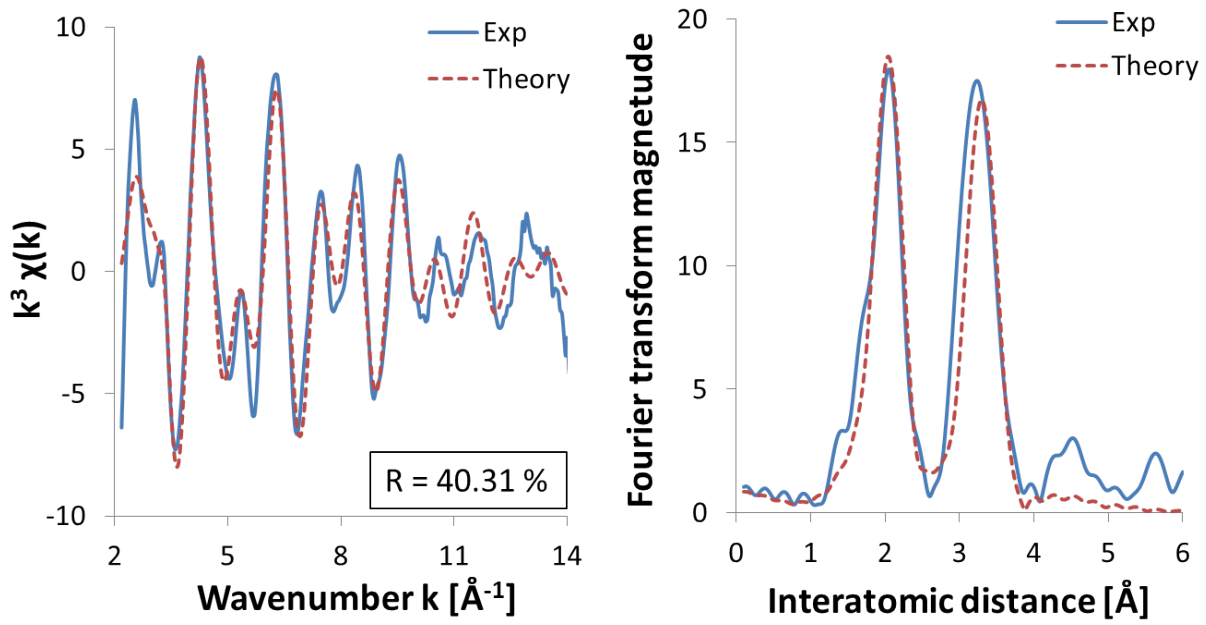

Figure 4.28: EXAFS least-square refinements of Co0.10 as prepared in k-space with k^3 weighting to the left and R-space to the right.

Table 4.2: EXAFS least-square refinement of Co0.10 as prepared.

Shell	**N**	**R [Å]**	**$2\sigma^2$ [Å^2]**	**E_F [eV]**	**R [%]**
Co-O	4.0(4)	2.087(9)	0.0133(3)	-2.9(7)	40.31
Co-Si	7(1)	3.327(9)	0.0135(3)		

The first and second shell was tried fitted to O and Si respectively and yielded an R-factor of 40.31, which is fairly decent, with a multiplicity of 4.0 oxygen atoms in the first shell at 2.09 Å and a multiplicity of 7 cobalt atoms in the second shell at 3.33 Å. Fourier filtering was applied to the second shell to verify Si from the gel structure to be the contributor. The refinements for the theoretical Co...Si, Co...Co and Co...Co+Si are shown in figure 4.29 together with the goodness of fit, R. The refinement values are shown in table 4.3.

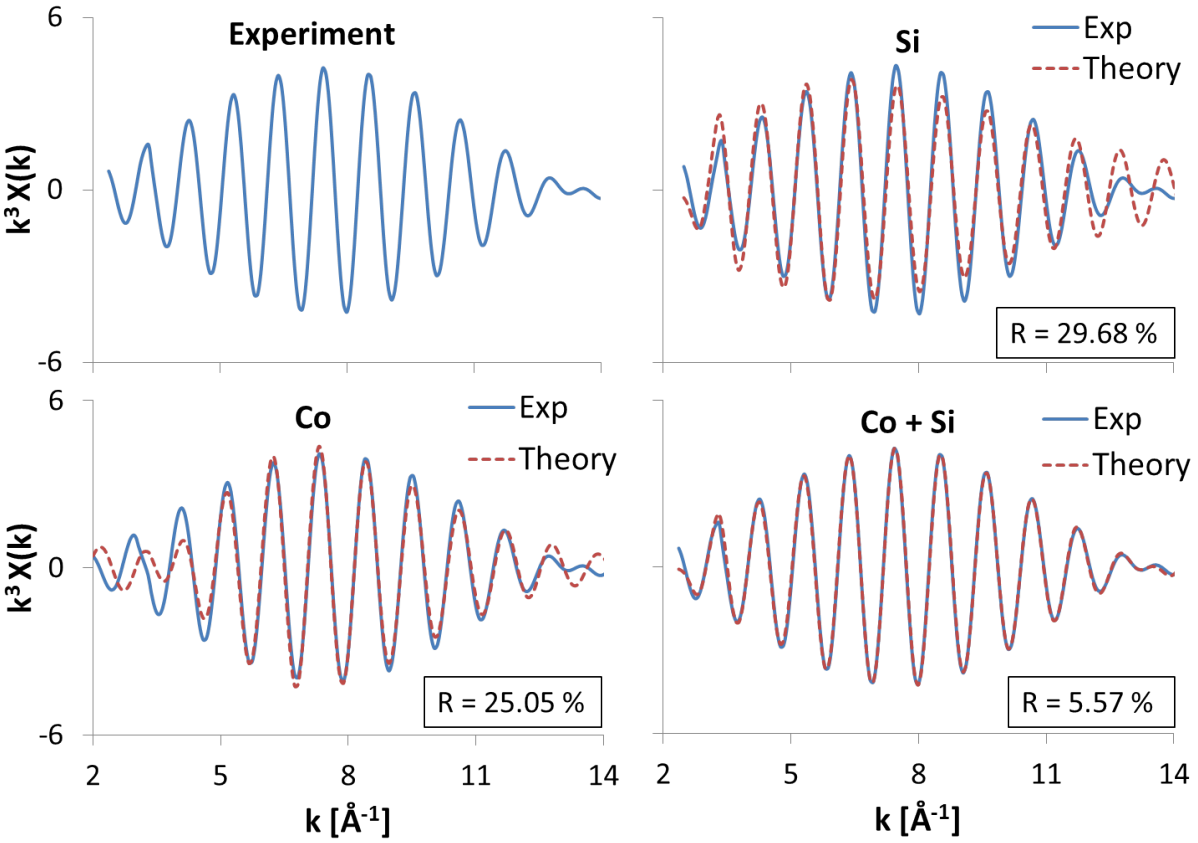

Figure 4.29: Fourier filtered second shell of Co0.10 as prepared with the theoretical model fitted to the experimental data as well as the goodness of fit (R).

Table 4.3: Fourier filtered second shell of Co0.10 as prepared.

Shell		**N**	**R [Å]**	**$2\sigma^2$ [Å^2]**	**E_F [eV]**	**R [%]**	**Δk [Å^{-1}]**
Co...Co+Si	Co	0.6(1)	3.063(4)	0.002(1)	0.1(2)	5.57	2.5-14.1
Co...Co+Si	Si	3.7(2)	3.312(3)	0.0064(5)			
Co...Co		4.6(2)	3.135(6)	0.018(2)	-6.4(9)	25.05	2.0-14.0
Co...Si		5.4(4)	3.284(5)	0.001(1)	2.1(6)	29.68	2.5-14.1

As seen in figure 4.29, the Co...Si pair and Co...Co pair both resulted in relatively low R-values and a good fit, however, the mixed Co+Si shell clearly yields the best fit. The filtered second shell consists of in average 0.6 cobalt atoms at 3.06 Å and 3.7 silicon atoms at 3.31 Å which could indicate partial incorporation of cobalt in single-site position, but with a fraction of it also as the unwanted Co-O-Co oxide species. However, oxygen and nitrogen are indistinguishable to Fourier filtering and possible Co-N species either in the pores, or frame-

work cobalt amine group stemming from side reactions between cobalt and ammonia during synthesis could contribute as well.

A theoretical model of the first two shells of the Co0.10 annealed at 700 °C sample was also tried fitted to the experimental χ(k) and the Fourier transformed in DL_EXCURV. The theoretical fit to the experimental data are shown in figure 4.30. The refined EXAFS values are shown in table 4.4.

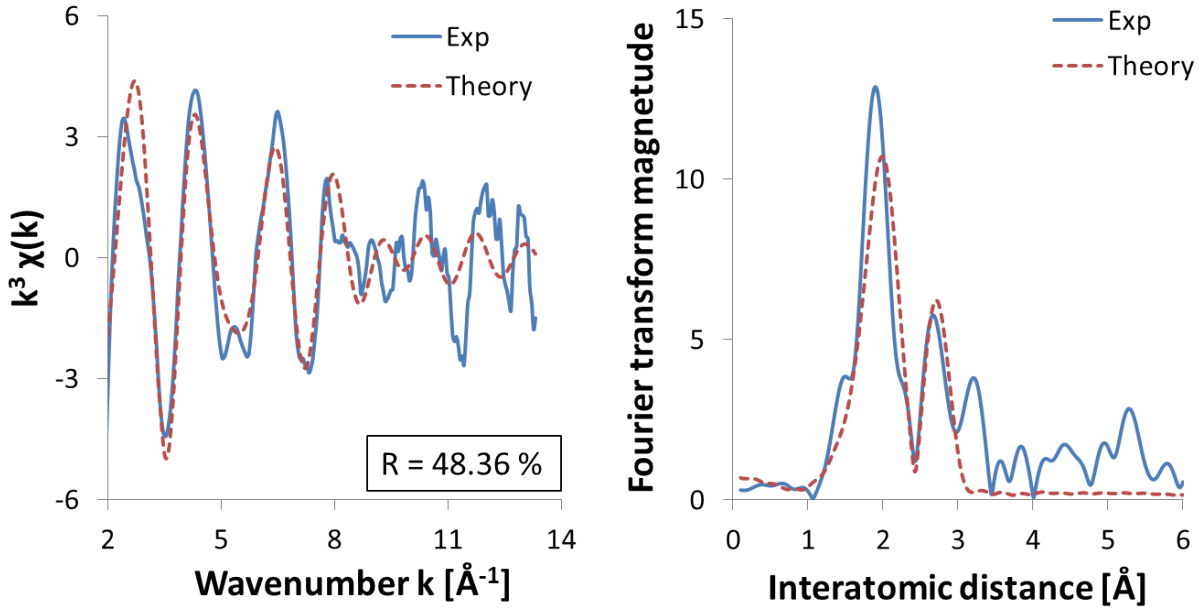

Figure 4.30: EXAFS least-square refinements of Co0.10 annealed at 700 °C in k-space with k^3 weighting to the left and R-space to the right.

Table 4.4: EXAFS least-square refinement of Co0.10 annealed at 700 °C.

Shell	**N**	**R [Å]**	**$2\sigma^2$ [Å^2]**	**E_F [eV]**	**R [%]**
Co-O	3.6(5)	2.06(1)	0.026(6)	-8.3(7)	48.36
Co-Si	1.2(5)	2.74(2)	0.012(7)		

The first and second shell was tried fitted to O and Si respectively as done for the as prepared sample, and yielded an R-factor of 48.36% and a multiplicity of 3.6 oxygen atoms in the first shell and 1.2 silicon atoms in the second shell. An R-factor of ~50 is in the high end of whats acceptable, and lowering the value is preferable to ensure a good model. Fourier filtering of the second shell was therefore performed to confirm Si as the contributor. The refinements

for the theoretical Co...Co, Co...Si and Co...Co+Si pairs are shown in figure 4.31 together with the goodness of fit, R. The refinement values are shown in table 4.5.

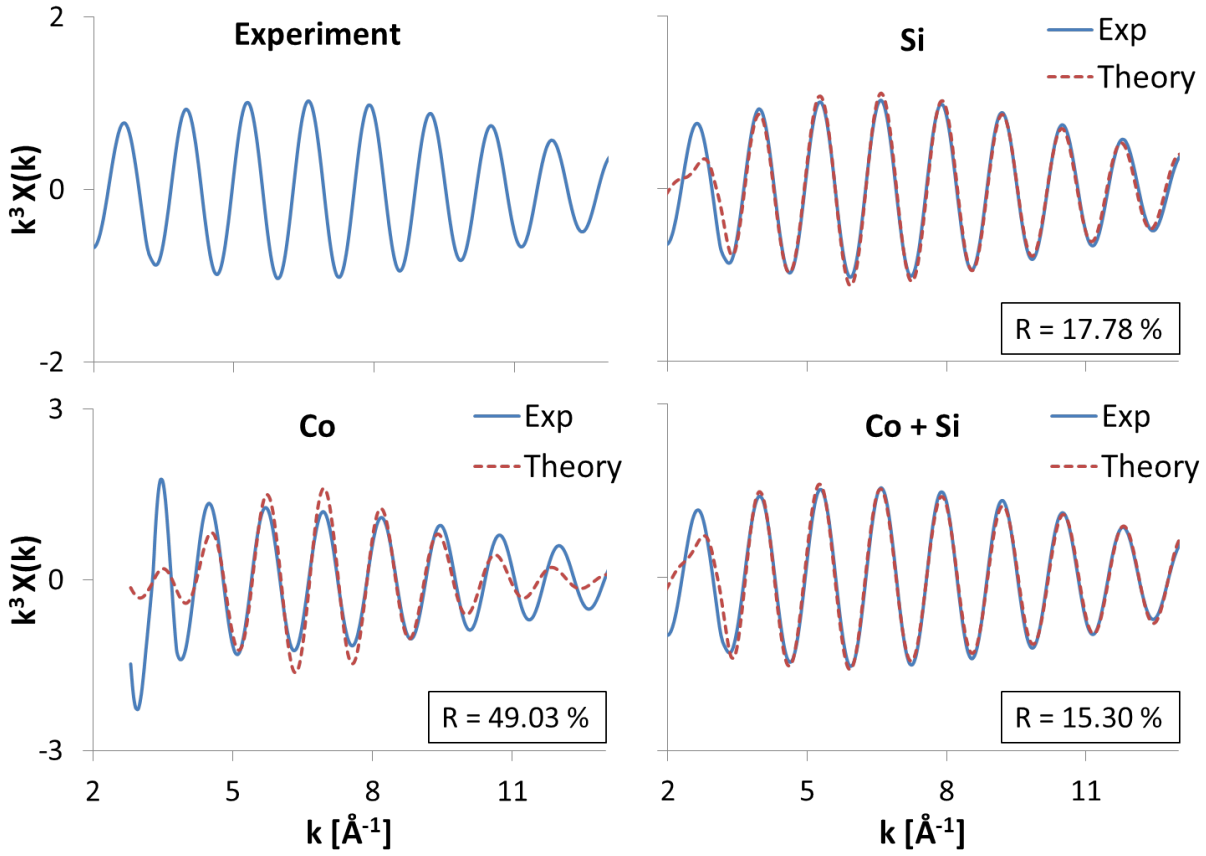

Figure 4.31: Fourier filtered second shell of Co0.10 annealed at 700 °C with the theoretical model fitted to the experimental data as well as the goodness of fit (R).

Table 4.5: Fourier filtered second shell of Co0.10 annealed at 700 °C.

Shell		**N**	**R [Å]**	**$2\sigma^2$ [Å^2]**	**E_F [eV]**	**R [%]**	**Δk [Å^{-1}]**
Co...Co+Si	Co	0.3(1)	2.65(3)	0.016(8)	-9.9(8)	15.30	1.9-13.1
Co...Co+Si	Si	1.08(8)	2.72(2)	0.008(1)			
Co...Co		1.9(6)	2.83(2)	0.025(6)	8(2)	49.03	2.9-13.3
Co...Si		0.93(7)	2.733(4)	0.008(1)	-10.3(6)	17.78	1.9-13.1

The Co...Co pair yielded an R-factor of 49.03%, which is higher than the original fit, while the two other pairs Co..Si and Co...Co+Si yielded the lowest values of 17.78% and 15.30% respectively. The fit is slightly better for the Co...Co+Si pair with a multiplicity of 0.3 cobalt atoms

at 2.65 Å and a multiplicity of 1.08 silicon atoms at 2.72 Å, indicating partial incorporation of cobalt in single-site.

4.9 In-situ X-ray Absorption Spectroscopy

In-situ studies was performed to monitor the change in chemical environment and oxidation state during heating in reducing and oxidizing atmospheres and catalytic performance. The sample Co0.05 calcined at 450 °C from the cobalt precursor study was chosen for in-situ analysis due to it having one of the highest surface areas of all gels in this work. This in addition to having a relatively high cobalt content without experiencing the significant reduction in porosity seen in gels with higher cobalt content. The results from in-situ XAS and catalytic performance will be regarded in this section.

4.9.1 XANES on Cobalt Silica Gels

During pretreatment of the sample in 75% H_2 and 25% Ar, several XANES scans was collected from room 100 °C to 600 °C to monitor reduction of cobalt in the sample. The E_0 values were corrected with respect to Co-foil at 7709 eV as described in section 3.8. Normalized XANES are shown in figure 4.32.

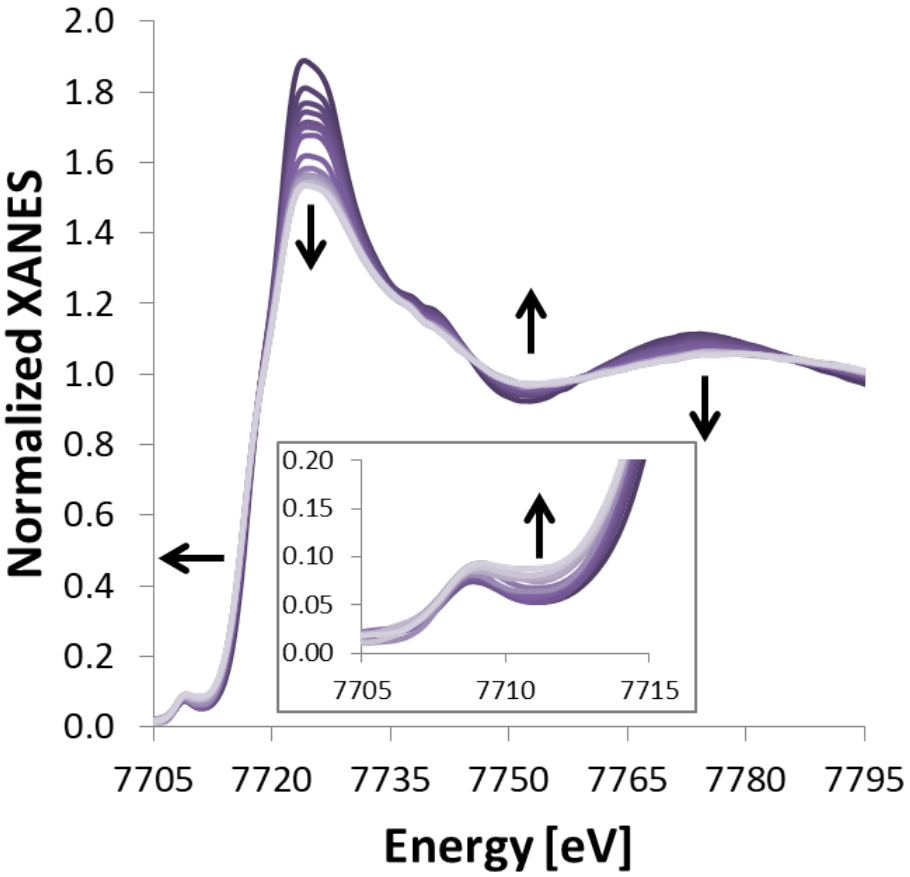

Figure 4.32: Normalized XANES for Co0.05 during pretreatment in 75% H_2 and 25% He with scans taken in a temperature range of 100-600 °C. XANES for lower temperatures are dark colored and gets lighter as temperature increases. Arrows show the movement of the XANES with increasing temperature.

From figure 4.32, heating in reducing atmosphere causes some reduction, however, reduction to metallic cobalt is not observed. Normalized XANES and first derivative of Co0.05 at 100 °C and after being held at 600 °C for 56 min together with reference compounds are shown in figure 4.33.

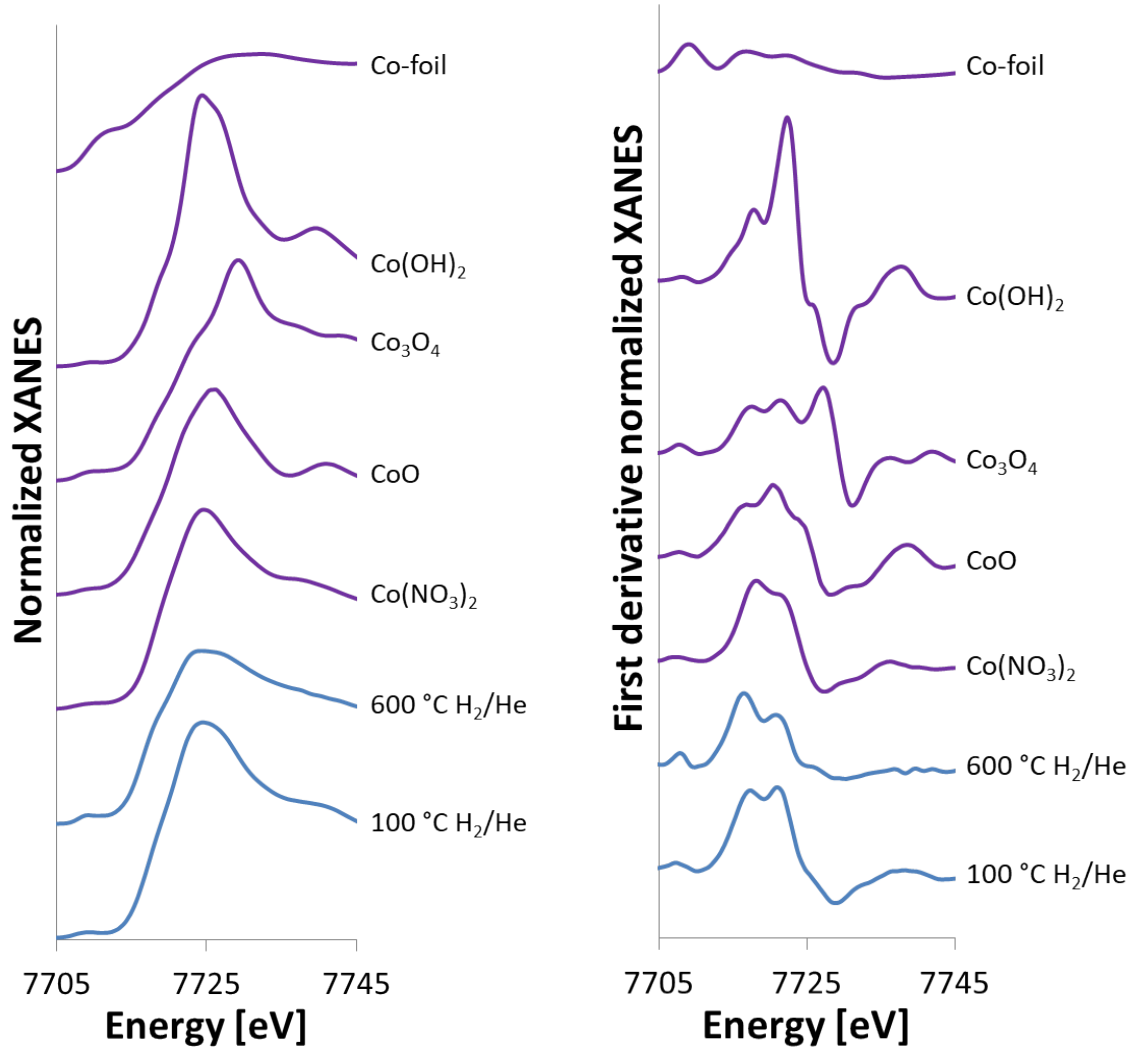

Figure 4.33: Normalized XANES (left) and the first derivative XANES (right) for the sample Co0.05 at room temperature and at after being held at 600 °C for 56 minutes together with references.

The change in near edge features are very small going from 100 °C to 600 °C. In the first derivative, a decrease is seen in the peak at 7721 eV and an increase in the peak at 7708 eV. XANES were also collected during decomposition of ammonia from 200 °C to 700 °C to monitor changes to the nature of cobalt. These are shown in figure 4.34.

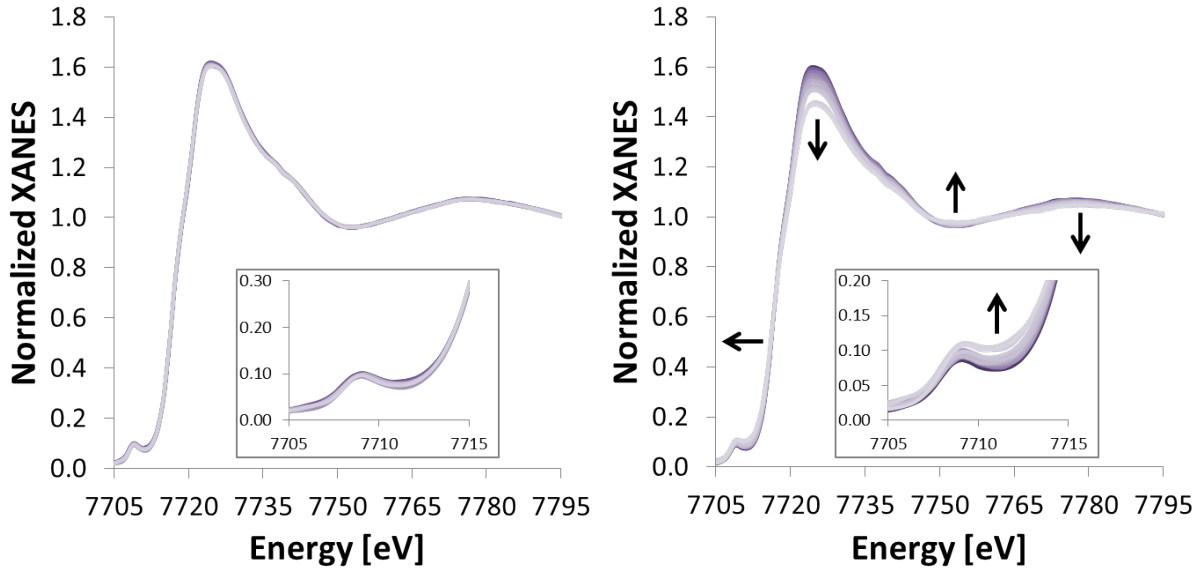

Figure 4.34: Normalized XANES for Co0.05 calcined at 450 °C during decomposition of ammonia (5% NH_3 in 95% He) with scans taken in a temperature range of 200-410 °C to the left and 420-700 °C to the right. XANES for lower temperatures are dark colored and gets lighter as temperature increases. Arrows show the movement of the XANES with increasing temperature.

The XANES collected during decomposition of ammonia could be split into to parts depending on temperature. Little to no change was observed during heating from 200 °C to ~420 °C as seen in figure 4.34. However, at temperatures higher than ~420 °C, change is observed, indicating further reduction of the sample. This is unexpected as the sample is heated in an oxidizing atmosphere.

4.9.2 EXAFS on Cobalt Silica Gels

Several EXAFS scans were collected after the sample had reached 700 °C. Due to a quite noisy signal after k = 7, several scans were merged, which improved the signal some, but still contained a fair amount of noise. This made the fitting process difficult. The theoretical fit to the experimental data are shown in figure 4.35. The refined EXAFS data values are shown in table 4.6.

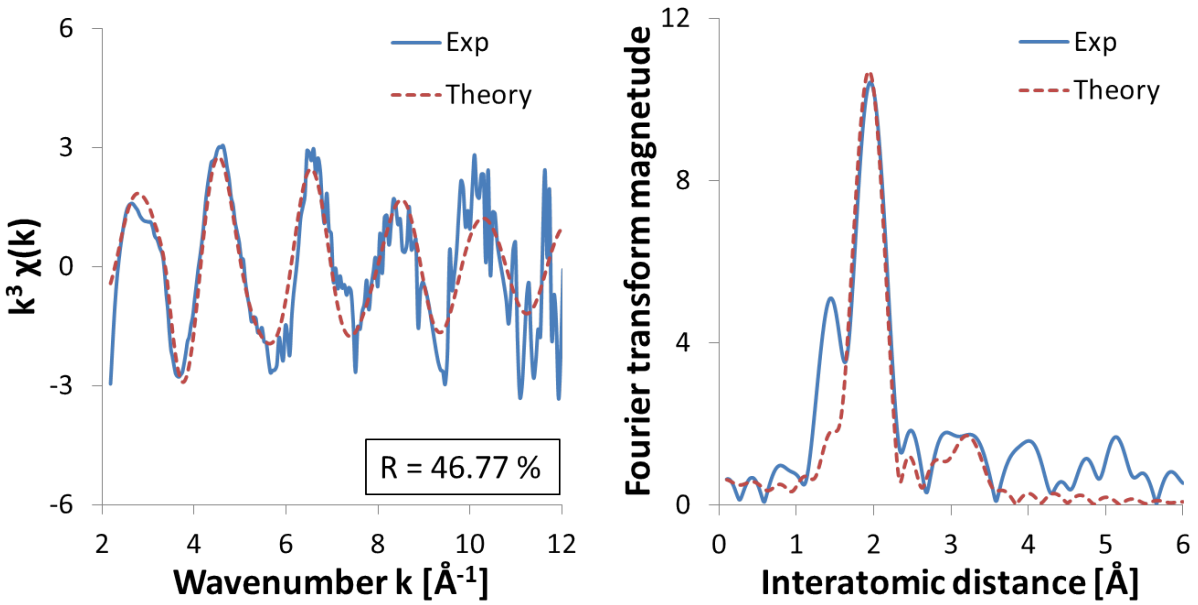

Figure 4.35: EXAFS least-square refinements of Co0.10 as prepared in k-space with k^3 weighting to the left and R-space to the right.

Table 4.6: EXAFS least-square refinement of Co0.05 calcined at 450 °C.

Shell	**N**	**R [Å]**	**$2\sigma^2$ [Å^2]**	**E_F [eV]**	**R [%]**
Co-O	1.2(2)	1.98(1)	0.006(3)	-3(1)	46.77
Co-Si	0.71(8)	3.22(5)	0.02(3)		

As for the previous ex-situ samples. the first and second shells were fitted to O and Si respectively and yielded an R-factor of 46.77%, a multiplicity of 1.2 oxygen atoms in the first shell and 0.71 silicon atoms in the second shell. Even though the R-factor is relatively low, the fitting was quite difficult due to the noisy data. Fourier filtering was therefore performed on the second shell to confirm Si as the contributor. Refinements for the theoretical Co...Co, Co...Si and Co...So+Si pairs are shown in figure 4.36. Refinement values are shown in table 4.7.

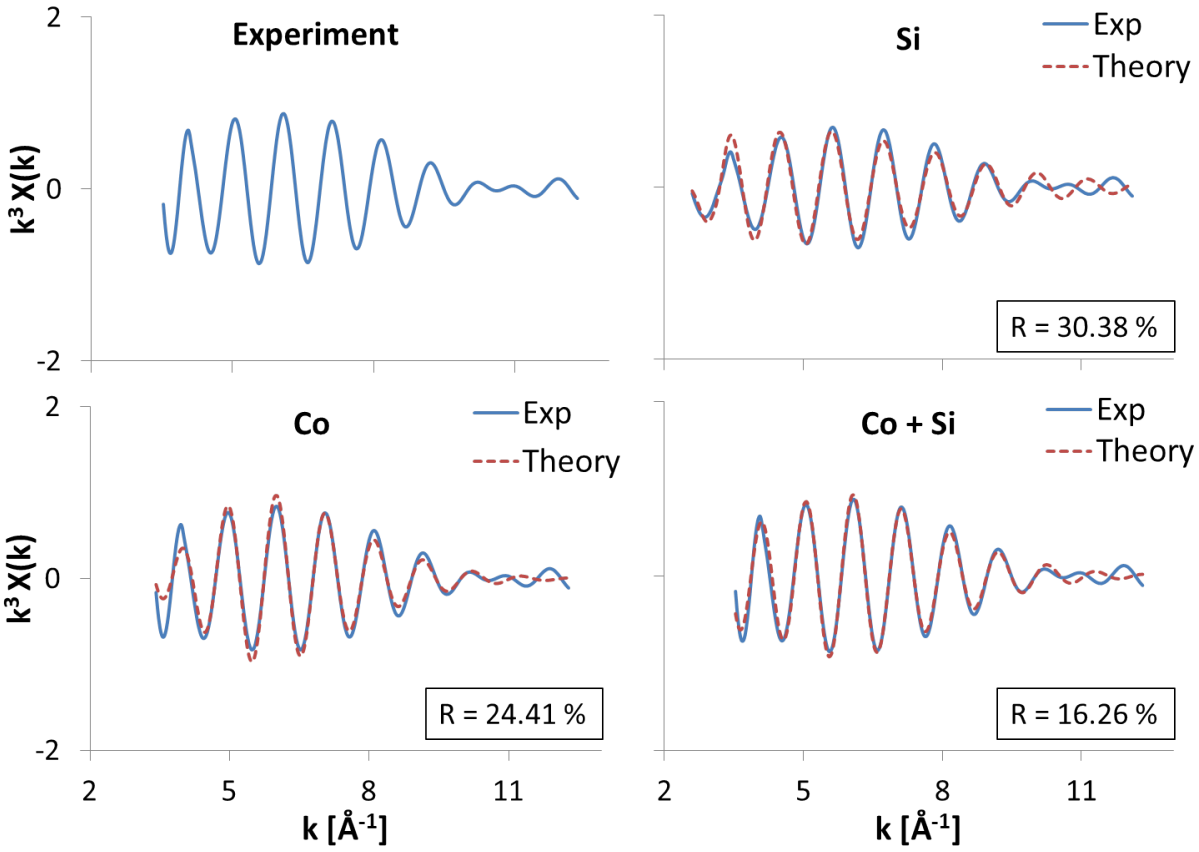

Figure 4.36: Fourier filtered second shell of Co0.05 calcined at 450 °C with the theoretical model fitted to the experimental data as well as the goodness of fit (R).

Table 4.7: Fourier filtered second shell of Co0.05 calcined at 450 °C.

Shell		**N**	**R [Å]**	**$2\sigma^2$ [Å^2]**	**E_F [eV]**	**R [%]**	**Δk [Å^{-1}]**
Co...Co+Si	Co	2(1)	3.24(4)	0.040(5)	24(1)	16.26	3.5-12.2
Co...Co+Si	Si	1.4(9)	3.38(6)	0.04(5)			
Co...Co		3.1(4)	3.25(1)	0.046(3)	20.7(9)	24.41	3.4-12.3
Co...Si		1.11(9)	3.157(7)	0.023(2)	3.7(5)	30.38	2.6-12.0

The Co...Co+Si pair yields the best fit at R = 16.26% with a multiplicity of 2 cobalt atoms at 3.24 Å and a multiplicity of 1.4 silicon atoms at 3.38 Å. The low R-factor value for the Co...Co+Si pair indicates partial incorporation of cobalt in single-site.

4.9.3 Catalytic testing

After pre-treatment, during ammonia decomposition, the catalytic activity was monitored by feeding the reaction products into a mass spectrometer. The conversion of ammonia is shown in figure 4.37.

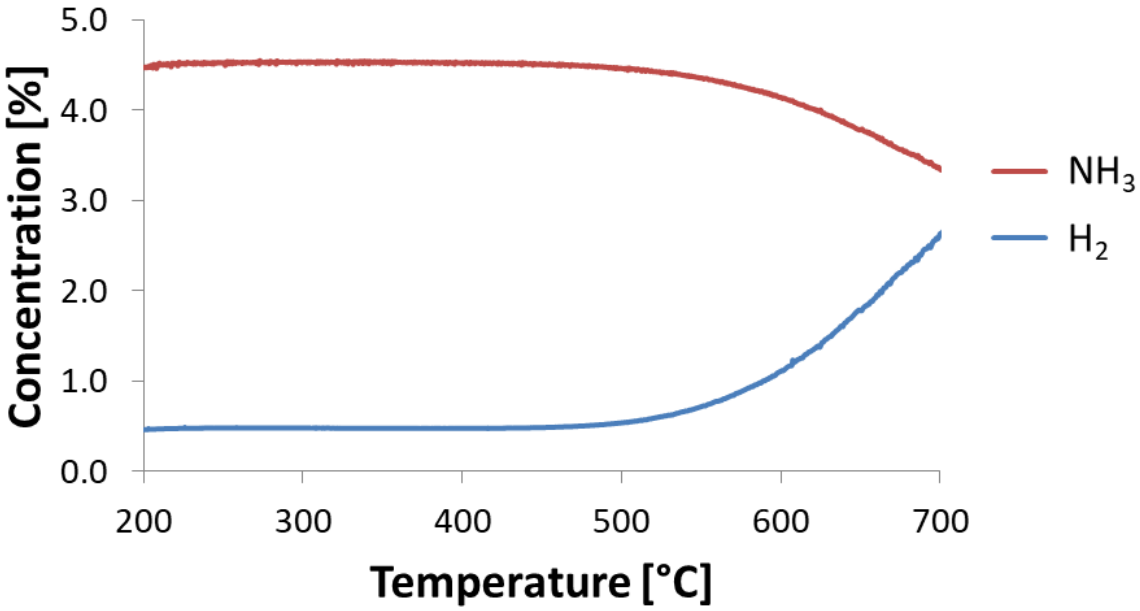

Figure 4.37: NH_3 conversion for Co0.05 during in-situ XAS with a feed of 5% NH_3 in He.

From figure 4.37 the sample is seen to be active for ammonia decomposition starting at ~420 and increasing in activity as temperature rises. At 700 °C the sample has a calculated conversion of ammonia of 24.8%, using the method described in section 3.7.

4.10 Catalytic testing and FT-IR Spectroscopy

The sample Co0.05 calcined at 450 °C that was analyzed with in-situ XAS, was also tested for catalytic performance in house with a tube reactor connected to an FT-IR analyzer as described in section 3.7. The conversion of ammonia as a function of temperature is shown in figure 4.38. The results were provided by the courtesy of ph.D. candidate Karsten Granlund Kirste.

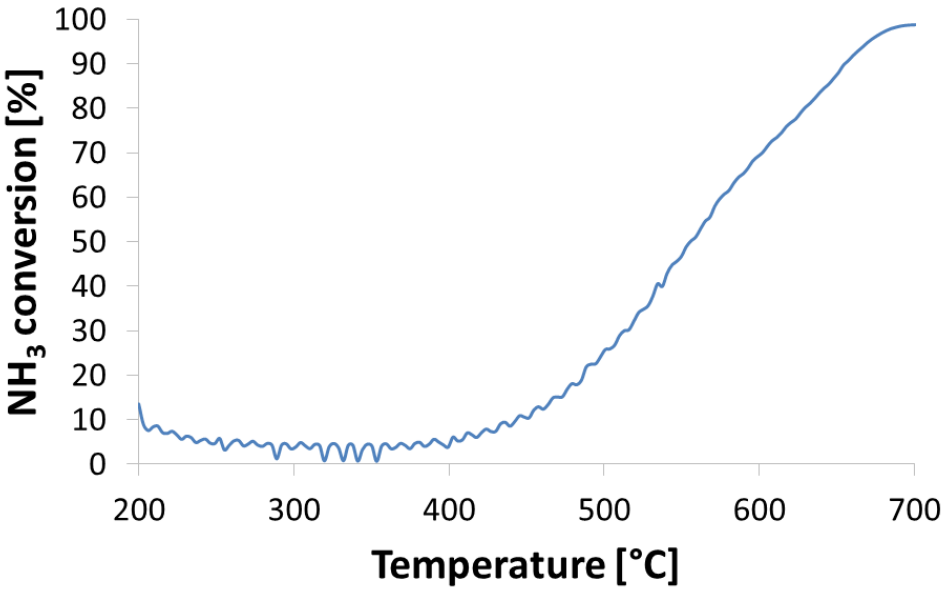

Figure 4.38: NH_3 conversion for Co0.05_450

From figure 4.38, the sample is seen to be active for ammonia decomposition, starting at ~420 °C and increasing in activity until reaching a conversion of ~99% at 700 °C, which is similar to the findings of Zhang et al. regarding cobalt on carbon nanotubes.[52] Conversion was calculated at shown in section 3.7.

5 Discussion

5.1 Achieving single-site via parameter changes

The main goal of this thesis was to functionalize and incorporate cobalt into the matrix of silica aerogels in single-site via the newly developed synthesis route using cheap sodium silicate and the APD method. Due to this never having been done before, several parameter studies were performed to investigate the possibility of such incorporation through changing the parameters; Co-content, pH of sol at gelation, concentration of silylation agents and precursor. The choice of values for the different parameters were inspired by the work of T. Kristiansen.[3] A washing procedure was also performed with the intention to remove cobalt species in the pores interfering with XAS analysis. High surface area and porosity and high cobalt content is generally desired due to the possibility of a high dispersion and good catalytic activity.

Considering the amount of cobalt in the gels, an upper limit was not observed. However, this does not necessarily mean cobalt is successfully incorporated into single-site. Cobalt species in the gel pores and not in the silica matrix is supported by XRD, but only for heat treated gels. In as prepared gels prepared via the CP-method, the only crystalline phase appearing correspond to that of ammonium nitrate, even at high cobalt concentration. After calcining and annealing, the phase disappear, likely due to decomposition of nitrate and removal of ammonia which is supported by the findings from TGA. However, the crystalline phases appearing after calcining and annealing stemming from cobalt oxide and cobalt silicate, indicates that some of the cobalt species are not thermally stable. The formation of such cobalt species can typically be explained by two scenarios: 1) formation of cobalt oxide (CoO_x) phases and cobalt silicate (Co_2SiO_4) due to cobalt and silicon being expelled from the gel structure during heating, or 2) nanophase CoO_x and Co_2SiO_4 sintering during heating to form larger particles inside the silica aerogel pores. Although the presence of such phases indicate unsuccessful incorporation of single-site cobalt and Fourier filtering of XAS results show a mix of Co...Co and Co...Si, this does not confirm an unsuccessful incorporation. The fact that Co...Si is also seen, indicates a variety of cobalt which could include the presence of single site cobalt.

Cobalt uptake is also expected to be greater for gels prepared with a higher pH from the SD method due to the increased surface siloxy groups available for cobalt to bond to. This is, however, not observed for either nitrate prepared gels or acetate prepared gels. The reason behind this effect is not known. Concentration of silylation agents seems to have almost no effect on gels prepared

Considering the porosity, all gels prepared in this work regardless of parameter study, show presence of mesopores with an average pore width between 33 Å and 138 Å and is within the definition of an aerogel. However, the difference in pore distribution and average pore width varies greatly depending on the parameter in question. Gels from the cobalt content parameter study prepared via the CP method, show a trend with increasing porosity and surface area with increasing cobalt content to a certain point before decreasing. The decrease in porosity and surface area at higher cobalt content can be explained by three possible scenarios; 1) HMDZ reacts with residual cobalt cations rather than the surface silanols of the wet gel causing excessive cross-linking through condensation; 2) HMDZ reacts with cobalt cations already incorporated into the silica gel matrix rather than silanols, producing cobalt amine complexes or cobalt hydroxide complexes instead, thus resulting in increased cross-linking; 3) Silanol groups associated with cobalt causing shrinkage during the drying process due to their hydrophilic nature increasing the capillary forces exerted on the gel.[3]

Gels prepared with cobalt acetate yielded the lowest surface area between the two precursors, however, cobalt acetate gels generally had better cobalt uptake. The difference in porosity of acid catalyzed and base catalyzed gels are rather expected. Acid catalyzed gels generally tend to form a yarn-like structure with small pores compared to base catalyzed gels with a "pearl-necklace" structure, limiting diffusion during solvent exchange. Remaining water in the pores therefore causes a higher degree of shrinking. However, the difference in trends seen between nitrate and acetate prepared gels is difficult to explain.

To see if some of the cobalt indeed was in single site, a washing procedure based on the works of Rao et al.[24,30] was tried analyzed with XAS. This method yielded superior gels in terms of surface area and pore size, but unfortunately the cobalt content was too low to be detected and did not produce any usable results. Due to time limitations, samples from other parameter studies were unfortunately not analyzed by XAS.

Overall, single-site cobalt is a possibility as the XAS results show, however, these results only cover gels from the cobalt content parameter study. Single-site cobalt in gels from the other parameter studies is impossible to confirm from the characterization methods they have been subject to.

5.2 Catalytic properties of cobalt in silica aerogels

The sample Co0.05 prepared from the CP method calcined at 450 °C from the cobalt content parameter study that was subject to catalytic testing both in-situ during XAS analysis and in a tube reactor in house, was shown to be catalytically active for ammonia decomposition. However, different catalytic performances were observed, even though the conditions were the same during both tests. The in house testing yielded a ~75% higher conversion compared to the results from the XAS analysis, which is indeed a very big difference. This could possibly be explained by a low sensitivity towards ammonia detection of the FT-IR analyzer in combination with too high dilution, overestimating the conversion. The high conversion results from the FT-IR is however in line with previous reports from Zhang et al., giving a near 100% conversion.[52]

Although the gel is observed to be active in decomposition of ammonia, the catalytically active cobalt species in the gel is difficult to determine. XRD show the presence of oxide phases, which is known to be catalytically active in ammonia oxidation[76] and cobalt silicate, while EXAFS indicates a combination of cobalt oxide and Co-O-Si species. It is unknown if the Co-O-Si species are single-site cobalt or cobalt silicate. The cobalt species present in the gel were also able to reduce somewhat during XAS pretreatment in H_2 and He. A high degree of reduction however, is not observed, which could indicate stabilization of cobalt in the silica matrix, further supporting single-site cobalt. Switching to NH_3 and He, the cobalt species seems unaffected until a temperature of ~420 °C is reached, which is also the point at which ammonia decomposition start. Interestingly, from this point, cobalt is observed to reduce even further. This is unexpected and difficult to explain, as the oxidative reaction conditions should not support such behavior. With all these different cobalt species present, it is not possible at this stage to pinpoint which are the catalytically active one(s), however metallic cobalt, single site cobalt and cobalt oxides are all known to be catalytically active for ammonia

decomposition.[77–79]

6 Conclusion

Incorporation of single-site cobalt is inconclusive, however, catalytically active silica aerogel-supported cobalt for ammonia decomposition was successfully synthesized. The reducibility of cobalt is low, but it was observed to be able to reduce somewhat in reducing atmosphere and most surprisingly in oxidative atmosphere as well. The exact catalytically active specie(s) are unknown and a wide variety of active cobalt species is likely.

An upper limit of cobalt uptake was not encountered, however, most of the cobalt is likely in the pores of the gels and not as a part of the gel structure. Gels prepared with cobalt acetate had generally higher uptake of cobalt than those prepared with cobalt nitrate regardless of the two synthesis routes (SD and CP). Concentration of silylation agent had little effect on cobalt uptake for gels prepared with cobalt nitrate, but gels prepared with cobalt acetate had a maximum uptake at 0.5 molar ratio HMDZ:Si and HMDSO:Si. A low pH of 3.6 resulted in the highest uptake for gels prepared with nitrate, while gels prepared with acetate had a maximum uptake at pH 5.0

High surface area and porosity was achieved for all gels synthesized in this thesis, with gels prepared with cobalt nitrate and high concentration of silylation agent yielding the most porous gel. The lowest surface area and porosity was seen for acid catalyzed gels, with gels prepared with cobalt acetate having the lowest between the two precursors.

7 Further work

Since only a few gels prepared in this thesis were subject to XAS, the exact nature of cobalt in the gels from parameter studies other than the cobalt precursor parameter study is difficult to determine. More XAS should be performed on these gels to determine any possible changes to cobalt in the silica aerogels depending on these parameters. Washed gels with a higher amount of cobalt added during synthesis could also possibly give more usable XAS results to give answers to how cobalt is present in the silica matrix.

More catalytic testing should be performed on gels from other parameter studies to see if those changes affect the catalytic performance.

Other parameter studies could be performed. The concentration of silica in the sol was kept constant for all gels in this thesis. This could also be its own parameter for future studies, investigating the effect of varying silica concentration together with varying cobalt concentration to see if there is an optimal ratio. More extensive investigation on precursors with oxidation states other than 2+ could also be interesting.

Additional characterization such as IR spectroscopy to investigate changes of the surface between different parameter studies, TEM to get a closer view of the topography than SEM can provide, and TGA in combination with DCS and MS to confirm the thermal events observed in this thesis.

Bibliography

[1] D. Cheddie. Ammonia as a Hydrogen Source for Fuel Cells: A Review. chapter 13. InTech, Rijeka, 2012.

[2] S. Chiuta, R. C. Everson, H. W. J. P. Neomagus, and D. G. Bessarabov. Hydrogen production from ammonia decomposition over a commercial Ru/Al_2O_3 catalyst in a microchannel reactor: Experimental validation and CFD simulation. *International Journal of Hydrogen Energy*, 41(6):3774 – 3785, 2016.

[3] T. Kristiansen. *Aerogels; a new class of materials for catalytic purposes.* PhD thesis, NTNU, 2013.

[4] Z. Lendzion-Bielun, U. Narkiewicz, and W. Arabczyk. Cobalt-based catalysts for ammonia decomposition. *Materials*, 6(6):2400–2409, 2013.

[5] S. S. Kistler. Coherent expanded aerogels and jellies. *Nature*, 127:741, 1931.

[6] H.-H. Park E. S. Kang J. L. Gurav, I.-K. Jung and D. Y. Nadargi. Silica Aerogel: Synthesis and Applications. *Journal of Nanomaterials*, 2010:11, 2010.

[7] A. S. Dorcheh and M. H. Abbasi. Silica aerogel; synthesis, properties and characterization. *Journal of Materials Processing Technology*, 199:10 – 26, 2007.

[8] L. Chu, M. I. Tejedor-Tejedor, and M. A. Anderson. Particulate sol-gel route for microporous silica gels. *Microporous Mterials*, 8(5-6):207 – 213, 1997.

[9] P. M. Shewale, A. V. Rao, and A. P. Rao. Effect of different trimethyl silylating agents on the hydrophobic and physical properties of silica aerogels. *Applied Surface Science*, 254(21):6902 – 6907, 2008.

[10] R. G. Jones. *Compendium of Polymer Terminology and Nomenuclature, IUPAC Recommendations 2008.* Royal Society of Chemistry Publishing, 2009.

[11] M. A. Aegerter, N. Leventis, and M. M. Koebel. *Aerogels Handbook.* Springer, 2011.

[12] C. J. Brinker and G. W. Scherer. *Sol-Gel Science.* Academic Press, 1990.

[13] Y. A. Attia. *Sol-Gel Processing and Applications.* Plenum Press, 1994.

[14] Z. A. Alothman. A review: Fundamental Aspects of Silicate Mesoporous Materials. *Materials*, 5(12):2874 – 2902, 2012.

[15] C. J. Brinker and G. W. Scherer. Sol ⟶ gel ⟶ glass: I. Gelation and gel structure. *Journal of Non-Crystalline Solids*, 70(3):301 – 322, 1985.

[16] M. J. van Bommel and A. B. de Haan. Drying of silica aerogel with supercritical carbon dioxide. *Journal of Non-Crystalline Solids*, 186:78 – 82, 1995.

[17] F. Schwertfeger, D. Frank, and M. Schmidt. Hydrophobic waterglass based aerogels without solvent exchange or supercritical drying. *Journal of Non-Crystalline Solids*, 225:24 – 29, 1998.

[18] S.-W. Hwang, H.-H. Jung, S.-H. Hyun, and Y.-S. Ahn. Effective preparation of crack-free silica aerogels via ambient drying. *Journal of Sol-Gel Science and Technology*, 41(2):139 – 146, 2007.

[19] G. W. Scherer. Aging and drying of gels. *Journal of Non-Crystalline Solids*, 100(1):77 – 92, 1988.

[20] F. Schwertfeger, N. Hüsing, and U. Schubert. Influence of the nature of organic groups on the properties of organically modified silica aerogels. *Journal of Sol-Gel Science and Technology*, 2(1):103 – 108, Jan 1994.

[21] J. L. Gurav, A. V. Rao, and U. K. H. Bangi. Hydrophobic and low density silica aerogels dried at ambient pressure using teos precursor. *Journal of Alloys and Compounds*, 471(1):296 – 302, 2009.

[22] H. Yokogawa and M. Yokoyama. Hydrophobic silica aerogels. *Journal of Non-Crystalline Solids*, 186:23 – 29, 1995.

[23] A. V. Rao and G. M. Pajonk and S. D. Bhagat and P. Barboux. Comparative studies on the surface chemical modification of silica aerogels based on various organosilane compounds of the type R_nSiX_{4-n}. *Journal of Non-Crystalline Solids*, 350:216 – 223, 2004.

[24] A. P. Rao, A. V. Rao, and G. M. Pajonk. Hydrophobic and physical properties of the ambient pressure dried silica aerogels with sodium silicate precursor using various surface modification agents. *Applied Surface Science*, 253:6032 – 6040, 2007.

[25] S. D. Bhagat, Y.-H. Kim, M.-J. Moon, Y.-S. Ahn, and J.-G Yeo. A cost-effective and fast synthesis of nanoporous SiO_2 aerogel powders using water-glass via ambient pressure drying route. *Solid State Sciences*, 9(7):628 – 635, 2007.

[26] S. D. Bhagat, Y.-H. Kim, Y.-S. Ahn, and J.-G. Yeo. Textural properties of ambient pressure dried water-glass based silica aerogel beads: One day synthesis. *Microporous and Mesoporous Materials*, 96(1):237 – 244, 2006.

[27] S. D. Bhagat, Y.-H. Kim, K.-H. Suh, Y.-S. Ahn, J.-G. Yeo, and J.-H. Han. Superhydrophobic silica aerogel powders with simultaneous surface modification, solvent exchange and sodium ion removal from hydrogels. *Microporous and Mesoporous Materials*, 112(1):504 – 509, 2008.

[28] C. E. Kim, J. S. Yoon, and H. J. Hwang. Synthesis of nanoporous silica aerogel by ambient pressure drying. *Journal of Sol-Gel Science and Technology*, 49(1):47, Sep 2008.

[29] P. R. Aravind, P. Shajesh, G. D. Soraru, and K. G. K. Warrier. Ambient pressure drying: a successful approach for the preparation of silica and silica based mixed oxide aerogels. *Journal of Sol-Gel Science and Technology*, 54(1):105 – 117, Apr 2010.

[30] A. V. Rao, E. Nilsen, and M.-A. Einarsrud. Effect of precursors, methylation agents and solvents on the physicochemical properties of silica aerogels prepared by atmospheric pressure drying method. *Journal of Non- Crystalline Solids*, 296:165 – 171, 2001.

[31] J. A. Schwarz, C. Contescu, and A. Contescu. Methods for Preparation of Catalytiv Materials. *Chemical Reviews*, 94:477 – 510, 1994.

[32] M. A. Vannice. *Kinetics of Catalytic Reactions*. Springer US, 2005.

[33] C. H. Bartholomew. Mechanisms of catalyst deactivation. *Applied Catalysis A: General*, 212(1):17 – 60, 2001.

[34] G. Jacobs, T. K Das, Y. Z., J. L., G. R., and B. H Davis. Fischer–Tropsch synthesis: support, loading, and promoter effects on the reducibility of cobalt catalysts. *Applied Catalysis A:*

General, 233(1):263 – 281, 2002.

[35] R. Köhn and M. Fröba. Nanoparticles of 3d transition metal oxides in mesoporous MCM-48 silica host structures: Synthesis and characterization. *Catalysis Today*, 68(1):227 – 236, 2001.

[36] Z. Wang, Q. Liu, J. Yu, T. Wu, and G. Wang. Surface structure and catalytic behavior of silica-supported copper catalysts prepared by impregnation and sol–gel methods. *Applied Catalysis A: General*, 239(1):87 – 94, 2003.

[37] A. Baiker, J.-D. Grunwaldt, C. A. Miiller, and L. Schmid. Catalytic Materials by Design. *CHIMIA International Journal for Chemistry*, 52(10):517–524, 1998.

[38] J. L. Mohanan and S. L. Brock. Influence of Synthetic and Processing Parameters on the Surface Area, Speciation, and Particle Formation in Copper Oxide/Silica Aerogel Composites. *Chemical Materials*, 15:2567 – 2576, 2003.

[39] B. C. Dunn, P. Cole, D. Covington, M. C. Webster, R. J. Pugmire, R. D. Ernst, E. M. Eyring, Na. Shah, and G. P. Huffman. Silica aerogel supported catalysts for Fischer–Tropsch synthesis. *Applied Catalysis A: General*, 278(2):233 – 238, 2005.

[40] J. C. Bailar. "HETEROGENIZING" HOMOGENEOUS CATALYSTS. *Catalysis Reviews*, 10(1):17–36, 1974.

[41] L. Owens and T. M. Tillotson and L. M. Hair. Characterization of vanadium/silica and copper/silica aerogel catalysts. *Journal of Non-Crystalline Solids*, 186(Supplement C):177 – 183, 1995.

[42] P. Fabrizioli and T. Bürgi and M. Burgener and S. van Doorslaer and A. Baiker. Synthesis, structural and chemical properties of iron oxide–silica aerogels. *Journal of Materials Chemistry*, 12(3):619 – 630, 2001.

[43] A. Khodakov and W. Chu and P. Fongarland. Advances in the Development of Novel Cobalt Fischer—Tropsch Catalysts for Synthesis of Long-Chain Hydrocarbons and Clean Fuels. *Chemical reviews*, 107:1692 – 744, 06 2007.

[44] J.-S. Girardon, A. S. Lermontov, L. G., P. A. Chernavskii, A. Griboval-Constant, and A. Y. Khodakov. Effect of cobalt precursor and pretreatment conditions on the structure and

catalytic performance of cobalt silica-supported fischer–tropsch catalysts. *Journal of Catalysis*, 230(2):339 – 352, 2005.

[45] S. F. Yin, B. Q. Xu, X. P. Zhou, and C. T. Au. A mini-review on ammonia decomposition catalysts for on-site generation of hydrogen for fuel cell applications. *Applied Catalysis A: General*, 277(1):1 – 9, 2004.

[46] S. F. Yin, B. Q. Xu, W. X. Zhu, C. F. Ng, X. P. Zhou, and C. T. Au. Carbon nanotubes-supported Ru catalyst for the generation of CO_x-free hydrogen from ammonia. *Catalysis Today*, 93-95(Supplement C):27 – 38, 2004.

[47] A. Boisen and S. Dahl and J. K. Nørskov and C. H. Christensen. Why the optimal ammonia synthesis catalyst is not the optimal ammonia decomposition catalyst. *Journal of Catalysis*, 230(2):309 – 312, 2005.

[48] D. Varisli and N. G. Kaykac. Hydrogen from ammonia over cobalt incorporated silicate structured catalysts prepared using different cobalt salts. *International Journal of Hydrogen Energy*, 41(14):5955 – 5968, 2016.

[49] S. Podila, Y. A. Alhamed, A. A. AlZahrani, and L. A. Petrov. Hydrogen production by ammonia decomposition using co-catalyst supported on mg mixed oxide systems. *International Journal of Hydrogen Energy*, 40(45):15411 – 15422, 2015.

[50] R. Metkemeijer and P. Achard. Comparison of ammonia and methanol applied indirectly in a hydrogen fuel cell. *International Journal of Hydrogen Energy*, 19(6):535 – 542, 1994.

[51] R. Z. Sørensen, L. J. E. Nielsen, S. Jensen, O. Hansen, T. Johannessen, U. Quaade, and C. H. Christensen. Catalytic ammonia decomposition: miniaturized production of CO_x-free hydrogen for fuel cells. *Catalysis Communications*, 6(3):229 – 232, 2005.

[52] J. Zhang, M. Comotti, F. Schüth, R. Schlögla, and D. S. Su. Commercial Fe- or Co-containing carbon nanotubes as catalysts for NH_3 decomposition. *Chemical Communications*, 19:1916 – 1918, 2007.

[53] I. Chorkendroff and J. W. Niemansverdriet. *Concepts of Modern Catalysis and Kinetics. 2^{nd} edition.* Wiley, 2007.

[54] B. S. Clausen, H. Topsøe, and R. Frahm. Application of combined x-ray diffraction and absorption techniques for in-situ catalyst characterization. *Advances in catalysis*, 42:315 – 344, 1998.

[55] M. A. Rida and F. Harb. Synthesis and Characterization of Amorphous Silica Nanoparticles from Aqueous Silicates Using Cationic Surfactants. *Journal of Metals, Materials and Minerals*, 24(1):37 – 42, 2014.

[56] K. S. W. Sing, D. H. Everett, R. A. W. Haul, L. Moscou, R. A. Pierotti, J. Rouquérol, and T. Siemieniewska. Reporting physisorption data for gas/solid systems with special reference to the determination of surface area and porosity. *Pure Applied Chemistry*, 57(4):603 – 619, 1985.

[57] E. P. Barrett, L. G. Joyner, and P. P. Halenda. The Determination of Pore Volume and Distributions in Porous Substances. I. Computations from Nitrogen Isotherms. *Journal of the American Chemical Society*, 73:373, 1951.

[58] A. Montaser. Indictively Coupled Plasma Mass Spectrometry. *Wiley-VCH*, 1998.

[59] H. Taylor. Indictively Coupled Plasma Mass Spectrometry Practices and Techniques. *California: Academic press*, 2001.

[60] V. S. Ramachandran and J. J. Beaudoin. *Handbook of Analytical Techniques in Concrete Science and Technology*. William Andrew Publishing/Noyes, 2001.

[61] D. A. Skoog and J. J. Leary. *Principles of Instrumental Analysis, 4th Ed.* Harcourt Brace Jovanovich, 1992.

[62] M. Newville. Fundamentals of XAFS. http://http://www.xafs.org/Tutorials. Accessed: 2017-11-20.

[63] D. C. Koningsberger, B. L. Mojet, G. E. van Dorssen, and D. E. Ramaker. Xafs spectroscopy; fundamental principles and data analysis. *Topics in Catalysis*, 10(3):143–155, May 2000.

[64] J. A. Bearden and A. F. Burr. Reevaluation of X-Ray Atomic Energy Levels. *Reviews of Modern Physics*, 39:125 – 142, 01 1967.

[65] F. de Groot, G. Vankó, and P. Glatzel. The 1s x-ray absorption pre-edge structures in transition metal oxides. *Journal of Physics: Condensed Matter*, 21(10):104207, 2009.

[66] P. Atkins and J. de Paula. *Elements of Physical Chemistry 6th ed.* Oxford University Press, 2010.

[67] C. H. M. van Oversteeg and H. Q. Doan and F. M. F de Groot and T. Cuk. In situ X-ray absorption spectroscopy of transition metal based water oxidation catalysts. *Chemical Society Reviews*, (46):102 – 125, 2016.

[68] D. Joseph and S. Basu and S. N. Jha and D. Bhattacharyya. Chemical shifts of K-X-ray absorption edges on copper in different compounds by X-ray absorption spectroscopy (XAS) with Synchrotron radiation. *Nuclear Instruments and Methods in Physics Research Section B: Beam Interactions with Materials and Atoms*, 274(Supplement C):126 – 128, 2012.

[69] B. K. Teo. *EXAFS: Basic principles and data analysis.* Springer-Verlag Berlin Heidelberg, 1986.

[70] B. Ravel and M. Newville. ATHENA, ARTEMIS, HEPHAESTUS: data analysis for X-ray absorption spectroscopy using IFEFFIT. *Journal of Synchrotron Radiation*, 12(5):537 – 541, 2005.

[71] F. A. Akgul and G. Akgul and M. Kurban. Microstructural properties and local atomic structures of cobalt oxide nanoparticles synthesised by mechanical ball-milling process. *Philosophical Magazine*, 96(30):3211 – 3226, 2016.

[72] N. N. Greenwood and A. Earnshaw. *Chemistry of the Elements (2nd ed.).* Pergamon Press plc, 1997.

[73] K. McAulay, J. S. J. Hargreaves, A. R. McFarlane, D. J. Price, N. A. Spencer, N. Bion, F. Can, M. Richard, H. F. Greer, and W. Z. Zhou. The influence of pre-treatment gas mixture upon the ammonia synthesis activity of Co–Re catalysts. *Catalysis Communications*, 68(Supplement C):53 – 57, 2015.

[74] S. Tomic and B. G. Searle and A. Wander and N. M. Harrison and A. J. Dent and J. F. W. Mosselmans and J. E. Inglesfield. New tools for the analysis of EXAFS: The DL EXCURV package. *Council for the Central Laboratory of the Research Councils.*

[75] T. Kristiansen and K. Mathisen and M.-A. Einarsrud and M. Bjørgen and D. G. Nicholson. Single-Site Copper by Incorporation in Ambient Pressure Dried Silica Aerogel and Xe-

rogel Systems: An X-ray Absorption Spectroscopy Study. *Journal of Physical Chemistry*, 115:19260 – 19268, 2011.

[76] K. Schmidt-Szałowski, K. Krawczyk, and J. Petryk. The properties of cobalt oxide catalyst for ammonia oxidation. *Applied Catalysis A: General*, 175(1):147 – 157, 1998.

[77] X. Yanran, H. Xinxin, Y. Han, G. Ziwang, J. Zhao, and J. Chunjiang. Fe- and co-doped lanthanum oxides catalysts for ammonia decomposition: Structure and catalytic performances. *JOURNAL OF RARE EARTHS*, 35(1):15–23, 2017.

[78] K. Khivantsev, A. Biancardi, M .Fathizadeh, F. Almalki, J. L. Grant, H. N. Tien, A. Shakouri, D. Blom, T. M. Makris, J. R. Regalbuto, M. Caricato, and M. Yu. Catalytic n-h bond activation and breaking by a well-defined co(ii)1o4 site of a heterogeneous catalyst. *ChemCatChem*, 2017.

[79] K. V. Khivantsev and F. A. and M. Yu. Catalytic Ammonia Decomposition to Hydrogen and Nitrogen on Supported Nanosized and Single-Site Cobalt Catalysts: Effects of Atomicity, Ligand Environment and Support. https://aiche.confex.com/aiche/2016/webprogram/Paper472372.html. Accessed: 2017-12-06.

Appendix

A Experimental

Table A.1: Synthesis parameters of gels from the Co-content parameter study.

Sample name	Molar ratio H_2O:Si	Molar ratio HMDZ:Si	Molar ratio HMDSO:Si	Molar ratio Co:Si	Cobalt precursor
Co0.0025	33	0.70	0.073	0.0025	Nitrate
Co0.0125	33	0.70	0.073	0.0125	Nitrate
Co0.025	33	0.70	0.073	0.025	Nitrate
Co0.05	33	0.70	0.073	0.05	Nitrate
Co0.10	33	0.70	0.073	0.10	Nitrate
Co0.15	33	0.70	0.073	0.15	Nitrate
Co0.20	33	0.70	0.073	0.20	Nitrate
Co0.25	33	0.70	0.073	0.25	Nitrate

Table A.2: Synthesis parameters of gels from the concentration of silylation agents and cobalt precursor parameter study.

Sample name	Molar ratio H_2O:Si	Molar ratio HMDZ:Si	Molar ratio HMDSO:Si	Molar ratio Co:Si	Cobalt precursor
N_0.25	33	0.25	0.25	0.025	Nitrate
N_0.50	33	0.50	0.50	0.025	Nitrate
N_1.00	33	1.00	1.00	0.025	Nitrate
Ac_0.25	33	0.25	0.25	0.025	Acetate
Ac_0.50	33	0.50	0.50	0.025	Acetate
Ac_1.00	33	1.00	1.00	0.025	Acetate

Table A.3: Synthesis parameters of gels from the pH parameter study.

Sample name	**Molar ratio H_2O:Si**	**Molar ratio HMDZ:Si**	**Molar ratio Co:Si**	**pH**	**Cobalt Precursor**
N_pH3.6	33	7	0.025	3.6	Nitrate
N_pH5.0	33	7	0.025	5.0	Nitrate
N_pH6.2	33	7	0.025	6.2	Nitrate
Ac_pH3.5	33	7	0.025	3.5	Acetate
Ac_pH5.0	33	7	0.025	5.0	Acetate
Ac_pH6.9	33	7	0.025	6.9	Acetate

Table A.4: Synthesis parameters of gels washed with ethanol and heptane

Sample name	**Molar ratio H_2O:Si**	**HMDZ (20 vol% in heptane)**	**Molar ratio Co:Si**	**pH**	**Cobalt Precursor**
Co0.0025_W	33	75 ml	0.0025	4.7	Nitrate
Co0.0125_W	33	75 ml	0.0125	4.7	Nitrate
Co0.025_W	33	75 ml	0.025	4.7	Nitrate

B XRD

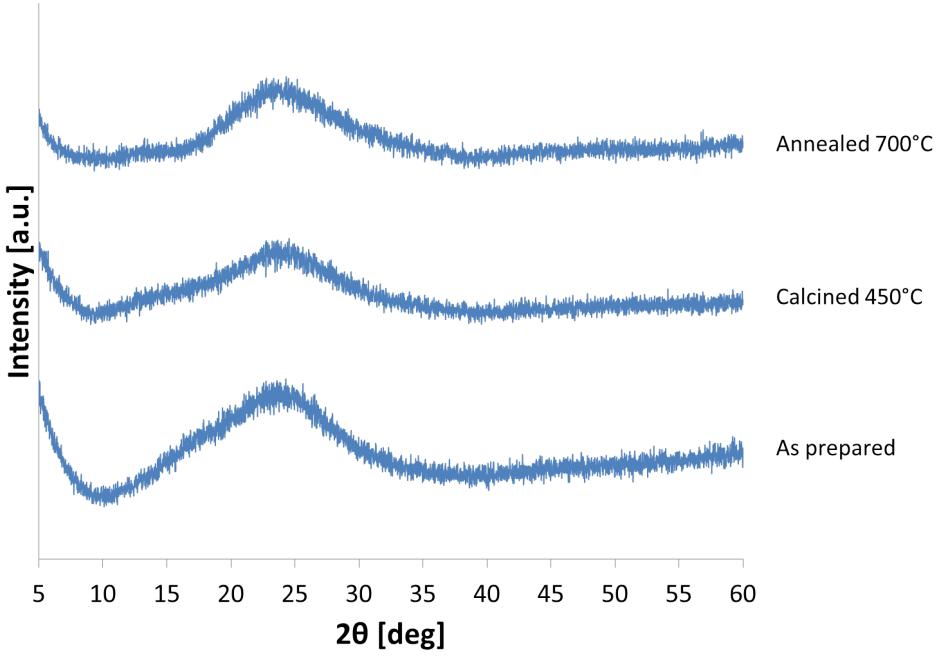

Figure B.1: X-Ray Diffraction patterns of Co0.0125 as prepared, calcined at 450 °C and annealed at 700 °C.

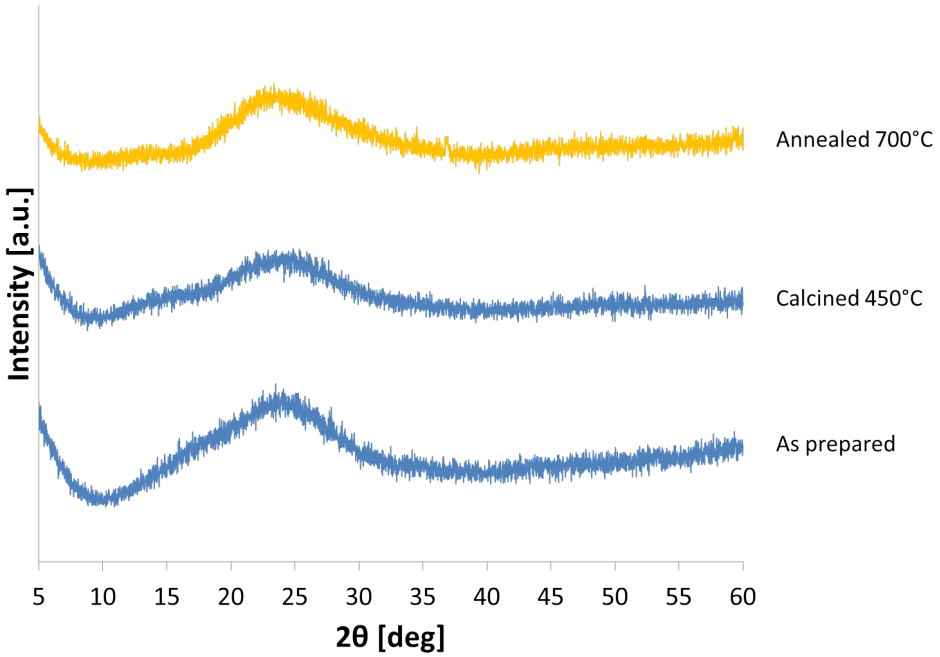

Figure B.2: X-Ray Diffraction patterns of Co0.025 as prepared, calcined at 450 °C and annealed at 700 °C.Yellow line indicates low presence of crystalline phases.

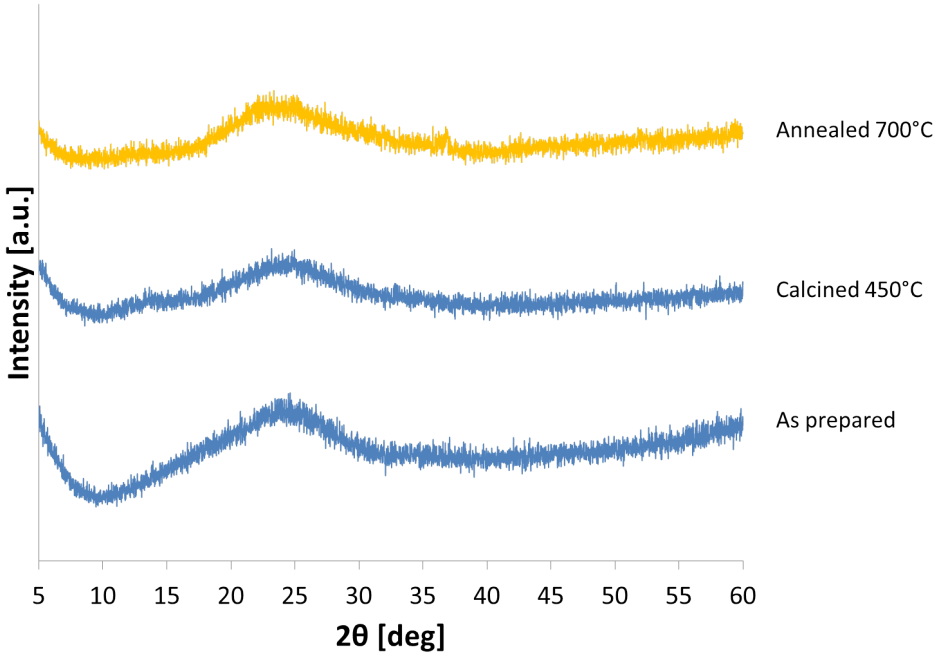

Figure B.3: X-Ray Diffraction patterns of Co0.05 as prepared, calcined at 450 °C and annealed at 700 °C.Yellow line indicates low presence of crystalline phases.

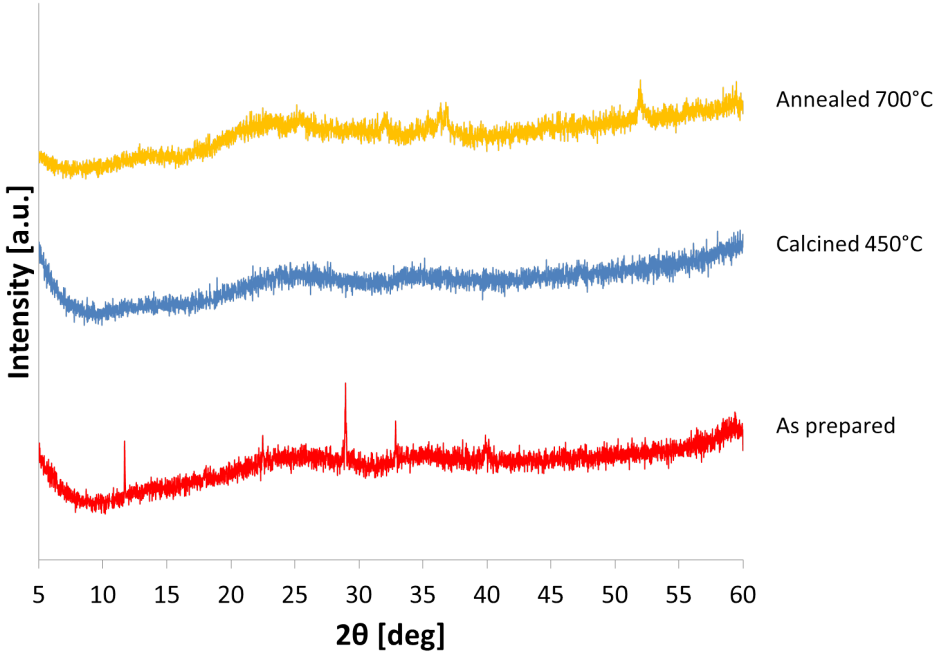

Figure B.4: X-Ray Diffraction patterns of Co0.15 as prepared, calcined at 450 °C and annealed at 700 °C. Yellow line indicates low presence of crystalline phases and red line indicates high presence of crystalline phases.

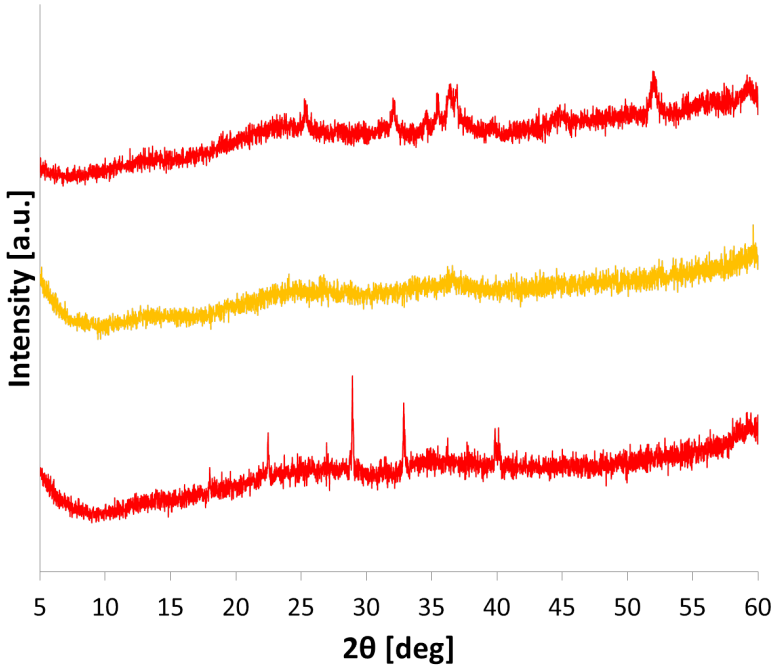

Figure B.5: X-Ray Diffraction patterns of Co0.20 as prepared, calcined at 450 °C and annealed at 700 °C. Yellow line indicates low presence of crystalline phases and red line indicates high presence of crystalline phases.

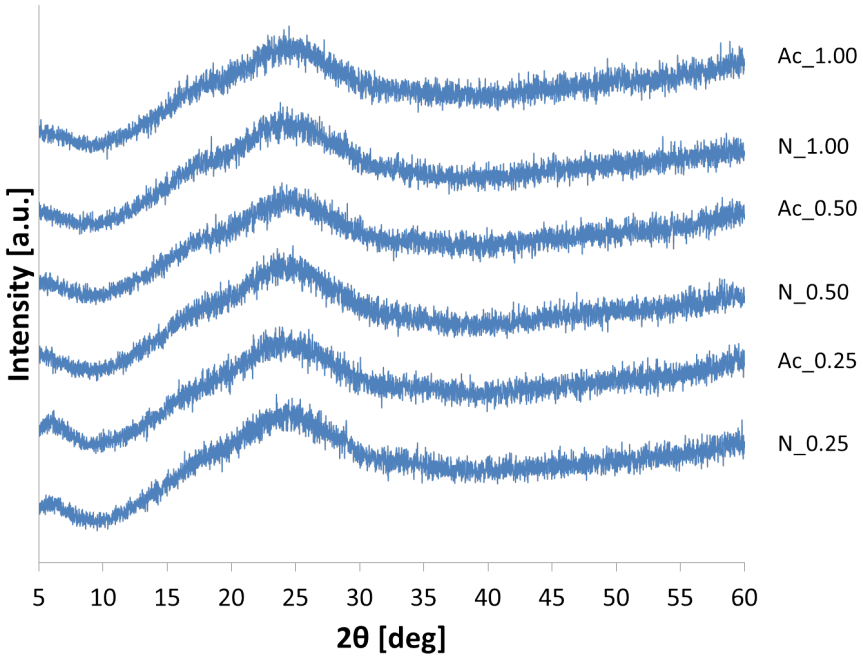

Figure B.6: X-Ray Diffraction patterns of the nitrate gels as well as the acetate gels as prepared from the concentration of silylation agents and precursor parameter study.

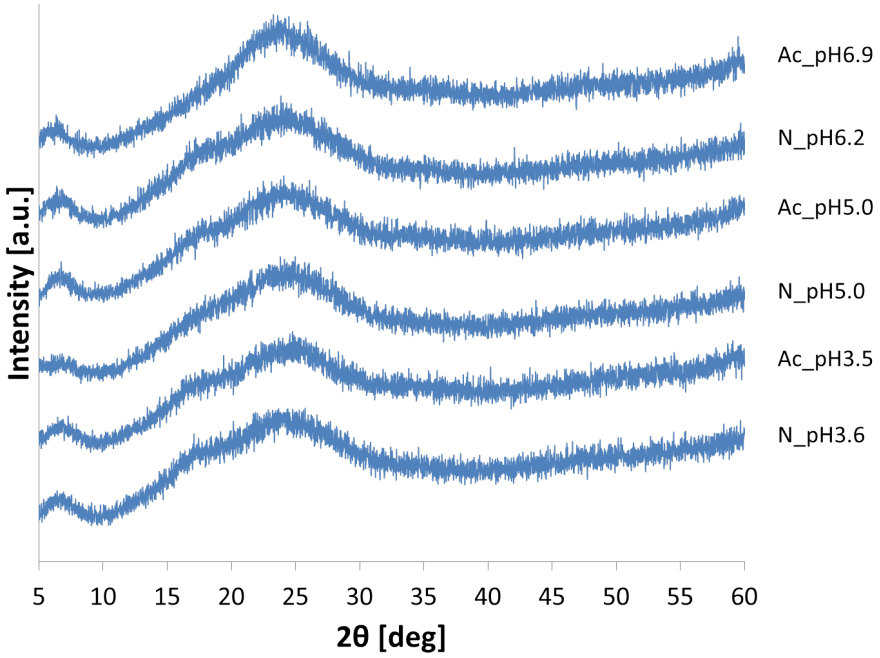

Figure B.7: X-Ray Diffraction patterns of the nitrate gels as well as the acetate gels as prepared from pH parameter study.

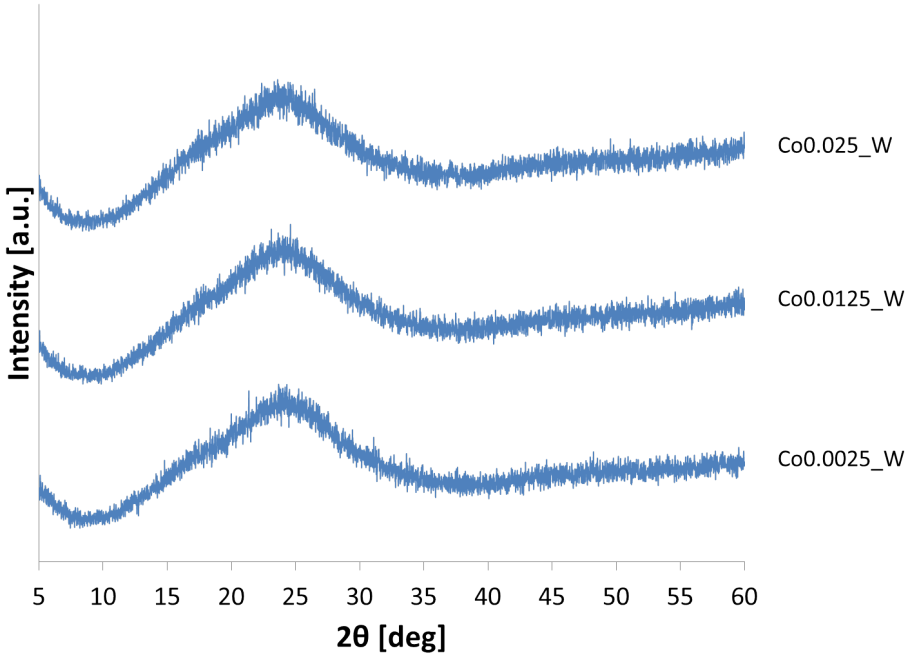

Figure B.8: X-Ray Diffraction patterns of the ethanol and heptane washed gels as prepared.

C BET and BJH

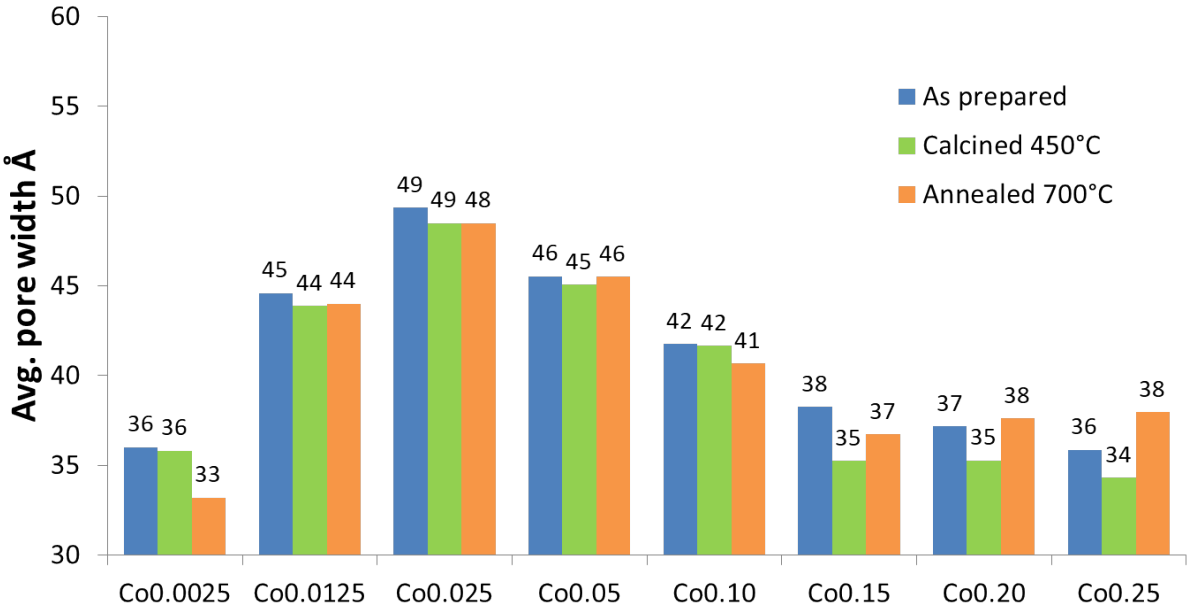

Figure C.9: Average pore width of gels from the Co-content parameter study.

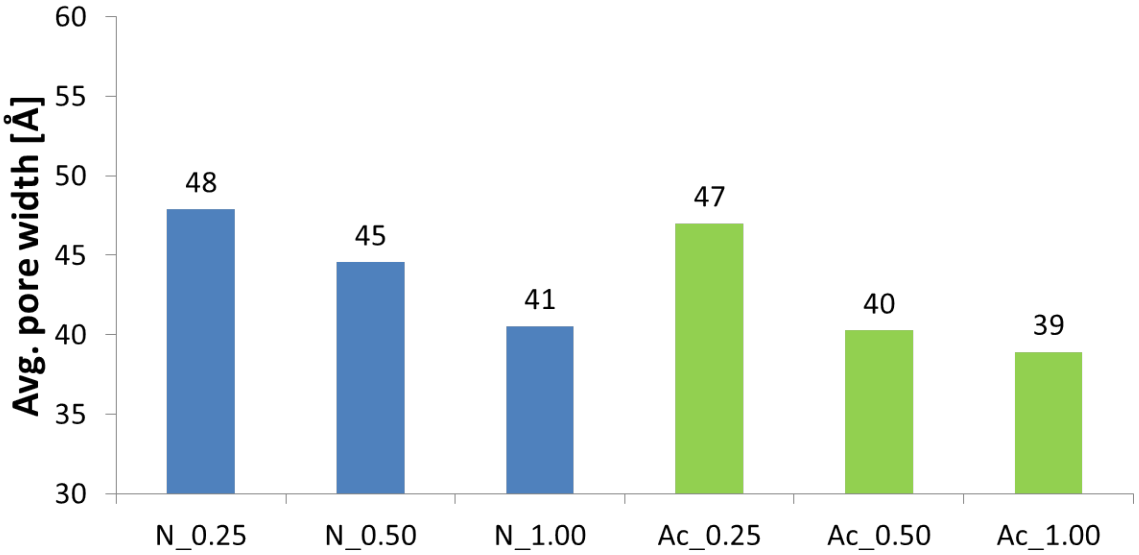

Figure C.10: Average pore width of gels from the concentration of silylation agents and precursor parameter study.

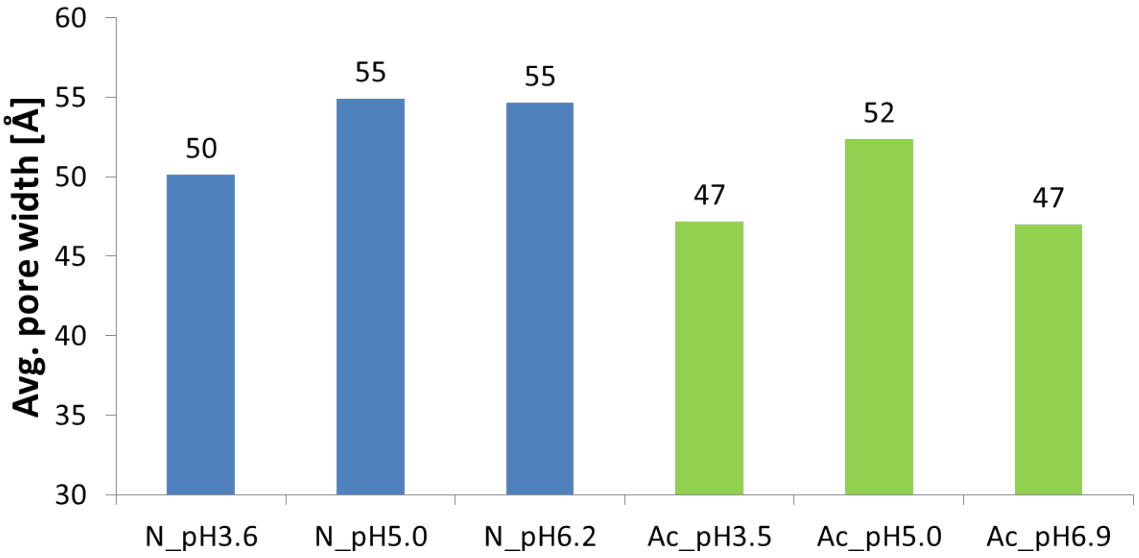

Figure C.11: Average pore width of gels from the pH parameter study

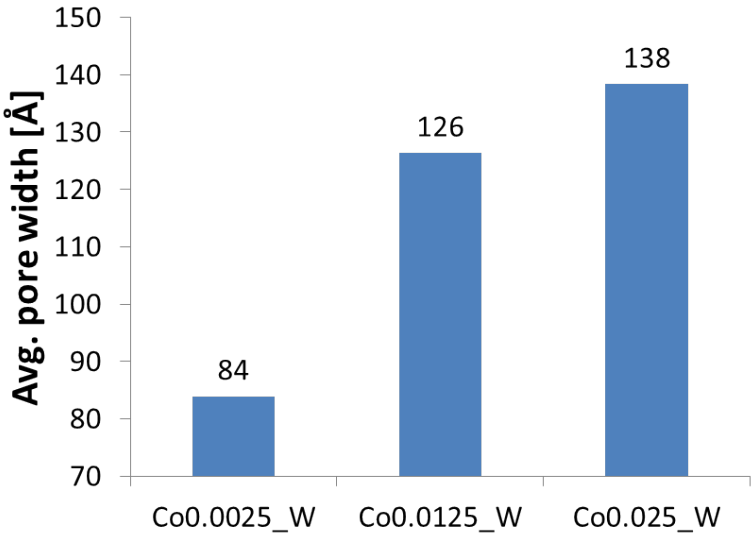

Figure C.12: Average pore width of gels washed with ethanol and heptane.

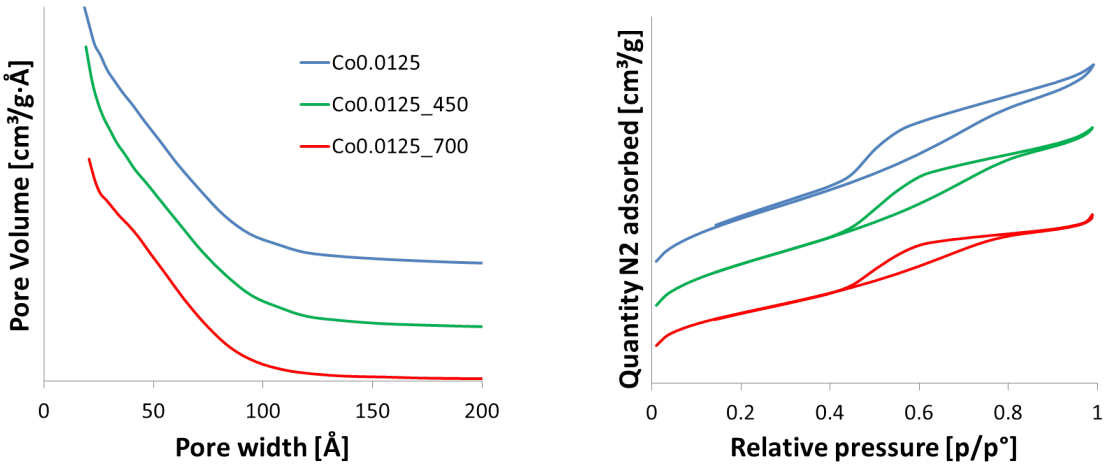

Figure C.13: Pore distribution and adsorption and desorption isotherms for Co0.0125 and its calcined and annealed analogue.

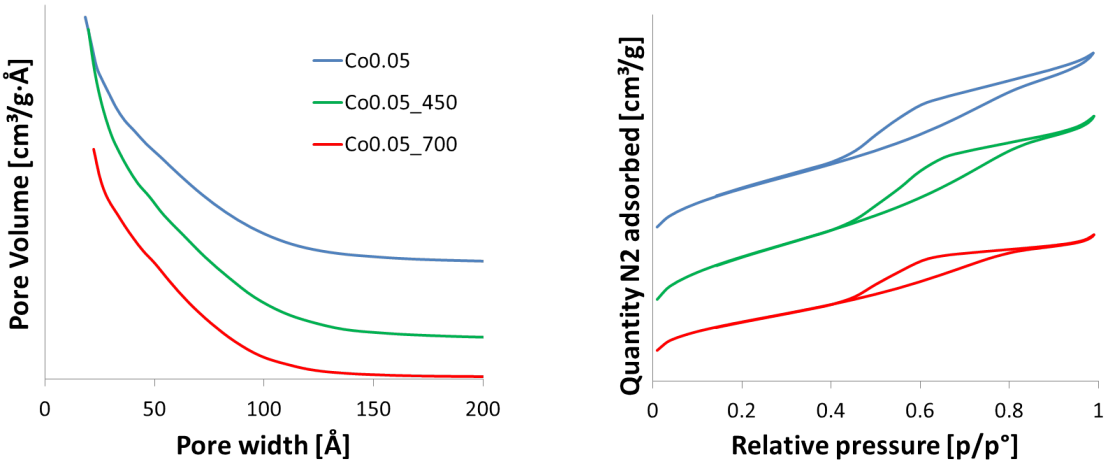

Figure C.14: Pore distribution and adsorption and desorption isotherms for Co0.05 and its calcined and annealed analogue.

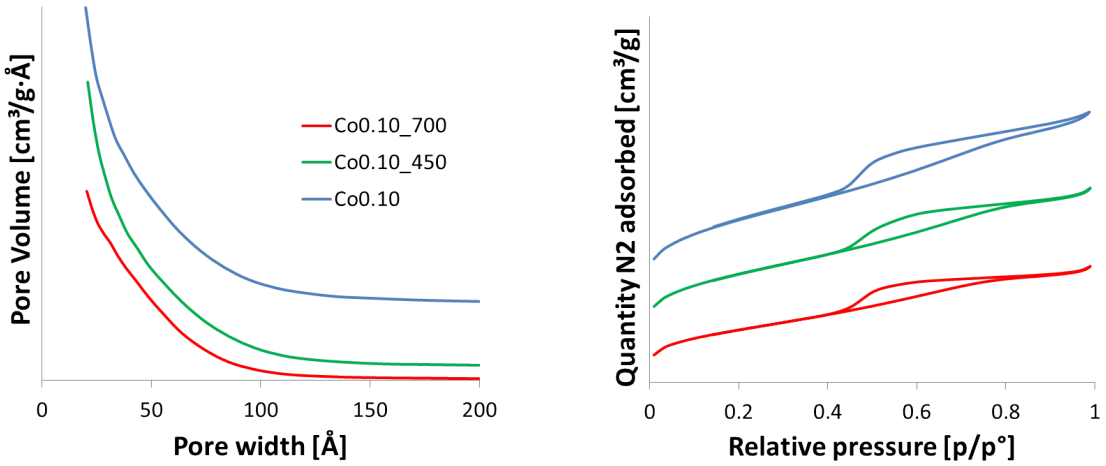

Figure C.15: Pore distribution and adsorption and desorption isotherms for Co0.10 and its calcined and annealed analogue.

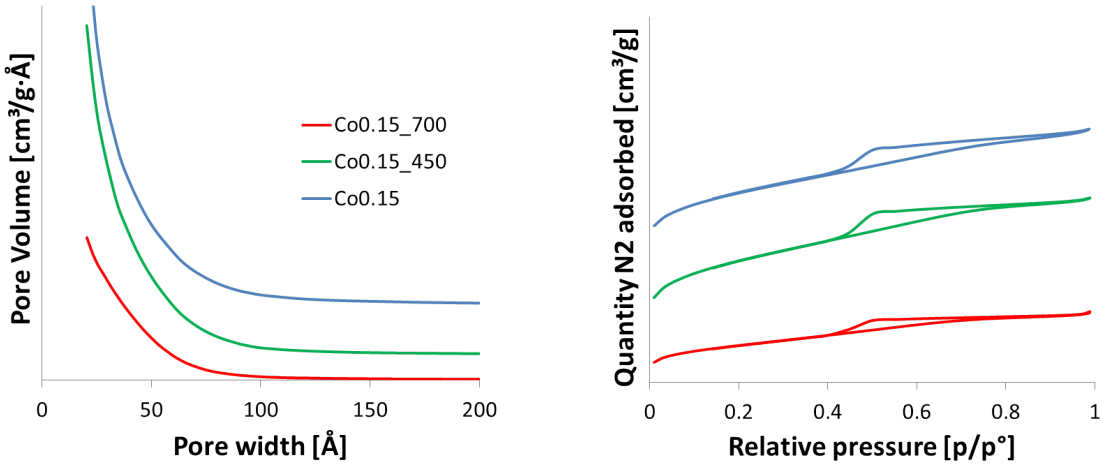

Figure C.16: Pore distribution and adsorption and desorption isotherms for Co0.15 and its calcined and annealed analogue.

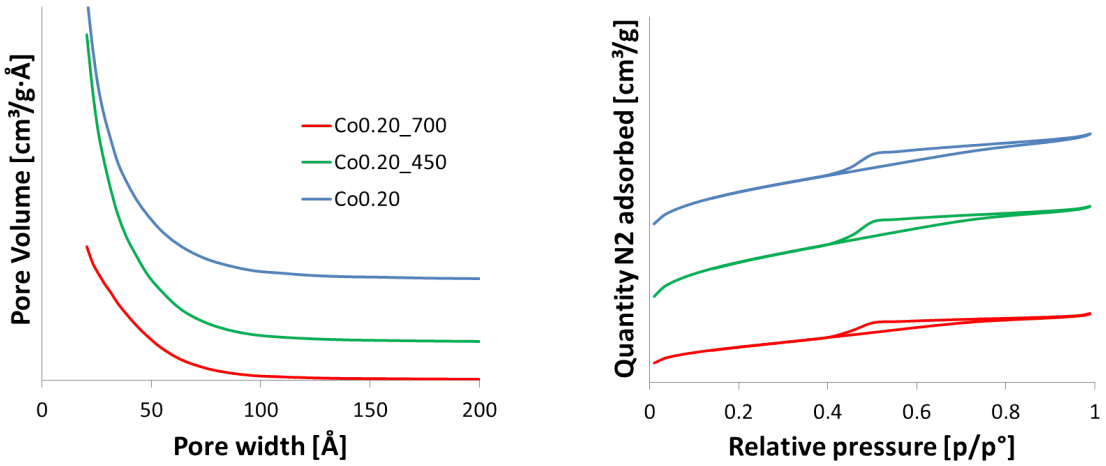

Figure C.17: Pore distribution and adsorption and desorption isotherms for Co0.20 and its calcined and annealed analogue.

D ICP-MS

Table D.5: Theoretical molar ratio of Si:Co along with the experimental molar ratio of Si:Co and wt.% of Co calculated from the ICP-MS for the cobalt content parameter study.

Sample name	**Theoretical molar ratio Co:Si**	**Experimental molar ratio Co:Si**	**Cobalt wt.%**
Co0.0025	0.0025	0.0034	0.20
Co0.0125	0.0125	0.017	0.93
Co0.025	0.025	0.028	1.80
Co0.05	0.050	0.054	2.94
Co0.10	0.10	0.13	6.82
Co0.15	0.15	0.16	8.06
Co0.20	0.20	0.21	8.81
Co0.25	0.25	0.28	11.09

Table D.6: Theoretical molar ratio of Si:Co along with the experimental molar ratio of Si:Co and wt.% of Co calculated from the ICP-MS for the calcined gels from the cobalt content parameter study.

Sample name	**Theoretical molar ratio Co:Si**	**Experimental molar ratio Co:Si**	**Cobalt wt.%**
Co0.0025_450	0.0025	0.0032	0.22
Co0.0125_450	0.0125	0.017	1.27
Co0.025_450	0.025	0.034	2.11
Co0.05_450	0.050	0.041	2.94
Co0.10_450	0.10	0.069	4.78
Co0.15_450	0.15	0.15	9.79
Co0.20_450	0.20	0.19	12.69
Co0.25_450	0.25	0.24	14.51

Table D.7: Theoretical molar ratio of Si:Co along with the experimental molar ratio of Si:Co and wt.% of Co calculated from the ICP-MS for the annealed gels from the cobalt content parameter study.

Sample name	**Theoretical molar ratio Co:Si**	**Experimental molar ratio Co:Si**	**Cobalt wt.%**
Co0.0025_700	0.0025	0.0023	0.24
Co0.0125_700	0.0125	0.011	0.94
Co0.025_700	0.025	0.020	1.70
Co0.05_700	0.050	0.040	3.33
Co0.10_700	0.10	0.078	7.23
Co0.15_700	0.15	0.12	9.62
Co0.20_700	0.20	0.15	10.33
Co0.25_700	0.25	0.18	13.93

Table D.8: Theoretical molar ratio of Si:Co along with the experimental molar ratio of Si:Co and wt.% of Co calculated from the ICP-MS for the concentration of silylation agents and precursor parameter study.

Sample name	**Theoretical molar ratio Co:Si**	**Experimental molar ratio Co:Si**	**Cobalt wt.%**
N_0.25	0.025	0.029	1.85
N_0.50	0.025	0.030	1.88
N_1.00	0.025	0.030	1.69
Ac_0.25	0.025	0.041	2.61
Ac_0.50	0.025	0.047	3.08
Ac_1.0	0.025	0.044	2.67

Table D.9: Theoretical molar ratio of Si:Co along with the experimental molar ratio of Si:Co and wt.% of Co calculated from the ICP-MS for the pH parameter study.

Sample name	**Theoretical molar ratio Co:Si**	**Experimental molar ratio Co:Si**	**Cobalt wt.%**
N_pH3.6	0.025	0.040	2.14
N_pH5.0	0.025	0.033	2.05
N_pH6.2	0.025	0.028	1.76
Ac_pH3.5	0.025	0.042	1.56
Ac_pH5.0	0.025	0.038	2.63
Ac_pH6.9	0.025	0.034	2.38

Table D.10: Theoretical molar ratio of Si:Co along with the experimental molar ratio of Si:Co and wt.% of Co calculated from the ICP-MS for the ethanol and heptane washed gels.

Sample name	**Theoretical molar ratio Co:Si**	**Experimental molar ratio Co:Si**	**Cobalt wt.%**
Co0.0025_W	0.0025	0.0011	0.0059
Co0.0125_W	0.0125	0.0021	0.17
Co0.025_W	0.025	0.0040	0.32